Membraneless Hydrogen Bromine Laminar Flow Battery for Large-Scale Energy Storage

by

William Allan Braff

Submitted to the Department of Mechanical Engineering
in partial fulfillment of the requirements for the degree of

Doctor of Philosophy

at the

MASSACHUSETTS INSTITUTE OF TECHNOLOGY

February 2014

ARCHIVES

MASSACHUSETTS INSTITUTE OF TECHNOLOGY
MAY 0 8 2014
LIBRARIES

© Massachusetts Institute of Technology 2014. All rights reserved.

Author .....
Department of Mechanical Engineering
December 19, 2013

Certified by .....
Cullen R. Buie
Assistant Professor of Mechanical Engineering
Thesis Supervisor

Certified by .....
Martin Z. Bazant
Professor of Chemical Engineering and Mathematics
Thesis Supervisor

Accepted by .....
David E. Hardt
Chairman, Department Committee on Graduate Theses

Membraneless Hydrogen Bromine Laminar Flow Battery for Large-Scale Energy Storage

by

William Allan Braff

Submitted to the Department of Mechanical Engineering
on December 19, 2013, in partial fulfillment of the
requirements for the degree of
Doctor of Philosophy

Abstract

Electrochemical energy storage systems have been considered for a range of potential large-scale energy storage applications. These applications vary widely, both in the order of magnitude of energy storage that is required and the rate at which energy must be charged and discharged. One such application aids the integration of renewable energy technologies onto the electrical grid by shifting the output from renewable energy resources to periods of high demand, relaxing transmission and distribution requirements and reducing the need for fossil fuel burning plants. Although the market need for such solutions is well known, existing technologies are still too expensive to compete with conventional combustion-based solutions.

In this thesis, the hydrogen bromine laminar flow battery (HBFLB) is proposed and examined for its potential to provide low cost energy storage using the rapid reaction kinetics of hydrogen-bromine reaction pairs and a membrane-less laminar flow battery architecture. In this architecture, fluid reactants and electrolyte flow through a small channel at sufficiently low Reynolds number that laminar flow is maintained and the liquid electrolyte acts as a separator between the reactants.

Experimental results from a proof of concept cell are presented, and compared with numerical and analytical modeling results to better understand discharging and recharging behavior. General theoretical principles for the design and optimization of laminar flow batteries are also developed. These results indicate that the HBLFB can efficiently store and discharge energy at very high power densities compared to existing battery technologies using low cost reactants and stack materials at room temperature and atmospheric pressure.

Thesis Supervisor: Cullen R. Buie
Title: Assistant Professor of Mechanical Engineering

Thesis Supervisor: Martin Z. Bazant
Title: Professor of Chemical Engineering and Mathematics

Acknowledgments

The work that I've done for my Ph.D. would never have been possible without the support of a number of people. I am deeply indebted to my coadvisors, Professors Cullen Buie and Martin Bazant, from whom I've learned a great deal, and whose advice and guidance have helped me grow as an engineer. I am also very grateful to Professor Jessika Trancik for her help to better understand grid-scale storage, and to Bill Aulet, Tod Hynes, Frank O'Sullivan, Lucas DiLeo, Louis Goldish, Roman Lybinsky, and Tom Pounds for their mentorship and advice about the entrepreneurial implications of the work. I must also thank Dr. Cortney Mittelsteadt, whose support and advice set me on the road to becoming an engineer in the first place, and without whom I would never have had the chance to pursue a Ph.D.

I would also like to acknowledge the support of my colleagues in the Buie and Bazant groups. Thanks to Dr. Matthew Suss, Laura Gilson, Gregoire Jacquot, Ricardo Charles, and Kameron Conforti for their past and future contributions to the flow battery project. I am also grateful for the advice and support I have received from my other labmates, Dr. Peng Bai, Dr. Daosheng Deng, Naga Dingari, Dr. Todd Ferguson, Zhifei Ge, Dr. Jihyung Han, Dr. Paulo Garcia, Laura Gilson, Youngsoo Joung, Andrew Jones, Edwin Khoo, Dr. Jeff Moran, Dr. Sourav Padhy, Matthew Pinson, Carlos Sauer, Sven Schlumpberger, Alisha Schor, Ray Smith, Qianru Wang, Yi Zeng, and Dr. Pei Zhang. Thanks as well to my colleagues at the Sloan School of Management, Jamie Fordyce and Dave Parkin, from whom I learned a great deal.

In addition to the excellent professional mentorship and guidance I have received, my deepest gratitude goes to my family for their unending patience and belief in me over the past years. My mother and father, Florence and Allan, and my siblings and their spouses, Jen, Joe, Jon, and Julie, have been constant sources of support for me, and I am grateful to all of them. Lastly, my wife Georgiana has been with me every step of the way, from the moment I applied to MIT onwards. Her love and support has been invaluable to me, and no words can describe how grateful I am to her.

Contents

List of Figures

List of Tables

Chapter 1

Introduction

1.1 Large-Scale Energy Storage

Today the electrical grid faces a number of critical challenges moving forward, including increased levels of distributed generation, larger market impact of renewable resources, and growing numbers of electric vehicles creating larger peak-trough demand behavior [9]. Low cost, reliable energy storage has the potential to address many of these issues, and represents one of the most critical technological challenges of the 21st century [10]. Efforts to provide low cost, reliable energy storage date back many decades. The most prevalent technologies to date have been pumped hydroelectric and compressed air energy storage [10]. These technologies very been very successful from a cost perspective, but are constrained to regions with the necessary geographic features: either rivers that can be dammed or underground caverns to store compressed air. These constraints limit where they can be installed on the electrical grid, reducing their applicability, and rendering them ineffective for many applications where location is critical, such as to relieve pressure on an overused transmission line [8, 11]. The demand for grid-scale storage is still in its infancy, but is forecast to grow from 3.2 GWh to 185 GWh over the next five years, representing a $113 billion market by 2017 [12].

At present, electrochemical energy storage technologies are simply too expensive to tap this vast market, so the need remains for a low-cost, scalable technology that

can address the needs of the electrical grid going into the future [8, 13]. Electrochemical energy storage technologies have made tremendous advances over the past several decades, including new chemistries and better designs. However, most of those improvements have been targeted towards improving the energy density of small to medium scale systems targeted towards applications ranging from mobile phones up to automobiles [14]. At the grid-scale, energy storage operates in a commodity market where system cost rather than energy density becomes the critical performance metric. Under these circumstances, a new framework for evaluating technologies is required.

1.2 Electrochemical Energy Storage

Electrochemical energy storage technologies operate on the principle of transferring ions between two active materials through an electrically insulating electrolyte, which drives electrons through an external circuit. Depending on the free energies of the two active materials, this process either releases or stores energy. For large-scale applications, the importance of system cost cannot be overstated, since these technologies must be competitive against low-cost fossil-fuel based technologies in order to be effective [9]. Exhaustive reviews of current storage technologies are available elsewhere [15], and are beyond the scope of this work, but a handful of technologies have emerged as leading candidates to provide large-scale energy storage for the grid. Lithium-ion batteries, hydrogen fuel cells, and vanadium redox flow batteries are three of the most well-known energy storage technologies today. Lithium-ion batteries in particular have achieved significant commercial success in the automotive market with their high energy density and proven record in the consumer electronics market. Unfortunately, the cost of the necessary active materials has been a challenge for large-scale implantation. Hydrogen oxygen regenerative fuel cells use water as their energy storage medium, so they enjoy extremely low active material costs. However, the high cost of the electrochemical stacks has delayed their development. Vanadium redox flow batteries represent something of a hybrid between these two

Table 1.1: Key performance metrics for lithium ion batteries (LIB), hydrogen oxygen regenerative fuel cells (RFC), vanadium redox flow batteries (VRB), and hydrogen bromine redox flow batteries (HBRFB).

Technology	Power density ($kW\ kg^{-1}$)	Energy density ($Wh\ kg^{-1}$)	Efficiency (%)	Power cost ($\$\ kW^{-1}$)	Energy cost ($\$\ kWh^{-1}$)
LIB	0.6 [16]	200 [16]	90 [15]	1800 [15]	900 [15]
RFC	0.06 [17]	400 [17]	50 [17]	1500 [8]	15 [8]
VRFB	0.3 [18]	25 [2]	90 [2]	200 [8]	250 [8]
HBRFB	0.5 [19]	60 [2]	90 [3]	150 [20]	80 [20]

technologies, with lower active material costs than lithium ion batteries as well as decreased stack costs compared to fuel cells. These cost savings are significant, but questions remain as to whether they will be enough to be competitive for large-scale applications. Hydrogen bromine flow batteries have the potential for even further cost savings, thanks to very low-cost reactants and superior power density compared to vanadium redox flow batteries, but significant technical challenges have hindered their development to date. A summary of key performance metrics for these storage technologies is shown in Table 1.1.

1.2.1 Lithium Ion Batteries

The first lithium ion batteries were developed nearly forty years ago as a room temperature energy storage solution [21]. The strongly negative potential of the lithium redox pair coupled to appropriate electrolyte and electrode materials ensured that that these type of batteries possess the potential for excellent energy density, with recent lab-scale efforts reporting values as high as 200 $Wh\ kg^{-1}$ [16,22]. In these systems, lithium ions pass through an organic electrolyte and intercalate into the cathode during charging, or anode during discharging, as shown in Figure 1-1. Key technological advancements such as graphite intercalation anodes [23], spinel cathodes [24], and numerous other contributions [25] have contributed to dramatic improvements in lithium-ion battery energy density and performance.

More recently, efforts have been made to enhance rate capability [26] and reduce cost by employing flow battery-like architectures [27–29]. However, the high cost and relative scarcity of lithium result in cost estimates for large-scale energy storage of roughly \$500 kWh^{-1}, significantly higher than alternatives [8]. Furthermore, it is impossible to decouple the power and energy capacities of these batteries at a system level because energy storage is achieved by intercalating lithium ions into the electrodes themselves. This is a major issue for large-scale applications that often require $4 - 8$ hours of energy storage. To store such large quantities of energy, a system employing lithium-ion batteries would have to be built with significantly more power generating capability than necessary, raising costs.

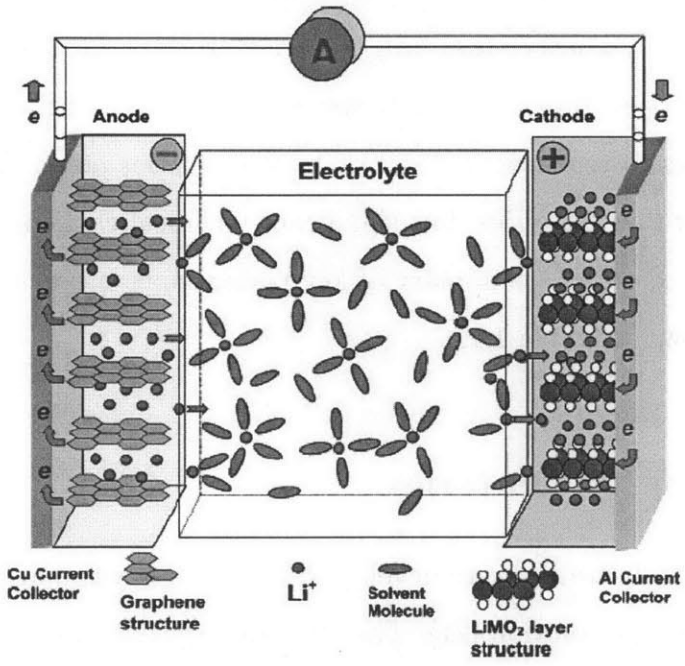

Figure 1-1: Exemplar schematic of a lithium-ion battery. During discharge, lithium ions pass from the graphene anode into the electrolyte, and then intercalate into a spinel cathode, forcing electrons through an external load. Figure reproduced from [1].

1.2.2 Hydrogen Oxygen Regenerative Fuel Cells

Hydrogen oxygen regenerative fuel cells were originally developed for the United States space program in the late sixties to address the need for long-duration en-

ergy storage during missions [30]. These systems employ hydrogen and oxygen as a redox couple, and can store these reactants in large external tanks so that the system's ability to store energy could be varied independently of its ability to generate or absorb power. Unlike lithium ion batteries, these systems employ porous electrodes through which fluid reactants, in this case hydrogen and oxygen, flow through the half cells and convert to water during discharge. To recharge the cell, water flows back through the system where it is electrolyzed back into hydrogen and oxygen. Because these systems store energy in pure gas and liquid phases, they can achieve extremely high theoretical energy densities, in excess of 400 Wh kg^{-1} [31]. Furthermore, the energy-specific cost of storage in these systems is only \$15 kWh^{-1}, thanks to their ability to store reactants in external tanks [8, 32].

Unfortunately, the electrochemical cells used to generate power and recharge the system are prohibitively expensive, with a power-specific cost of roughly \$1500 kW^{-1} [8]. Hydrogen oxygen regenerative fuel cell systems also suffer from low round trip energy efficiencies due to the poor reaction kinetics of the oxygen reduction and evolution reactions. Round trip efficiencies for these systems remain well below 50% despite significant efforts to identify effective bifunctional catalysts [33–36]. Such high losses contribute significantly to the operating cost of these systems, minimizing their feasibility for grid-scale applications [35].

1.2.3 Vanadium Redox Flow Batteries

Vanadium redox flow batteries are a relatively new technology compared to lithium-ion batteries and regenerative fuel cells. These systems build on the regenerative fuel cell by replacing the hydrogen-oxygen redox pair with aqueous vanadium and vanadium oxide solutions that can be charged and discharged by flowing through an electrochemical stack, as shown in Figure 1-2 [37]. The reaction kinetics of these systems are far superior to those of the oxygen electrode in a regenerative fuel cell, resulting in energy efficiencies as high as 90%. Like fuel cells, the ability to independently specify power and energy rating at the system level give these systems a significant advantage over lithium ion and other solid-state battery technologies [38]. Power-related costs

have declined significantly due to a number of system improvements, including revisions to the electrolyte chemistry [39,40], separator technology [41,42], and increased power density [18,43].

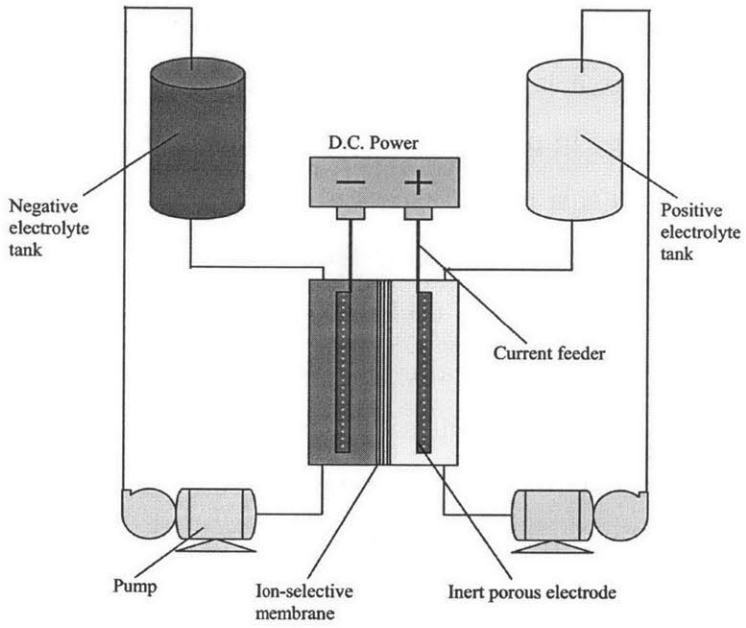

Figure 1-2: Schematic of a vanadium redox flow battery. The anolyte and catholyte are flowed past their respective electrodes to produce electrical energy. Figure reproduced with permission by the Electrochemical Society from Skyllas-Kazacos et al. [2].

The low solubility of vanadium in its carrier electrolyte results in energy densities around 25 Wh kg^{-1}, significantly lower than either regenerative fuel cells or lithium-ion batteries [2]. This is only a minor drawback for stationary energy applications, where cost is paramount and space is not at a premium. The more pressing challenge for vanadium system is the cost of reactants, with energy-related costs estimated to be roughly \$250 kWh^{-1} [2]. Additionally, the long term costs associated with producing large quantities of vanadium are expected to increase by a factor of ten if demand exceeds the capacity of current production methods. Currently, vanadium is produced as a byproduct from coal and oil mining and refining processes, but [44].

1.2.4 Hydrogen Bromine Redox Flow Batteries

Hydrogen bromine flow batteries were proposed in 1980 as a means to improve on the performance of hydrogen oxygen regenerative fuel cells by replacing gaseous oxygen with liquid bromine on the cathode of the cell as shown in Figure 1-3 [45, 46]. These systems have several advantages over the other energy storage technologies discussed here. Unlike oxygen, bromine is known to possess very rapid reaction kinetics for both reduction and evolution, facilitating highly efficient roundtrip energy storage [47–49]. Unlike vanadium, bromine is abundant and easily harvested at low cost. Energy-related storage costs are almost completely dominated by tank costs, with reactant costs of roughly \$4 kWh^{-1} [50]. Lastly, early efforts demonstrated the long lifetime potential of hydrogen bromine systems, with 10,000 hours of continuous operation reported from an early prototype [51].

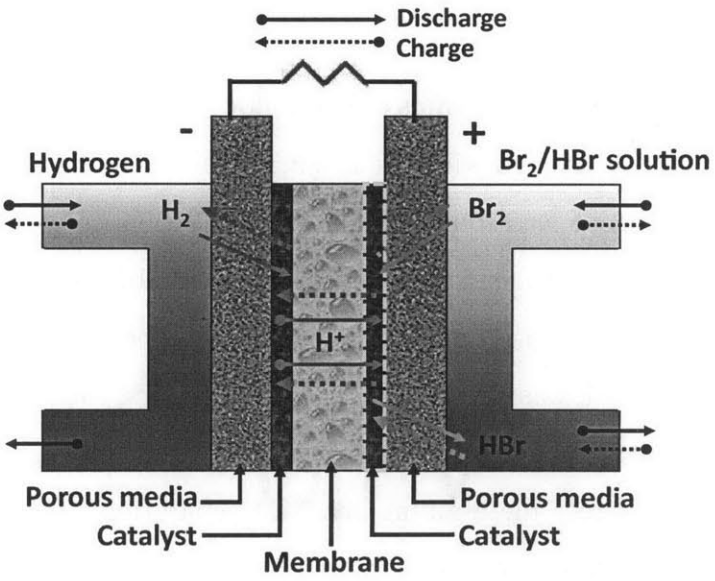

Figure 1-3: Cell schematic for a hydrogen bromine redox flow battery. During discharge, hydrogen is oxidized at the anode to produce protons and bromine is reduced at the cathode to generate hydrobromic acid. Electrons are forced through an external load. During charging, electrical energy is pumped back into the system to reverse the process and replenish the reactants. Figure reproduced with permission by the Electrochemical Society from Cho et al. [3].

The high solubility of bromine in aqueous solutions mitigates any mass transport

limitations associated with the cathode, and the rapid reaction kinetics at both the anode and cathode virtually eliminate activation losses [52]. However, the transport properties of the proton exchange membranes used to separate the half-cell reactions are highly influenced by the local water content. The hydrobromic acid produced at the cathode can dehydrate the membrane, increasing its resistance [53,54]. Theoretical and experimental characterization of these systems has confirmed that membrane conductivity remains a critical factor limiting cell performance [55,56]. Advancements such as nanoporous composite membranes [19] and porous flow-through electrodes [3] have resulted in enhanced power density, but membrane cost and durability remain major concerns. Currently, membranes represent the single most expensive component in commercial fuel cell designs [57,58].

1.3 Membrane-less Electrochemical Systems

The concept of using colaminar streams of liquid flowing at low Reynolds numbers was first developed fifteen years ago with the original goal of fabricating microstructures *in situ* [59]. This concept was soon applied to electrochemical cells, with the original concept demonstrating a membrane-less vanadium redox fuel cell fabricated using poly(dimethylsiloxane) (PDMS) and microelectrodes patterned onto glass microscope slides [4]. This early work was revolutionary, demonstrating that the solid electrolyte membranes used in traditional electrochemical cells could be replaced with a flowing liquid electrolyte while maintaining reactant separation. Preliminary reported measurements demonstrated an open circuit potential approximately 90% that of a traditional membrane-based cell.

The benefits of eliminating solid electrolyte membranes from electrochemical systems are significant: membranes account for between 22% and 40% of the cost of a commercial electrochemical stack, and pinhole membrane failures are a major lifetime limitation [38,57,58]. Early membrane-less systems had several significant drawbacks, however. Most importantly, at low flow rates, the coplanar electrode configuration resulted in poor reactant utilization and limiting current densities below 10 mA cm^{-2}.

The schematic shown in Figure 1-4a illustrates the cell geometry. Increasing the flow rate led to slight improvements, but the cell was still limited to roughly 80 mA cm^{-2}. These cells could not be recharged, and so were not practical from an energy storage perspective.

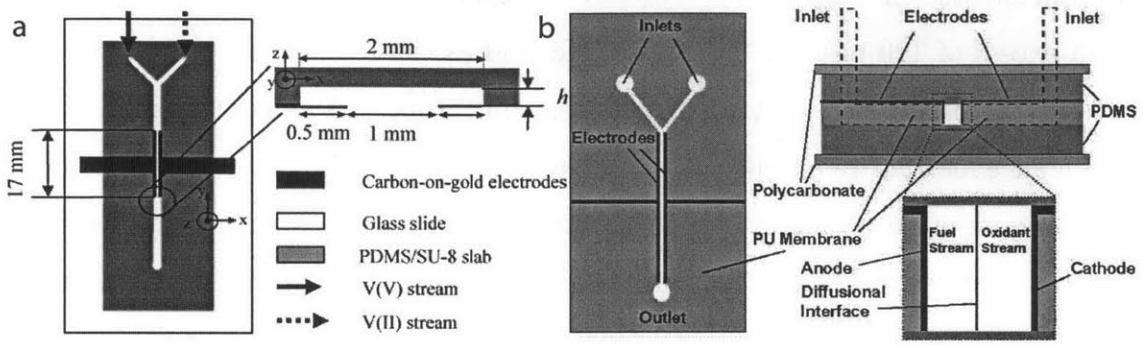

Figure 1-4: Reproduced schematic of the cell employed by Ferrigno et al. with coplanar electrodes and a vanadium redox pair [4] (a). The revised cell developed by Choban et al. employed vertical, electrodes to enhance utilization along with formic acid and dissolved oxygen as its fuel and oxidant, respectively [5] (b). Part (a) reprinted with permission from Ferrigno et al. [4]. Copyright 2002 American Chemical Society. Part (b) reproduced with permission from Choban et al. [5]. Copyright 2004 Elsevier.

Subsequent efforts attempted to remedy these deficiencies by revising the cell geometry to employ parallel electrodes to enhance reactant utilization, as well as by replacing the vanadium redox pair with formic acid and dissolved oxygen [5]. The revised cell is shown in Figure 1-4b. However, the low solubility of oxygen in aqueous solutions resulted in limiting current densities one hundred times lower than the 80 mA cm^{-2} observed by Ferrigno et al. [4]. Replacing the dissolved oxygen with potassium permanganate improved the performance by a factor of ten, indicating that the cathode was drastically limiting the cell performance [5].

Significant efforts were put into understanding these systems through both modeling and experimentation [36,60–68]. There were a number of minor revisions to this design involving fabrication techniques and geometry [69], reactant chemistry [70,71], and an effort to enhance the oxygen solubility of the oxidant fluid using a fluorinated hydrocarbon emulsion [72]. However, very limited improvements were made from a

performance standpoint until the concept of an air-breathing laminar flow fuel cell was introduced [6]. In this new cell design, illustrated in Figure 1-5b, a porous cathode allowed oxygen to diffuse to the reaction sites in contact with a liquid electrolyte, thereby avoiding the low oxygen solubility limitations that had hampered previous efforts illustrated in Figure 1-5b. The new design allowed for limiting current densities in excess of 120 mA cm^{-2} using formic acid as the fuel and air as the oxidant, as shown in Figure 1-5c, and single pass reactant utilization as high as 33%. These performance metrics were a substantial improvement, but were still significantly lower than those reported for traditional membrane-based systems, which reported current densities densities as high as 334 mA cm^{-2} [73]. Regardless, the chemical flexibility and reduced cost inherent in a membrane-less design were distinct advantages.

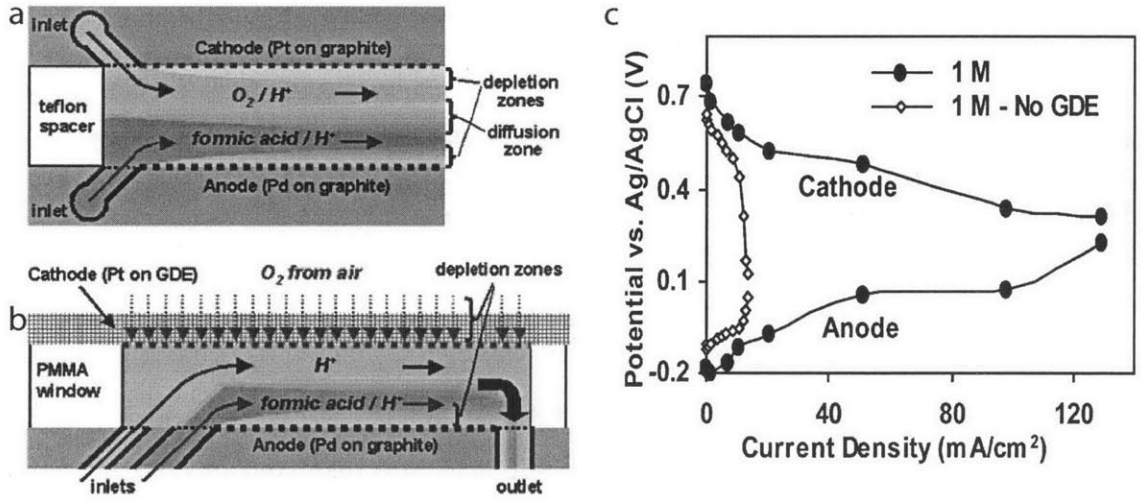

Figure 1-5: Reproduced schematic of the cell employed by Jayashree et al. compared to the earlier design employed by Choban et al. [5,6] (a and b). The new cell design incorporated a gas diffusion electrode (GDE) to allow gaseous oxygen to reach the cathode. The independent current-voltage behavior of the anode and cathode of the new cell incorporating the GDE was drastically improved compared to the original cell (c). Figures reprinted with permission from Jayashree et al. [6]. Copyright 2005 American Chemical Society.

Further iterations and modifications to air-breathing design allowed for multiple gaseous streams; a wide range of fuels and chemistries beyond formic acid were investigated, including methanol, hydrogen, hydrazine, percarbonate, and borohydride, as well as acid-base combinations [74–80]. These efforts demonstrated the value of this

architecture as a diagnostic tool, but the performance of the system was insufficient for it to be seriously considered as a power source [81–85].

A number of new designs and refinements have been proposed, including the incorporation of porous electrodes to enhance mass transfer capabilities [86–91], new flow configurations to enhance performance [92–96], chaotic mixing patterns and porous separators to produce local vortices to enhance mass transport [97–99], multi-cell stack designs [96, 100], and manufacturing and packaging improvements [101–106]. Improved modeling efforts for these new systems offer a more detailed understanding of the role of diffuse charge in flowing electrolytes [107–116]. Current densities as high as 600 mA cm^{-2} were reported for a microfluidic vanadium redox battery employing porous electrodes, resulting in a maximum power density of 300 mW cm^{-2} [91]. This level of performance constitutes a major improvement over early efforts, but was still inferior to traditional membrane-based systems [40].

1.4 Hydrogen Bromine Laminar Flow Battery

Despite the progress made in membrane-less electrochemical cells over the past decade, they have been unable to compete directly with equivalent membrane-based systems, in large part due to the excellent transport properties of the ion exchange membranes [117]. The low thickness, high conductivity, and low reactant permeability of these membranes has proven extremely effective in a number of a number of applications, including hydrogen-air fuel cells, direct methanol fuel cells, and vanadium flow batteries. Unfortunately, hydrogen bromine redox flow batteries subject their membranes to extremely challenging environments, resulting in lower conductivity and increased reactant crossover. As a result, hydrogen-bromine technologies have struggled to progress at the same rate as its peers.

The hydrogen bromine laminar flow battery (HBLFB) developed in this thesis seeks to combine the cost savings, reliability, and flexibility associated with membraneless electrochemical cells with the rapid reaction kinetics, low reactant cost, and excellent mass transfer capabilities of hydrogen bromine flow batteries. The design

builds on the porous cathode design advanced by Jayashree et al. [6] by replacing the porous cathode and solid anode with a solid cathode and a porous anode. In this configuration, aqueous bromine flows over the cathode, and is separated from the porous hydrogen anode by flowing hydrobromic acid as shown in Figure 1-6. During discharging, bromine is consumed along the cathode, forming a depletion layer. Simultaneously, a diffusion zone forms at the top of the bromine layer where bromine diffuses into the hydrobromic acid electrolyte stream. Gaseous hydrogen flows through the porous anode to generate protons that migrate to the cathode, completing the circuit as electrons are driven through an external load.

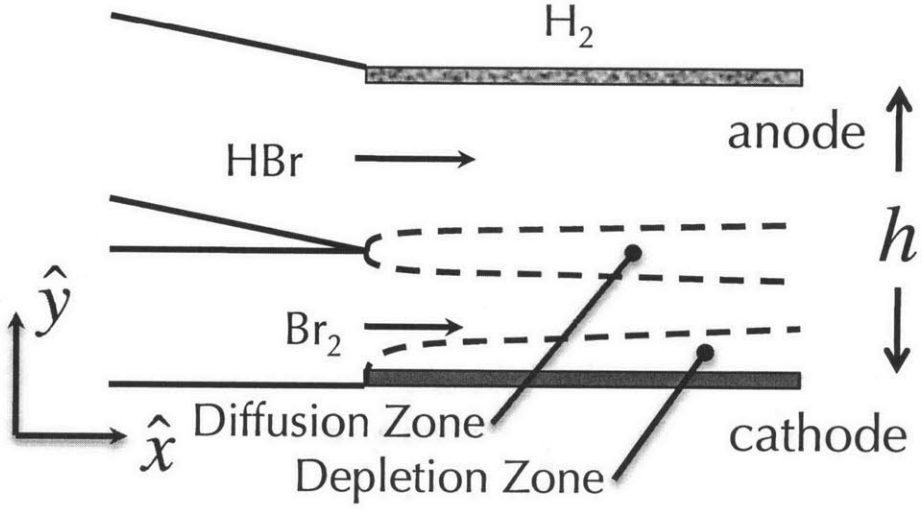

Figure 1-6: Schematic of a hydrogen-bromine laminar flow battery (HBLFB) [7].

1.5 Study Objectives and Organization

In this thesis, a new energy storage technology, the Hydrogen Bromine Laminar Flow Battery (HBLFB) is presented from a theoretical and experimental viewpoint. Critical advantages and design challenges are identified, and its potential role in grid-scale storage is investigated.

Chapter 2 examines experimental concerns involved in fabricating a demonstration-scale cell and supporting apparatus. Charging and discharging data are presented for

a range of operating conditions to determine the potential for the system to provide efficient, power-dense energy storage.

Chapter 3 looks at numerical and theoretical modeling efforts to describe the performance of the HBLFB in detail and provides greater insight into the advantages and limitations of the system. A numerical electrochemical model is developed using the finite element method to accurately describe the behavior the HBLFB under a wide range of operating conditions. A boundary layer analysis is used to derive a more general analytical model to describe the performance of the HBLFB. This analysis can also be adapted to describe the electrochemical performance of any membrane-less laminar flow electrochemical cell.

Chapter 4 addresses the inertial behavior of the flowing liquid within the HBLFB. Under certain conditions, inertial effects in both two- and three- dimensions can result in surprising flow patterns near the inlet region of the HBLFB that can enhance bromine mixing into the electrolyte, reducing cell performance.

Chapter 5 considers the greater context of large-scale energies storage. Historical data for energy pricing as well as output from hypothetical wind turbine or photovoltaic panel farms are employed to estimate the economic performance of a hybrid renewable-storage system sited in a number of sites across the Unites States, and these results are used to establish performance targets and cost tradeoffs for the development of energy storage technologies.

Finally, Chapter 6 presents the major conclusions and broader impact of the work, and discusses opportunities for future study.

Chapter 2

Experimental Investigation of the Hydrogen Bromine Laminar Flow Battery

2.1 Introduction

Low-cost energy storage remains a critical unmet need for a wide range of applications, include grid-scale frequency regulation, load following, contingency reserves, and peak shaving, as well as portable power systems [41,118–120]. For applications that require the storage of large quantities of energy economically and efficiently, flow batteries have received renewed attention [121, 122]. A wide variety of solutions have been proposed, including zinc-bromine and vanadium redox cells [41, 123]. This includes recent efforts to incorporate novel concepts such as organic electrolytes for greater voltage stability and semisolid reactants for higher reactant energy density [27, 124] or chemistries to reduce reactant cost [37, 39]. One such permutation is the hydrogen bromine flow battery [3, 19, 45, 56, 125]. The rapid and reversible reaction kinetics of both the bromine reduction reaction and the hydrogen oxidation reaction minimize activation losses [47, 126], while the low cost ($1.39 kg^{-1}) and abundance (243,000 metric tons produced per year in the United States alone) of bromine distinguishes

it from many other battery chemistries [50]. However, theoretical investigations of such systems have revealed that the perfluorosulfonic acid membranes typically used suffer from low conductivity in the absence of sufficient hydration [127, 128]. In the presence of hydrobromic acid, this membrane behavior is the dominant limitation on overall performance [52, 56].

Laminar flow electrochemical cells have been proposed to address many of the challenges that face traditional membrane-based systems [4–6,69,77,87,129]. Laminar flow cells eliminate the need for an ion exchange membrane by relying on diffusion to separate reactants. Eliminating the membrane decreases cost, relaxes hydration requirements, and opens up the possibility for a much wider range of chemistries to be investigated. This flexibility has been exploited in the literature; examples include vanadium redox flow batteries [4, 129], as well as methanol [6], formic acid [5], and hydrogen fuel cells [77]. However, none of these systems have achieved power densities as high as their membrane-based counterparts. This is largely because the proposed chemistries already work well with existing membrane technologies that have been refined and optimized over several decades. More recently, a laminar flow fuel cell based on borohydride and cerium ammonium nitrate employed a porous separator, chaotic mixing, and consumption of acid and base to achieve a power density of 0.25 W cm^{-2} [98]. This appears to be the highest previously published power density for a membrane-less laminar flow fuel cell.

In this work, we present a membrane-less Hydrogen Bromine Laminar Flow Battery (HBLFB) with reversible reactions and a peak power density of 0.795 W cm^{-2} at room temperature and atmospheric pressure. The cell uses a membrane-less design similar to previous work [6], but with several critical differences that allow it to triple the highest previously reported power density for a membrane-less electrochemical cell and also enable recharging. First, where many previous laminar flow electrochemical cell designs were limited to low current operation by the low oxygen concentration at the cathode, the HBLFB uses gaseous hydrogen fuel and aqueous bromine oxidant [4–6, 69, 77]. This allows for high concentrations of both reactants at their respective electrodes, greatly expanding the mass transfer capacity of the

system Next, both reactions have fast, reversible kinetics, with no phase change at the liquid electrode, eliminating bubble formation as a design limitation. These two characteristics of the HBLFB enable high power density storage and discharge of energy at high efficiency, while avoiding the cost and reliability issues associated with membrane-based systems.

2.2 Methods

2.2.1 Cell fabrication

A proof of concept electrochemical cell was assembled using a graphite cathode and a commercial carbon cloth gas diffusion anode with 0.5 mg cm^{-2} of platinum (60% supported on carbon) obtained from the Fuel Cell Store (San Diego, CA). The cell was housed between graphite current collectors and polyvinylidene fluoride (PVDF) porting plates as shown in Figure 2-1b. All components were fabricated using traditional CNC machining or die cutting. No additional catalyst was applied to the cathode. The hydrogen flow rate through the porous anode was 25 sccm, and an oxidant stream of bromine mixed with aqueous hydrobromic acid passed through the channel in parallel with an electrolyte stream of aqueous hydrobromic acid. An 800 μm thick Viton gasket was used to separate the two electrodes and create the channel, which was 1.4 cm long from oxidant inlet to outlet with an active area of 25 mm^2. A fixed ratio of ten to one was maintained between the electrolyte and oxidant flow rates, and the net flow rate was adjusted to study the performance of the cell as a function of the Peclet number, Pe, defined by the average flow velocity U, channel height h, and bromine diffusion coefficient D such that $\mathrm{Pe} \equiv Uh/D$.

2.2.2 Numerical model details

A scaled, dimensionless model was constructed in COMSOL Multiphysics, and results were calculated over a range of flow rates and reactant concentrations. A complete description of the model has been presented previously [7,130]. Bromine concentration

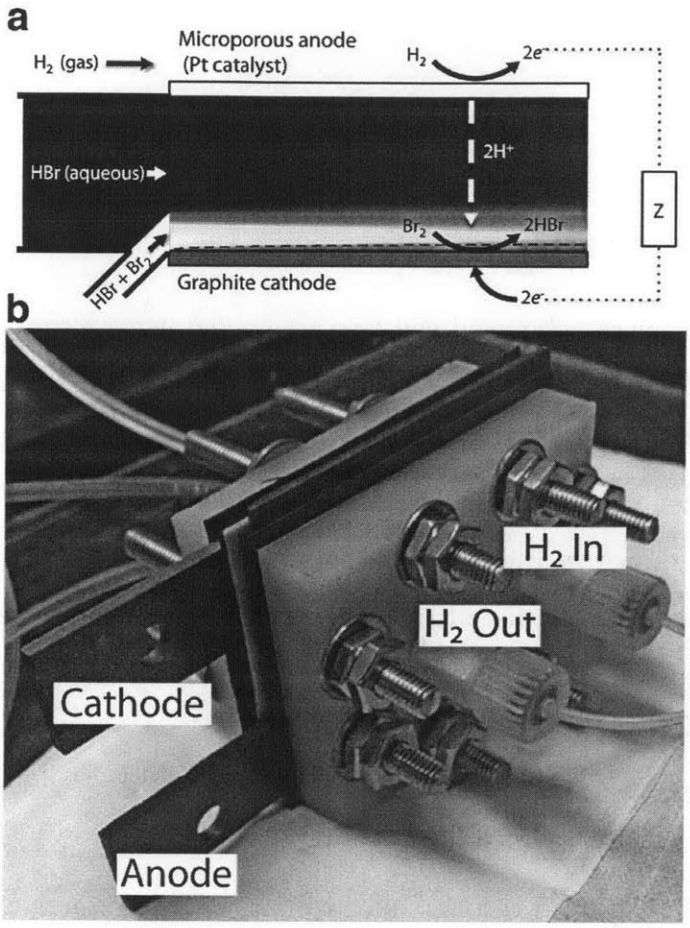

Figure 2-1: Schematic of reactant flow within the Hydrogen Bromine Laminar Flow Battery (HBLFB). During discharge, liquid bromine is reduced to hydrobromic acid along the lower solid graphite electrode, and hydrogen is oxidized at the upper porous electrode. Numerically predicted concentration of Br_2 for a Peclet number of 10,000 and initial concentrations of bromine and hydrobromic acid of 1 M is overlaid (a). Assembled cell prior to testing (b).

varied along the length of the channel, resulting in strong spatial variations in the current density, demonstrated in Figure 2-1a. Current-voltage data was obtained for a range of reactant concentrations and flow rates for comparison to experimental data by averaging the current density along the length of the cell, and calculating solutions over a range of specified cell voltages.

2.3 Results

2.3.1 Numerical model

A two-dimensional numerical model of the device was constructed to allow for a greater understanding of the underlying physics of the cell [7,130]. The model solves the Nernst-Planck equations with advection in the imposed flow for the concentrations and electrostatic potential, assuming a quasi-neutral bulk electrolyte. Fully developed Poiseuille flow was assumed in the channel, with reactions occurring at the top and bottom of the channel along thin electrodes. A schematic of the system is shown in Figure 2-1. Because the channel width far exceeds the height, edge effects can be ignored, validating the two-dimensional assumption. Equilibrium potentials along the cathode and anode were determined by the Nernst equation assuming dilute solution theory, and activation losses were estimated using the symmetric Butler-Volmer equation, consistent with existing kinetics data [47]. Electrolytic conductivity was assumed to depend on the local (spatially evolving) hydrobromic acid concentration, and was calculated using empirical data [131].

2.3.2 Discharge experiments

The cell was operated galvanostatically at room temperature and atmospheric pressure over a range of flow rates and reactant concentrations. The cell was observed to reach steady state in less than ten seconds, so each data point was collected after sixty seconds of steady state operation to eliminate transient artifacts. Polarization data was collected as a function of Peclet number for the HBLFB using 1 M HBr and 1 M

Br_2, and compared with numerical model results in Figure 2-2. The Peclet numbers of 5,000, 10,000, and 15,000 correspond to Reynolds numbers of 5.75, 11.5, and 17.25, oxidant flow rates of 0.22, 0.44, and 0.66 mL min^{-1} cm^{-2}, and mean velocities of 6.3, 12, and 19 mm s^{-1}, respectively. The oxidant flow rates correspond to stoichiometric currents of 0.7, 1.4, and 2.1 A cm^{-2} respectively. Hydrogen was flowed in excess at a rate of 25 sccm. The slightly enhanced maximum current density of the observed results compared to the predicted results may be attributed to the roughness of the electrode surface producing chaotic mixing that slightly enhances reactant transport. Below limiting current, the agreement between model and experiment is very good. At low current densities, the voltage differences between the different Peclet numbers are small, but in each case, the voltage drops rapidly as the cell approaches limiting current, corresponding to the predicted mass transfer limitations.

2.3.3 Analytical limiting current

These limitations can be estimated analytically for fast reactions by assuming a bromine concentration of zero at the cathode and applying the Lévêque approximation to the bromine depletion layer [132,133]. For a channel of length L and height h, fully developed Poiseiulle flow, and initial bromine concentration c_0, the resulting partial differential equation and boundary conditions can be expressed in terms of dimensionless bromine concentration $\tilde{c} = c/c_0$, position $\tilde{y} = y/h$ and $\tilde{x} = x/h$, channel aspect ratio $\beta = L/h$, and Peclet number $\mathrm{Pe} = Uh/D$.

$$\begin{aligned} \frac{6\mathrm{Pe}}{\beta}\tilde{y}\frac{\partial \tilde{c}}{\partial \tilde{x}} &= \frac{\partial^2 \tilde{c}}{\partial \tilde{y}^2} \\ \tilde{c}(\tilde{x}=0) &= 1 \\ \tilde{c}(\tilde{y}\to\infty) &= 1 \\ \tilde{c}(\tilde{y}=0) &= 0 \end{aligned} \tag{2.1}$$

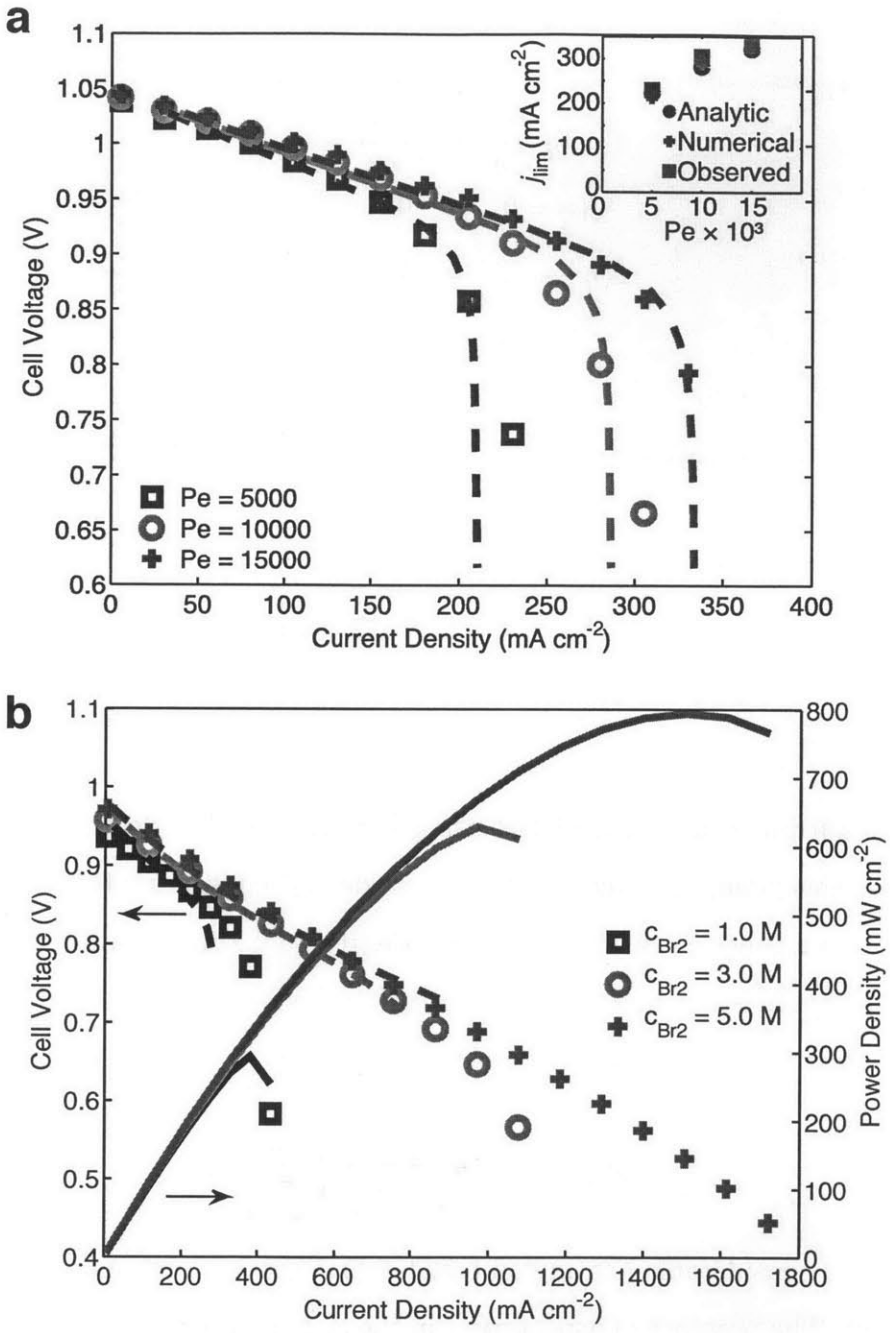

Figure 2-2: Discharge performance of the HBLFB. Predicted (dashed) and observed (dots) cell voltage and as a function of current density and Peclet number for the HBLFB during discharge using 1M Br_2 and 1M HBr. For low concentration reactants, mass transport is the dominant source of loss, and limiting current density j_{lim} can be predicted analytically as a function of Peclet number Pe using the Lévêque approximation (inset) (a). Predicted (dashed) and observed (dots) cell voltage and power density as a function of current density and Br_2 concentration for Pe = 10,000 and 3 M HBr. The higher reactant concentrations require concentrated solution theory to accurately model, but allow for much higher current and power density (b).

A similarity technique can be applied to convert this to an ordinary differential equation.

$$\begin{aligned} \eta^2 \frac{\partial \tilde{c}}{\partial \eta} &= \frac{\partial^2 \tilde{c}}{\partial \eta^2} \\ \tilde{c}(\eta = 0) &= 0 \\ \tilde{c}(\eta \to \infty) &= 1 \\ \eta &= \frac{\tilde{y}}{\sqrt[3]{\beta \tilde{x}/2\mathrm{Pe}}} \end{aligned} \tag{2.2}$$

This equation can be solved exactly in terms of the incomplete Gamma function, $\Gamma(s, a)$.

$$\tilde{c}(\tilde{x}, \tilde{y}) = \Gamma\left(\frac{2\mathrm{Pe}\tilde{y}^3}{3\beta\tilde{x}}, \frac{1}{3}\right) \tag{2.3}$$

Limiting current can be calculated using Faraday's law to determine the distribution of current along the length of the electrode and integrating to obtain limiting current j_{lim} as a function of Peclet number Pe, reactant concentration c_0 and diffusivity D, channel height h and aspect ratio β, Faraday's constant F, and the number of moles of electrons transferred per mole of reactant n.

$$j_{\mathrm{lim}} = 1.47 \frac{c_0 n D F}{h} \sqrt[3]{\frac{\mathrm{Pe}}{\beta}} \tag{2.4}$$

This result has considerable bearing on how laminar flow systems should be designed and operated. The presence of aspect ratio in the denominator means that shortening the channel results in greater power density, as observed in experiment [116]. In addition, the weak 1/3 dependence on Peclet number means that increasing the flow rate beyond a certain point yields minimal benefits. There was excellent agreement between maximum observed current density, maximum numerically predicted current density, and the analytically predicted limiting current density as a function of Peclet number, as shown in Figure 2-2a.

2.3.4 High power operation

Higher bromine concentrations were also investigated by using a more concentrated electrolyte (3M HBr) to enhance bromine solubility and move beyond the mass transfer limitations of 1 M Br_2. The performance of this system was investigated at a Peclet number of 10,000 by varying the bromine concentration, and is shown in Figure 2-2b. Using 5M Br_2 and 3M HBr as the oxidant and electrolyte respectively, a peak power density of 0.795 W cm^{-2} was observed when operated near limiting current density. This corresponds to power density per catalyst loading of 1.59 W mg^{-1} platinum. The open circuit potential of the cell dropped more than might be predicted simply using the Nernst equation at the cathode. The drop in open circuit potential is consistent with data on the activity coefficient of concentrated hydrobromic acid available in the literature, as well as previous studies that employed concentrated hydrobromic acid [19, 131]. To account for this effect, empirical data for the activity coefficient of hydrobromic acid as a function of local concentrate was incorporated into the boundary conditions. The activity coefficient was assumed to vary slowly enough within the electrolyte that gradients in activity coefficient were neglected in the governing equations. Taking into account the activity coefficient of hydrobromic acid, there is good agreement between the model and experiment. As in the low concentration data, the observed maximum current density is slightly higher than predicted. Otherwise the model captures the main features of the data, including the transition from transport limited behavior at low bromine concentrations, evidenced by a sharp drop in cell voltage, to ohmically limited behavior at high bromine concentrations. In this ohmically limited regime, mass transport limitations are less important, and the limiting current solution applied to the low concentration results does not apply.

2.3.5 Recharging and round-trip efficiency

Charging behavior was also investigated by flowing only HBr and applying a voltage to electrolyze HBr back into Br_2 and H_2. The voltage versus current density behavior of the cell was investigated during charging as a function of HBr concentration at a

Peclet number of 10,000, as shown in Figure 2-3. Experimental conditions were kept identical to those of the discharge experiments, with the exception that no bromine was externally delivered to the cell. Side reactions, in particular the formation of hypobromous acid and the evolution of oxygen become dominant before potentials get sufficiently high to observe limiting current. As a result, the numerical model cannot accurately describe the behavior at of the cell at potentials above 1.3 volts, and was not applied to the charging data. At lower voltages, both the electrolyte conductivity and the limiting current density were increased by increasing the HBr concentration, resulting in the increased performance shown in Figure 2-3. Roundtrip voltage efficiency was then calculated by dividing the discharge voltage by the charging voltage for a number of reactant concentrations. This data is plotted against power density in Figure 2-4. Voltage efficiencies slightly greater than 100% were observed for low power densities due to differences in the open circuit potential that are generated by the variation in bromine concentration between the charging and discharging experiments. This anomaly becomes unimportant at higher current densities, where the reactant concentration varies spatially much more strongly. Using high concentration reactants, roundtrip efficiency of 90% was observed when using high concentration reactants at 25% of peak power (200 mW cm^{-2} during discharge). This appears to be the first publication of roundtrip charging and discharging of a membrane-less laminar flow battery, and compares very favorably to existing flow battery technologies. Vanadium redox batteries, for example, have demonstrated voltage efficiencies as high as 91%, but only at a discharge power density nearly an order of magnitude lower than the HBLFB [134].

Although closed-loop operation was not demonstrated in this study, some insight into coulombic efficiency can be gathered by considering the effect of reactant mixing within the channel. At 25% of peak power, the single-pass coulombic efficiency of the cell is only about 1%. If no attempt were made to separate the reactants at the outlet of the cell, the resulting energy efficiency of the cell would also be very low. However, if the channel outlet were split to conserve the volume of stored electrolyte and oxidant, only the Br_2 that had diffused into the electrolyte layer would be lost.

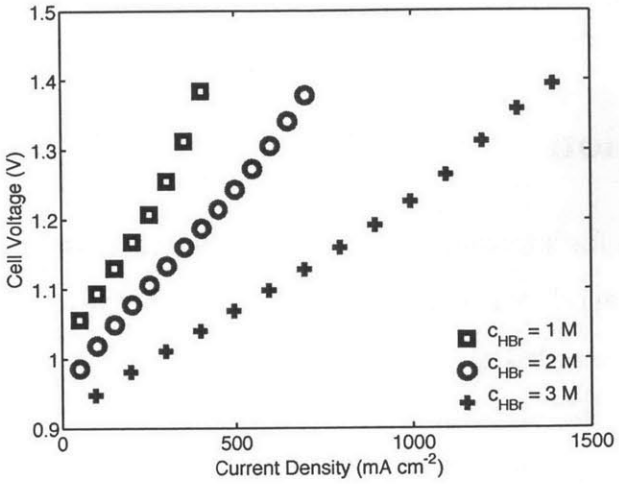

Figure 2-3: Charging performance of the HBLFB. Observed cell voltage during charging as a function of HBr concentration at a Peclet number of 10,000 and a Br_2 concentration of 1 M. Increasing the HBr increases both the conductivity and the limiting current, resulting in superior performance.

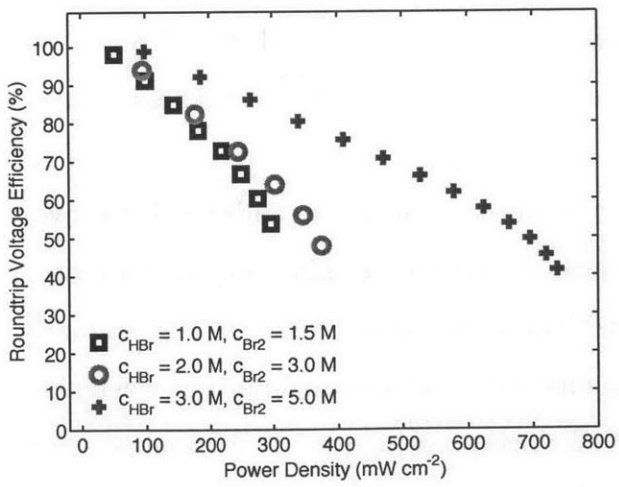

Figure 2-4: Roundtrip efficiency of the HBLFB. Round-trip voltage efficiency of the HBLFB as a function of power density for a range of reactant concentrations at a Peclet number of 10,000.

Assuming fully developed Poiseuille flow, this corresponds to a coulombic efficiency of 72%, or a roundtrip energy efficiency of 66%.

2.4 Discussion

Several opportunities for improvement on this design remain to be investigated. First, the porous hydrogen anode was selected because of its commercial availability, despite the fact that it was intended for use in a proton exchange membrane fuel cell. The catalyst composition and structure, wettability, and media porosity have not been optimized. Previous work has shown that these parameters can impact the power density of laminar flow cells by nearly an order of magnitude [83]. Recent work on thin hydrogen oxidation electrodes has demonstrated that excellent catalytic activity can be achieved with platinum loadings as low as 3 μg cm^{-2}, more than two order of magnitude lower than the electrodes used in this study [135]. Assuming equivalent performance, an HBLFB employing such a hydrogen electrode would have a specific power density of roughly 250 W mg^{-1} platinum, virtually eliminating platinum as a cost-limiting component of the system. Second, the channel geometry used in these experiments was relatively long in order to achieve high oxidant utilization. Shortening the channel would decrease the average thickness of the depletion layer that develops along the cathode, enabling higher current densities [116]. That enhanced power density must be balanced against the additional inactive area created due to gasketing around the actual channels to minimize system cost. This effect is examined in more detail in Chapter 6. Third, reducing the distance between electrodes would greatly reduce ohmic losses, which are dominant when high concentration reactants are fed into the cell. Incorporating further refinements, such as micro patterned chaotic mixing patterns coupled with a non-specific convection barrier or non noble metal catalysts could also improve performance. [97, 98, 136].

The initial data presented here for the HBLFB suggests that high power density and high efficiency energy storage is achievable using a membrane-less electrochemical cell operating at room temperature and pressure. The HBLFB requires no

special procedures or facilities to fabricate, and uses kinetically favorable reactions between abundant, low cost reactants. Recent work has shown that a membrane-based hydrogen-bromine flow battery at room temperature can generate 850 mW cm^{-2}, or 7% more power than these experiments with the HBLFB at room temperature [3]. However, this was achieved using a stoichiometric oxidant flow rate over 8 times larger than that used in this work, as well as an acid-treated porous bromine electrode with substantially greater active area than the HBLFB's bare graphite bromine electrode.

This work represents a major advance of the state of the art in flow batteries. To the best of the authors' knowledge, the data presented here represent the highest power density ever observed in a laminar flow electrochemical cell by a factor of three, as well as some of the first recharging data for a membrane-less laminar flow electrochemical cell [91, 98]. Although previous work has identified the appropriate scaling laws [62, 137], the result presented here represents the first exact analytical solution for limiting current density applied to a laminar flow electrochemical cell, and serves as a guide for future designs. The HBLFB rivals the performance of the best membrane-based systems available today without the need for costly ion exchange membranes, high pressure reactants, or high temperature operation. This system has the potential to play a key role in addressing the rapidly growing need for low-cost, large-scale energy storage and high efficiency portable power systems.

Chapter 3

Boundary Layer Analysis of Membrane-less Electrochemical Cells

3.1 Introduction

Since they were first developed over ten years ago, membrane-less laminar-flow electrochemical cells have attracted considerable attention [4, 5, 87, 138, 139]. Compared to traditional electrochemical cells, these systems eliminate the need for a membrane by relying on laminar flow and the slow molecular diffusion of reactants to ensure separation of the two half-reactions. Significant cost reductions go along with removing the membrane, which has been estimated to account for between 22% and 40% of the overall stack cost, making it the single most expensive stack component [38, 57, 58]. In addition, the balance of plant is simplified by avoiding any membrane hydration requirements. Chemical limitations imposed by the membrane are also eliminated, allowing for the use of a wide range of electrolytes, fuels, oxidants, and catalysts [77, 82, 85, 98, 129, 140].

The inherent advantages of this technology for micro and small-scale mobile power applications were identified early in the development of these systems [4]. but the mass

transfer limitations present in these devices have limited their overall power density and applicability. A number of new concepts have been incorporated to improve performance, including porous separators to minimize crossover [98, 99], air-cathodes to enhance oxygen transport [6], patterned electrodes to enhance chaotic mixing [97,141], and flow-through porous electrodes to enhance fuel utilization [4,5,87,90,91,138,139], but the fundamental limitations of the technology largely remain. Previous efforts to model laminar flow systems have focused on either channel geometry and flow optimization [57, 62, 66, 79], or more detailed examination of the impact of reactant crossover and diffuse charg [77, 82, 85, 98, 110, 112, 129, 140]. However, these models have required computationally intensive numerical techniques, with solutions requiring as much as several hours of processor time to compute, and they provide limited analytical insights. The purpose of this work is to derive accurate scaling laws and theoretical guidelines that can be applied to the future design of membrane-less electrochemical cells. The ability of these systems to maintain reactant separation is of particular importance, and previous work has independently established scaling laws for mixing colaminar flow in microchannels [4, 137, 142–145]. We present numerical and approximate analytical solutions of a general mathematical model that couples these scaling laws to a Nernst-Planck description of ion transport. The theory is developed for laminar electrochemical cells with Poiseuille or plug flow between flat electrodes, but the model equations could be applied to any fluidic architecture with appropriate flow profiles.

The general theory is illustrated by successful application to the Hydrogen Bromine Laminar Flow Battery (HBLFB) [98, 99, 137, 144]. Although the theory can be applied to a range of systems, the HBLFB makes for an appealing model system for two major reasons. Firstly, the reaction kinetics for both half-cell reactions in the HBLFB are sufficiently fast and reversible that activation overpotentials are minimal for both charging and discharging, emphasizing mass transport and ohmic losses in the system. Secondly, the HBLFB is the only membrane-less laminar flow electrochemical system for which there exists sufficient published polarization data to validate the theory for both charging and discharging [146]. HBLFB uses a membrane-less laminar flow

design with aqueous bromine serving as the oxidant and gaseous hydrogen as the fuel. The system is reversible, producing hydrobromic acid in discharge mode and recovering bromine and hydrogen in charging mode, with high round-trip efficiency. Although this system differs from many existing membrane-less electrochemical cells in that it uses a liquid oxidant and gaseous fuel, the rapid reaction kinetics at both electrodes minimize activation losses and make for an appealing model system. These characteristics have also been shown to allow the HBLFB to achieve power densities as high as 795 mW cm^{-2}, with a round-trip voltage efficiency of 90% at 25% of peak power in its first iteration [6, 146]. The full model in two dimensions can be solved numerically using finite elements to predict the performance of the HBLFB, as well as to better understand the sources of loss and how they can be mitigated. The focus of this work, however, is to derive simple, but accurate, approximate solutions by boundary-layer analysis, which can be used to quickly establish the relative importance of the various sources of loss and interpret experimental data. Analogous efforts have been made to describe the performance of membrane-based fuel cells [147, 148]. Although there has been some work analyzing the current-voltage behavior of laminar flow electrochemical cells, this appears to be the first study to provide closed-form analytical solutions [97, 115, 141]. By accurately predicting the behavior of the HBLFB with minimal computational expense, the analytical model can serve as a guide for future design of laminar flow electrochemical cells.

3.2 Mathematical Model

The laminar flow electrochemical cell consists of two flat electrodes with flowing electrolyte separating them. The flow within the channel is assumed to be fully developed and laminar. The length of the channel L is assumed to be much greater than the spacing h between the electrodes or the channel width w, so that edge effects can be neglected. Two canonical cases of unidirectional flow are considered. In the first case, $h \ll w$, so the flow is roughly uniform in the z direction, and adopts a parabolic velocity profile between the electrodes as shown in Figure 3-1a.

In the second case $w \ll h$, and the velocity profile can be depth-averaged in the z direction to arrive at a uniform velocity profile between the electrodes as shown in Figure 3-1b. This Hele-Shaw type flow can generally be described as a potential flow. There is a third case, in which a channel of arbitrary shape contains a porous medium, and the flow obeys Darcys Law. The flow can be treated in the same manner as the potential flow case, as shown in Figure 3-1c. Ion transport is governed by the Nernst-Planck equations, which predict concentration polarization, leading to variations in bulk conductivity [143]. The electrostatic potential is determined by bulk electroneutrality across the entire channel, since the typical channel dimensions ($\sim$ 100 μm – 1 cm) are much larger than the Debye screening length ($\sim$ 1 nm) for aqueous electrolytes with concentrations of 0.1 M or greater, as is the case with the HBLFB [143]. For such thin Debye lengths, Frumkin effects of double-layer charge on reaction kinetics can also be neglected [149, 150]. For common reactants, electrolytes, and concentrations in the range of 1 – 3 M, activity coefficients are near unity, so dilute solution theory can be applied with no loss in accuracy [131]. It would be straightforward to account for the impact of non-unity activity coefficient or additional charged species on transport [143] and reaction kinetics [151] in numerical simulations, but analytical progress would be more difficult.

3.2.1 Example: Hydrogen bromine laminar flow battery

For the HBLFB during discharge, the two half-cell reactions are the oxidation of hydrogen at the anode, and the reduction of bromine at the cathode.

$$\begin{aligned} \text{Anode: } H_2 &\rightarrow 2H^+ + 2e^- \\ \text{Cathode: } 2e^- + Br_2 &\rightarrow 2Br^- \end{aligned} \tag{3.1}$$

For the purpose of this work, the electrodes are assumed to be thin so the reactions can be treated as heterogeneous. A microporous anode is assumed to provide sufficient hydrophobicity such that it creates a thin interface between liquid electrolyte in the open channel and gaseous hydrogen in the electrode. Therefore, no

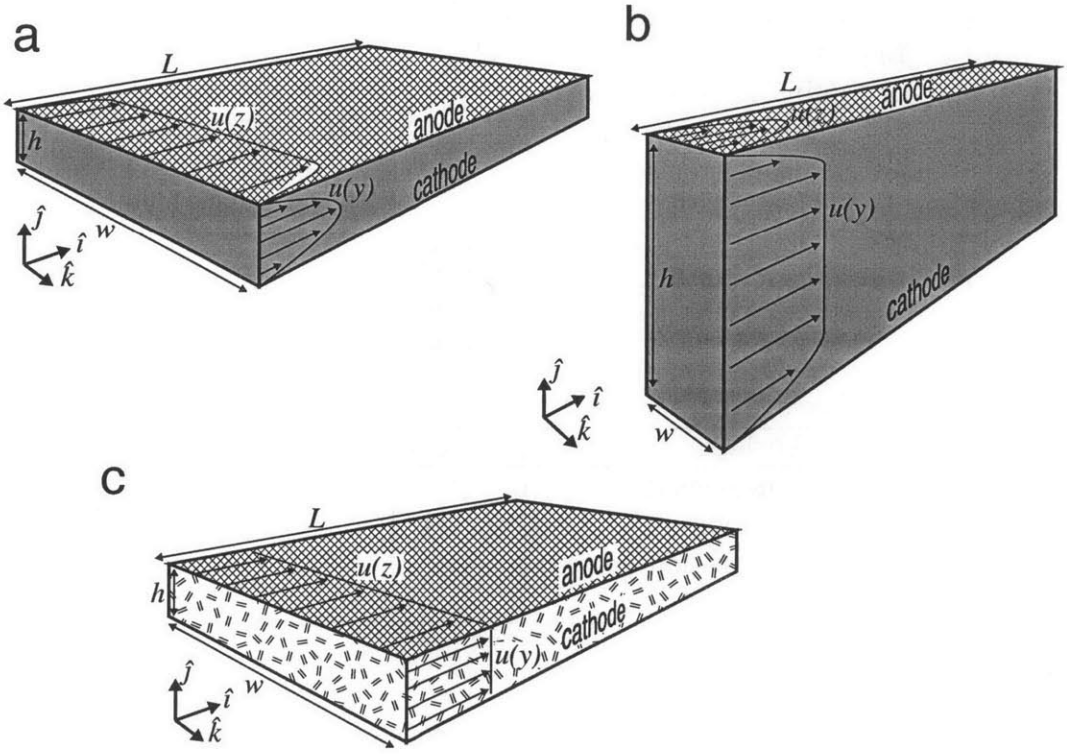

Figure 3-1: Domain for the membrane-less electrochemical cell model. For wide, short channels (a), a parabolic flow profile can be assumed. For tall, narrow channels (b), a depth-averaged plug flow profile can be assumed. If the channel contains a porous medium (c), the flow profile will be similar to (b).

Table 3.1: Model parameters and variables for the Hydrogen Bromine Laminar Flow Battery.

Parameter	Symbol	Value
Ideal gas constant	R	8.314 J mol^{-1} K
Temperature	T	298 K
Faraday's constant	F	96485 C mol^{-1}
Channel height	h	800 μm
Channel length	L	1.30 cm
Mean flow velocity	U	1.44 cm/s
Br_2 diffusion coefficient	D_{Br2}	1.15×10^{-5} cm^2 s^{-1}
Br^- diffusion coefficient	D_{Br-}	2.08×10^{-5} cm^2 s^{-1}
H^+ diffusion coefficient	D_{H+}	9.31×10^{-5} cm^2 s^{-1}
Br_2 exchange current density	K_c^0	0.5 A cm^2
HBr exchange current density	K_a^0	0.5 A cm^{-2}
Br_2 inlet concentration	c_{Br2}^0	1.0 M
HBr inlet concentration	c_{HBr}^0	1.0 M
Cell potential	φ_{cell}	0.900 V
Aspect ratio	β	16.25
Peclet Number	Pe	10^4
Variable	Symbol	Dimensionless Scale
Current density	j	$nD_iFc_i^0/h$
Position	(x, y)	(L, h)
Concentration	c_i	ci^0
Ionic potential	φ	RT/F

gas intrudes into the channel, and no liquid intrudes into the electrode. The entire cell is assumed to be isothermal and isobaric at standard temperature and pressure. The electrolyte is assumed to be quasineutral at high salt concentration, and reaction kinetics are typically fast compared to bulk diffusion [114]. Reaction rate constants are estimated based on values quoted in the literature, although because activation losses are minimal in this system, the model is not sensitive to these values [47]. The relevant parameters and their nominal values are listed in Table 3.1.

3.2.2 Governing equations in the electrolyte

The species present in the channel are the reactant bromine and the product hydrobromic acid. The geometry of the channel is shown schematically in Figure 3-1a, so

fluid flow is assumed to be fully developed Poiseuille flow in a channel, and is treated as a model input.

$$\vec{u} = 6U\left(\frac{y}{h} - \frac{y^2}{h^2}\right)\hat{i} \tag{3.2}$$

Reactions occur only at the boundaries, so species and current conservation is maintained within the channel. Species flux $\vec{N}_i$ and ionic current $\vec{J}$ can be expressed by applying dilute solution theory and using the Nernst Planck equations in terms of the parameters listed in Table 3.1, species concentrations c_i, and dimensionless ionic potential $\tilde{\varphi}$, scaled to the thermal voltage RT/F.

$$\begin{aligned}
\vec{N}_{\mathrm{H+}} &= -D_{\mathrm{H+}}(\nabla c_{\mathrm{H+}} + c_{\mathrm{H+}}\nabla\tilde{\varphi}) + \vec{u}c_{\mathrm{H+}} \\
\vec{N}_{\mathrm{Br-}} &= -D_{\mathrm{Br-}}(\nabla c_{\mathrm{Br-}} - c_{\mathrm{Br-}}\nabla\tilde{\varphi}) + \vec{u}c_{\mathrm{Br-}} \\
\vec{N}_{\mathrm{Br2}} &= -D_{\mathrm{Br2}}\nabla c_{\mathrm{Br2}} + \vec{u}c_{\mathrm{Br2}} \\
\vec{J} &= F(\vec{N}_{\mathrm{H+}} - \vec{N}_{\mathrm{Br-}})
\end{aligned} \tag{3.3}$$

Because electroneutrality and a binary electrolyte are assumed, the concentration of protons and bromide ions are equal, and the governing equations can be simplified by defining an ambipolar diffusion coefficient $D_{\mathrm{HBr}} = 2D_{\mathrm{H+}}D_{\mathrm{Br-}}/(D_{\mathrm{H+}} + D_{\mathrm{Br-}})$ [133].

$$\begin{aligned}
\vec{N}_{\mathrm{HBr}} &= -D_{\mathrm{HBr}}\nabla c_{\mathrm{HBr}} + \vec{u}c_{\mathrm{HBr}} \\
\vec{N}_{\mathrm{Br2}} &= -D_{\mathrm{Br2}}\nabla c_{\mathrm{Br2}} + \vec{u}c_{\mathrm{Br2}} \\
\vec{J} &= F(D_{\mathrm{H+}} - D_{\mathrm{Br-}})\nabla c_{\mathrm{HBr}} + F(D_{\mathrm{H+}} + D_{\mathrm{Br2}})c_{\mathrm{HBr}}\nabla\tilde{\varphi}
\end{aligned} \tag{3.4}$$

3.2.3 Anode boundary conditions

The anode is assumed to be exposed to isobaric hydrogen at standard temperature and pressure, so the anode itself is not explicitly included in the model. However, the potential drop across the interface between the grounded anode and the electrolyte determines the ionic potential φ at the boundary $y = h$. The potential drop is a function of the equilibrium half-cell potential $\tilde{\varphi}_{\mathrm{a}}^{\mathrm{eq}}$, modeled by the Nernst equation, and activation overpotential η_{a}, modeled by the symmetric Butler-Volmer equation. Hydrogen oxidation/evolution is accomplished with 0.5 mg cm^{-2} loading of platinum at the anode to ensure rapid reaction kinetics, and to be consistent with existing best practices [3, 19, 45, 56]. These quantities are coupled to both the local acid concentration c_{HBr} and the local current density $j = \hat{n} \cdot \vec{J}$ normal to the boundary.

$$\begin{aligned} \varphi(x, y = h) &= -\varphi_{\mathrm{a}}^{\mathrm{eq}}(c_{\mathrm{HBr}}) + \eta_{\mathrm{a}}(c_{\mathrm{HBr}}, j) \\ \varphi_{\mathrm{a}}^{\mathrm{eq}} &= \varphi_{\mathrm{a}}^{0} + \frac{RT}{F} \ln(c_{\mathrm{HBr}}) \\ \eta_{\mathrm{a}}(c_{\mathrm{HBr}}, j) &= \frac{RT}{F} \sinh^{-1}\left(\frac{j}{2K_{\mathrm{a}}^{0} c_{\mathrm{HBr}}}\right) \end{aligned} \tag{3.5}$$

Because the hydrogen concentration is assumed to be constant, it does not appear in these three equations, which can be combined to form a coupled, nonlinear boundary condition for potential at $y = h$, and simplified by noting that standard potential at the anode is zero volts referenced to the standard hydrogen electrode.

$$j = 2K_{\mathrm{a}}^{0} c_{\mathrm{HBr}} \sinh\left(\frac{F\varphi}{RT} + \ln c_{\mathrm{HBr}}\right) \tag{3.6}$$

Faraday's Law determines species conservation by noting that at the anode, the active species is protons, while the bromide ions are static, and, assuming there is no crossover, bromine plays no role in the reaction.

$$
\begin{aligned}
N_{\mathrm{Br2}} &= 0 \\
N_{\mathrm{Br-}} &= 0 \\
N_{\mathrm{H+}} &= j/F
\end{aligned} \tag{3.7}
$$

These equations for bromide and proton flux can be combined using the ambipolar diffusion coefficient.

$$
N_{\mathrm{HBr}} = -\frac{D_{\mathrm{HBr}}}{2D_{\mathrm{H+}}}\frac{j}{F} \tag{3.8}
$$

3.2.4 Cathode boundary conditions

The cathode adds in the consumption of bromine, but is otherwise very similar to the anode. The potential boundary condition at $y = 0$ reflects the concentration dependent and spatially varying equilibrium potential of the bromine reduction reaction, $\varphi_{\mathrm{c}}^{\mathrm{eq}}$, and the non-zero cathode potential, φ_{cell}, which is a model input parameter.

$$
\varphi(x, y = 0) = \varphi_{\mathrm{cell}} - \varphi_{\mathrm{c}}^{\mathrm{eq}}(c_{\mathrm{Br2}}, c_{\mathrm{HBr}}) - \eta_{\mathrm{c}}(c_{\mathrm{Br2}}, c_{\mathrm{HBr}}, j) \tag{3.9}
$$

This expression can be rewritten as a coupled, nonlinear, mixed boundary condition by combining the impact of bromine activity with the equilibrium potential and activation overpotential. As discussed earlier, dilute solution theory is assumed with reference conditions of 1 molar bromine and 1 molar hydrobromic acid, such that species activity is equal to species concentration.

$$
j = -2K_{\mathrm{c}}^{0}\sqrt{c_{\mathrm{Br2}}}c_{\mathrm{HBr}}\sinh\left(\frac{F}{RT}(\varphi + \varphi_{\mathrm{c}}^{0} - \varphi_{\mathrm{cell}}) + \frac{1}{2}\ln\left(\frac{c_{\mathrm{Br2}}}{c_{\mathrm{HBr}}^{2}}\right)\right) \tag{3.10}
$$

Faraday's Law again describes species conservation, and the species flux can be expressed as an effective ambipolar flux by observing that the active species at the cathode is the bromide ion, with no contribution from protons. An interesting aspect of this result is that although the ionic flux at the cathode and anode are identical for a given current, the apparent ambipolar flux at the cathode is larger due to the slower diffusion of bromide ions relative to protons.

$$\begin{aligned} N_{\mathrm{Br2}} &= \frac{j}{2F} \\ N_{\mathrm{HBr}} &= -\frac{D_{\mathrm{HBr}}}{2D_{\mathrm{Br\text{-}}}}\frac{j}{F} \end{aligned} \tag{3.11}$$

The standard potential of aqueous bromine is known to be 1.087 V [131]. However, in the presence of bromide ions, bromine complexes into tribromide with an equilibrium coefficient of 17 L/mol [152]. At the concentrations probed in this study, tribromide replaces bromine as the dominant reactant species in the oxidant stream. Past efforts with numerical simulations have attempted to model how homogeneous reactions between bromine and tribromide affect the behavior of bromine reduction. However, these simulations are only tractable under very limited circumstances and are completely dependent on the uncharacterized relationship between the reaction rate constants governing tribromide formation and those governing bromine reduction [153]. For the purpose of this work, this question is addressed by using the standard potential and diffusion coefficient for tribromide ions in place of bromine [131, 154].

3.2.5 Inlet and outlet boundary conditions

Electroneutrality dictates that zero flux boundary conditions are applied for the ionic potential at both the inlet and the outlet. At the outlet, zero diffusive flux boundary conditions are applied to both species. At the inlet, Dirichlet boundary conditions are imposed on both species. A constant initial acid concentration is applied to the entire inlet. The bromine is hydrodynamically focused to form a thin layer near the

cathode by fixing an electrolyte to oxidant flow ratio of 10:1. For Poiseuille flow in a channel, this corresponds to an oxidant layer thickness of $y^* = 0.186h$ at the inlet.

3.3 Boundary Layer Analysis

The full model can be solved numerically with finite-element discretization (using COMSOL Multiphysics software, Burlington, MA), and results are given below. The numerical solution is valuable in that it allows for a deconstruction of the source of loss, and provides a tool to predict and understand the performance of experimental systems. However, it is computationally expensive to perform these simulations, with complete polarization curves often taking many hours to compute on a 2.4 GHz quad-core Intel processor. It would be desirable to derive simple formulae to immediately predict the performance and behavior of any laminar flow system with no specialized computational hardware or software. This can be done by boundary-layer analysis for forced convection in the cases of plug flow and Poiseuille flow discussed earlier [149]. The simplest case to consider is a cell with fast reactions and highly conductive electrolyte operating at limiting current. In this case, reactant flows into the cell at $x = 0$ with a constant concentration and is quickly consumed at the electrode at $y = 0$, so the reactant concentration there is zero. Next, these assumptions are lifted, and the analytical approximation is extended to under-limiting current and finite electrolyte conductivity, while maintaining good accuracy over a wide range of system parameters.

3.3.1 Plug flow

This problem is a special case of advection-diffusion in potential flow past a slipping adsorbing boundary [155,156], which has been studied recently in the context of solidification from a flowing melt [157] and particle aggregation or electrodeposition from flowing solutions [158]. Here, potential flow can be justified if the flow channel is either filled with an uncharged porous medium or thin in the transverse (z) direction ($w \ll h, L$), like a single two-dimensional pore, or Hele-Shaw cell as shown in Fig-

ures 3-1b-c. In both cases, the flow is governed by Darcys law and the fluid pressure acts as a velocity potential so long as capillary effects can be neglected, which is the case in systems like the HBLFB where there are no phase boundaries within the channel. Although the assumption of plug flow may seem restrictive, the same solution can be conformally mapped to any geometry of potential flow in two dimensions, such as curved, bent, corrugated or rough channels [156–158]. This mathematical transformation, based on the conformal invariance of the Nernst-Planck equations with advection in potential flow [155], preserves the scaling relationships derived below and underscores the generality of the boundary-layer theory. To clarify scalings and simplify the analysis, the governing equation for reactant transport is made dimensionless by defining the Peclet number as $\mathrm{Pe} = Uh/D_i$, along with the dimensionless position $(\tilde{x}, \tilde{y}) = (x/L, y/h)$, concentration $\tilde{c}_i = c_i/c_i^0$, and channel aspect ratio $\beta = L/h$. In the relevant limit of large Peclet numbers, advection dominates diffusion in the axial direction after a very short entrance region, $x \gg D_i/U$, or $\tilde{x} \gg (\beta \mathrm{Pe})^{-1}$. All dimensionless variables are delineated with a tilde. The advection-diffusion equation shown in Equation 3.4 then takes a very simple form,

$$\frac{\mathrm{Pe}}{\beta}\frac{\partial \tilde{c}_i}{\partial \tilde{x}} = \frac{\partial \tilde{c}_i}{\partial \hat{x}} = \frac{\partial^2 \tilde{c}_i}{\partial \tilde{y}^2}, \tag{3.12}$$

which is equivalent to the transient diffusion equation, where the distance traveled downstream in the plug flow is analogous to time for transverse diffusion between the electrodes. The appropriate imensionless variable is the axial position, $\hat{x} = \tilde{x}\beta/\mathrm{Pe} = x/x_e$, scaled to the entrance length, $x_e = Uh^2/D_i$, for forced convection [159]. The classical spreading solution of the diffusion equation yields a similarity solution for the reactant concentration [155–157],

$$\tilde{c}_i(\tilde{x}, \tilde{y}) = \mathrm{erf}\left(\sqrt{\frac{\mathrm{Pe}}{4\tilde{x}\beta}}\tilde{y}\right) = \mathrm{erf}\left(\frac{\tilde{y}}{2\sqrt{\hat{x}}}\right). \tag{3.13}$$

The solution describes a 99% depletion boundary layer of dimensionless thickness, $\tilde{\delta} = 3.64\sqrt{\hat{x}}$, having a parabolic shape, $\tilde{x} \sim \tilde{y}^2$. Faraday's law can then be used to

relate the reactant flux to the electrode to the local dimensionless current density $\tilde{j} = hj/nD_iFc_i^0$ in a pointwise manner along the length of the channel in terms of the number of moles of electrons transferred per mole of reactant n.

$$\tilde{j}_{\text{lim}}(\hat{x}) = \sqrt{\frac{1}{\pi\hat{x}}} \tag{3.14}$$

3.3.2 Poiseuille Flow

Next we consider viscous flow in a free electrolyte channel between the electrodes. If the electrode spacing is much thinner than the channel width, then fully developed, unidirectional flow can be assumed with a parabolic Poiseuille flow profile. At sufficiently high Peclet numbers, the depletion layer of reactant near the electrode is thin relative to the electrode spacing, and the quadratic term in the flow profile can be neglected to simplify the advection diffusion equation. The equation can be simplified further by neglecting axial diffusion, as was done in the plug flow case.

$$\frac{6\text{Pe}}{\beta}\tilde{y}\frac{\partial\tilde{c}_i}{\partial\tilde{x}} = 6\tilde{y}\frac{\partial\tilde{c}_i}{\partial\hat{x}} = \frac{\partial^2\tilde{c}_i}{\partial\tilde{y}^2} \tag{3.15}$$

This approximation for the advection-diffusion boundary layer in viscous shear flow at a no-slip surface was first proposed by Lévêque [159,160] who obtained an exact solution widely used in theories of heat and mass transfer by forced convection [159] and electrodialysis [133]. The solution can be written in terms of the incomplete gamma function, $\Gamma(s,a)$.

$$\begin{aligned} \tilde{c}_i &= \Gamma\left(\frac{2\tilde{y}^3}{\hat{x}}, \frac{1}{3}\right) \\ \Gamma(s,a) &= \frac{\int_0^s e^{-t}t^{a-1}dt}{\int_0^\infty e^{-t}t^{a-1}dt} \end{aligned} \tag{3.16}$$

The 99% boundary layer thickness now scales as the cube-root of the axial position,

$\tilde{\delta} = 1.11\sqrt[3]{\hat{x}}$. Faraday's law can again be applied to this result to derive the local dimensionless limiting current distribution in terms of the complete Gamma function $\Gamma(a)$ using the same process as in the case of plug flow. A highly conductive electrolyte and fast reactions are assumed, therefore cell voltage will not change significantly until limiting current is reached, so the power of the system will be proportional to the limiting current.

$$\tilde{j}_{\text{lim}}(\hat{x}) = \sqrt[3]{\frac{18}{\hat{x}}}\frac{1}{\Gamma(1/3)} \tag{3.17}$$

The inverse cube root behavior of the limiting current along the length of the electrode is a general consequence of the boundary layer scaling noted above [137, 144, 149] and also arises in the theory of electrodialysis [133]. The same analysis also generally relates the dimensionless flux in heat transfer (Nusselt number) or mass transfer (Sherwood number) to the Peclet number for forced convection in the entrance region of a pipe [159]. It stands in contrast to the inverse square root behavior of current density in the plug flow case, but in both cases, there is a maximum in current density near the inlet of the cell, followed by a gradual drop off along the length of the channel. Both of these results can also be integrated along the length of the channel to determine the average limiting current density, as shown in Table 3.2. Although exact conformal invariance does not hold for viscous flow, the same scaling relationships also apply to advection-diffusion viscous flows in more complicated geometries [159].

3.3.3 Reactant crossover

The absence of a physical barrier between the electrodes makes reactant crossover a primary concern in membrane-less systems. The growth of the mixing layer in a laminar channel as reactants diffuse away from their respective electrodes into the separating electrolyte has been well described before, and can be directly applied here [144]. In the case of plug flow, there is no local strain rate, so the mixing region

Table 3.2: Comparison of limiting current behavior for plug flow and Poiseuille flow profiles predicted by boundary-layer analysis expressed in terms of Peclet number Pe, aspect ratio β, dimensionless reactant layer thickness $\tilde{y}^*$, and dimensionless channel position $(\hat{x}, \tilde{y})$.

Variable	Plug Flow	Poiseuille Flow
Flow profile $\tilde{u}(\tilde{y})$	Pe	$6\text{Pe}(\tilde{y} - \tilde{y}^2)$
Local current density $\tilde{j}_{\text{lim}}(\hat{x})$	$\sqrt{1/(\pi\hat{x})}$	$\sqrt[3]{18/\hat{x}}\Gamma(1/3)$
Average current density $\bar{j}_{\text{lim}}$	$2\sqrt{\text{Pe}/(\pi\beta)}$	$3\sqrt[3]{9\text{Pe}/(4\beta)}/\Gamma(1/3)$
99% depletion layer thickness $\tilde{\delta}$	$3.64\sqrt{\hat{x}}$	$1.11\sqrt[3]{\hat{x}}$
Reactant utilization γ	$(2/\tilde{y}^*)\sqrt{\beta/(\pi\text{Pe})}$	$(3\beta/(2\text{Pe}))^{2/3}/(\tilde{y}^{*2}\Gamma(1/3))$

grows as $\tilde{\delta}_m = 3.64\sqrt{\hat{x}}$ everywhere in the channel. This results in a maximum channel aspect ratio to ensure that the mixing region does not reach across the channel.

$$\beta_{\text{mixing}} \ll 0.755\text{Pe} \tag{3.18}$$

Hydrogen crossover from anode to cathode can be treated similarly, albeit with a slightly different Peclet number to reflect the slightly faster diffusion of hydrogen in water compared to bromine. In reality, neither of these effects are major limitations on system design. In the example of the HBLFB, the channel would have to be almost a meter long before mixing became an issue.

The situation is more complicated for Poiseuille flow due to the variable strain rate across the channel. Near the center of the channel, the flow is nearly uniform, and the mixing region grows as $\tilde{\delta}_m \sim \sqrt{\hat{x}}$, just like the plug flow case. However, as the mixing region nears the edges, the strain rate increases and the mixing region slows down to $\tilde{\delta}_m \sim \sqrt[3]{\hat{x}}$. Numerical methods are required to solve for the intermediate regions between these two limits [137,144], but mixing region growth will be bounded by the plug flow case, and can again be ignored for most systems.

3.3.4 Coulombic efficiency

In a real system, coulombic efficiency is also a significant concern, since low coulombic efficiency hurts overall energy efficiency. Coulombic efficiency γ is defined as the ratio of reactant consumed at the electrode to total reactant flux into the channel, and can be expressed in terms of the initial location of the reactant electrolyte interface, $\tilde{y}^*$. For the case of plug flow,

$$\gamma = \frac{\beta \int_0^{\beta/\mathrm{Pe}} \tilde{j}_{\mathrm{lim}}(\hat{x}) d\hat{x}}{\int_0^{\tilde{y}^*} \tilde{u}(\tilde{y}) d\tilde{y}} = \frac{2}{\tilde{y}^*} \sqrt{\frac{\beta}{\pi \mathrm{Pe}}}. \tag{3.19}$$

Comparing Equation 3.19 with the average current density in Table 2REF shows that there is a tradeoff between coulombic efficiency and limiting current density. Increasing the Peclet number or decreasing the aspect ratio will increase limiting current at the same rate that it decreases coulombic efficiency, such that their product is a constant.

$$\gamma \cdot \tilde{j}_{\mathrm{lim}} = \frac{4}{\pi \tilde{y}^*} \tag{3.20}$$

As long as cell voltage is not heavily influenced by ohmic losses, this results in a balancing act between power and utilization. This inherent compromise must be considered in the design of any membrane-less electrochemical cell. A similar analysis can be performed for Poiseuille flow, with the results for a thin reactant layer summarized in Table 3.2. As in the case of plug flow, an increase in current always results in a decrease in utilization.

Regardless of the flow profile, decreasing $\tilde{y}^*$ has the immediate effect of increasing utilization up to the point where the depletion boundary layer $\tilde{\delta}$ is thicker than the reactant layer $\tilde{y}^*$. This places an easily calculable upper limit on coulombic efficiency.

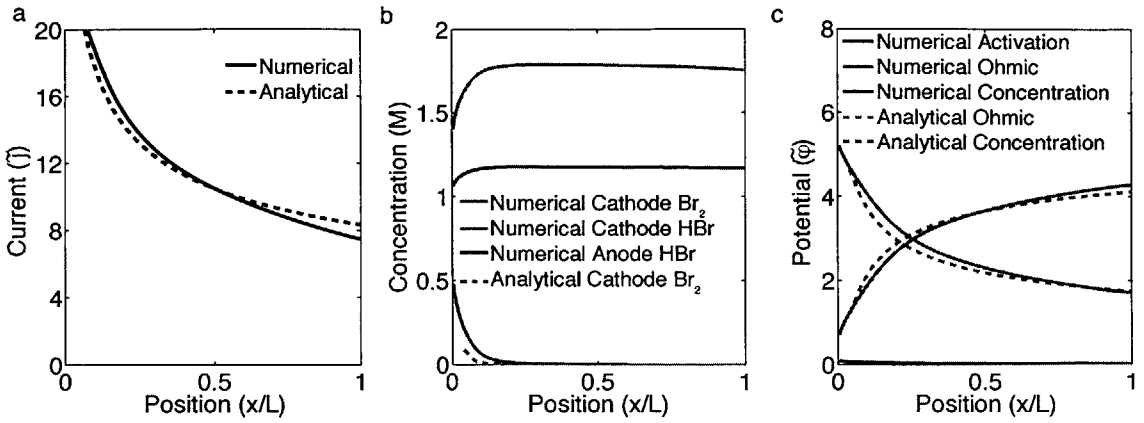

Figure 3-2: (a) Local dimensionless current density, (b) dimensionless concentrations of bromine and hydrobromic acid, and (c) dimensionless activation, ohmic, and concentration polarization losses along the length of the channel of the HBLFB for conditions listed in Table 3.1. Numerical results are shown as solid lines, with the analytical model overlaid as dashed lines. The dimensionless current density in the channel drops rapidly from a maximum at the inlet due to the sharply dropping bromine concentration at the cathode. Activation losses in the analytical model are negligible, and concentration polarization rises along the length of the channel to ensure constant electrode potential.

3.3.5 Under-limiting current

In any type of flow, the boundary-layer theory for limiting current can be extended to more completely describe an electrochemical flow cell by allowing for under-limiting current and finite electrolyte conductivity, which to our knowledge has not been done before. For the case of the HBLFB, activation losses are assumed to be small, an assumption justified by Figure 3-2, but the technique described here could easily be modified to account for activation losses. As long as the current density in the channel remains one-dimensional, the system can be described by a local current-voltage relation expressed in terms of dimensionless potential $\tilde{\varphi} = F\varphi/RT$ and conductivity $\tilde{\sigma} = RT\sigma/nD_iF^2c_i^0$. For the reacting bromine in the HBLFB, $n = 2$.

$$\tilde{\varphi}_{\text{cell}} = \tilde{\varphi}_{\text{c}}^0 = \frac{1}{2}\ln(\tilde{c}_{\text{Br2}}(\tilde{x})) - \tilde{j}(\tilde{x})/\tilde{\sigma} \tag{3.21}$$

If the conductivity becomes large, and the cell potential goes to a large negative value, Equation 3.21 returns the limiting current result from Equation 3.17 for Poiseuille flow. At finite cell potential and conductivity, the structure of the boundary layer is such that the local surface concentration changes slowly along the length of the channel relative to how it changes moving into the channel. At every point along the electrode, the local current density can be expressed in terms of the local cathode surface concentration and the limiting current density summarized in Table 3.2.

$$\tilde{j}(\tilde{x}) = (1 - \tilde{c}_{\mathrm{Br2}}(\tilde{x}))\tilde{j}_{\mathrm{lim}}(\tilde{x}) \tag{3.22}$$

Solving for $\tilde{c}_{\mathrm{Br2}}(\tilde{x})$ and substituting the result back into Equation 3.21 yields a current-voltage relation that can be implicitly solved for every point along the electrode.

$$\tilde{\varphi}_{\mathrm{cell}} = \tilde{\varphi}_{\mathrm{c}}^{0} + \frac{1}{2}\ln\left(1 - \frac{\tilde{j}(\tilde{x})}{\tilde{j}_{\mathrm{lim}}(\tilde{x})}\right) - \frac{\tilde{j}(\tilde{x})}{\tilde{\sigma}} \tag{3.23}$$

Equation 3.23 represents a general current-voltage relation for any laminar flow electrochemical cell with rapid ion removal at a surface. Since this relation is determined by ion transport to an adsorbing surface, the same fundamental result, using the appropriate ionic species in Equations 3.21 and 3.23, could also be applied to electrodialysis in Poiseuille flow [161], shock electrodialysis in plug flow [162] or any other membrane-based ion removal process in cross flow. The expression could be modified further to include anode concentration polarization or activation overpotential with no loss of generality. The impact of the flow profile on this expression is through the limiting current term, which can be specified to reflect the particular electrochemical cell being examined.

3.4 Results and Discussion

The HBLFB provides an example of a reversible membrane-less electrochemical cell with which to validate the theory presented in this work. In a recent article [146], it was shown that numerical solutions of the full two-dimensional model provide an excellent fit to experimental current-voltage data for different flow rates and bromine concentrations for both charging and discharging of the cell. Our focus here is on testing the accuracy of the simple analytical expressions derived above by boundary layer analysis and discussing general engineering principles for membrane-less laminar flow electrochemical cells.

Under the conditions specified in Table 3.1, the numerical solution can be used to predict the concentration of bromine and hydrobromic acid in the channel, as shown in Figure 3-3. Hydrobromic acid flows into the cell at a concentration of 1 M, and enrichment layers develop at both electrodes along the length of the channels. The enrichment is greater at the cathode than the anode due to the asymmetry in diffusion coefficients between the bromide ions generated at the cathode and the protons generated at the anode. A bromine depletion layer develops along the cathode where bromine is consumed, while a mixing region develops at the top of the bromine layer as bromine diffuses into the electrolyte. Eventually, these two regions begin to overlap, resulting in bulk depletion of the bromine. This is desirable from a reactant utilization perspective, since it means that a large fraction of the bromine is being consumed, but violates the analytical assumption that the bromine concentration is uniform far away from the cathode surface.

Another important result is that the current density drops rapidly along the length of the channel. Both the numerical and analytical models accurately predict this effect, as shown in Figure 3-3a. This behavior is in stark contrast to traditional membrane-based electrochemical systems where serpentine flow fields and other means are used to ensure that current density is approximately constant along the entire active area. This drop in current is due predominantly to the depletion of bromine at the cathode, as shown in Figure 3-3b. One implication of this behavior

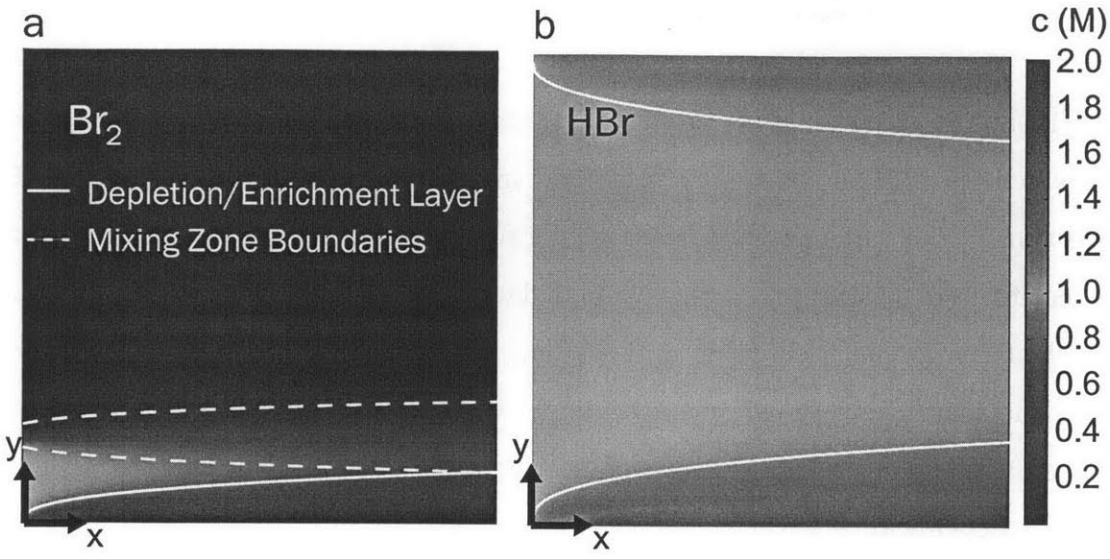

Figure 3-3: Concentration distribution of (a) bromine and (b) hydrobromic acid inside the channel under the conditions specified by Table 3.1. Depletion and enrichment layers derived from the boundary layer analysis are superimposed as solid white lines. Estimated reactant mixing zones that assume a linear velocity profile near the electrode wall are superimposed as dashed white lines.

is that the diffusion of acid away from the electrodes eventually becomes faster than the generation of acid at the electrodes. The result is a maximum acid concentration near the channel inlet followed by a gradual reduction in acid concentration along the rest of the channel.

High electronic conductivity within the current collectors ensures that the anode and cathode potentials are constant along the length of the channel, but the large variations in reactant surface concentrations and current density mean that the source of losses varies strongly. Losses can be grouped into three categories: activation, concentration, and ohmic. Activation overpotential is the potential required to drive charge transfer at the electrodes, concentration polarization describes the variation in equilibrium potential from standard conditions due to the enrichment or depletion of reactants and products at the electrodes, and ohmic loss is simply the potential drop across the electrolyte.

These three sources of loss can be compared to each other along the length of the channel. These results are shown in Figure 3-3c, and confirm that activation over-

potential is negligible as a result of the rapid reaction kinetics of both the bromine reduction reaction and the hydrogen oxidant reaction. This justifies ignoring activation losses in the analytical model. As expected, the strong spatial variation in species concentration and current density leads to variation in the source of loss along the length of the electrode, with ohmic losses dominating in the inlet region of the channel and concentration polarization rapidly building up towards the end of the channel. There is excellent agreement between the analytical and numerical predictions for ohmic and concentration losses along the length of the channel, which illustrates the predictive power of a lightweight analytical model to describe a numerically complex system.

The local current distribution predicted by the analytical and numerical models can also be integrated to calculate the average current density as a function of cell voltage. Because the analytical model treats only the dominant sources of loss- concentration polarization and ohmic losses- only four parameters are required to determine the analytical dimensionless current-voltage relation: aspect ratio, conductivity, Peclet number, and standard potential. For the purpose of this study, flow rate and reactant concentration are treated as model inputs. Figure 3-4a plots the predicted and observed current-voltage relation for the HBLFB during discharge as the Peclet number is varied from 5,000 to 15,000. The analytical model, which ignores activation overpotential completely, overestimates cell voltage at low current densities, but limiting current density is well described over a range of Peclet numbers.

The HBLFB employs reversible reactions at both electrodes, so both the analytical and numerical models can be easily applied to the cell during charging as well as discharging. Both the hydrogen oxidation reaction and the bromine reduction reaction are known to be reversible, so both models can equally be applied to the case of charging. If an external current is applied the cell, the electrodes switch function so that hydrogen is evolved at the cathode, and bromine at the anode. Figure 3-4b plots the analytical, numerical, and experimental current-voltage relations for the HBLFB during charging as the electrolyte concentration is varied. Again, the analytical theory slightly overpredicts performance at intermediate voltages compared

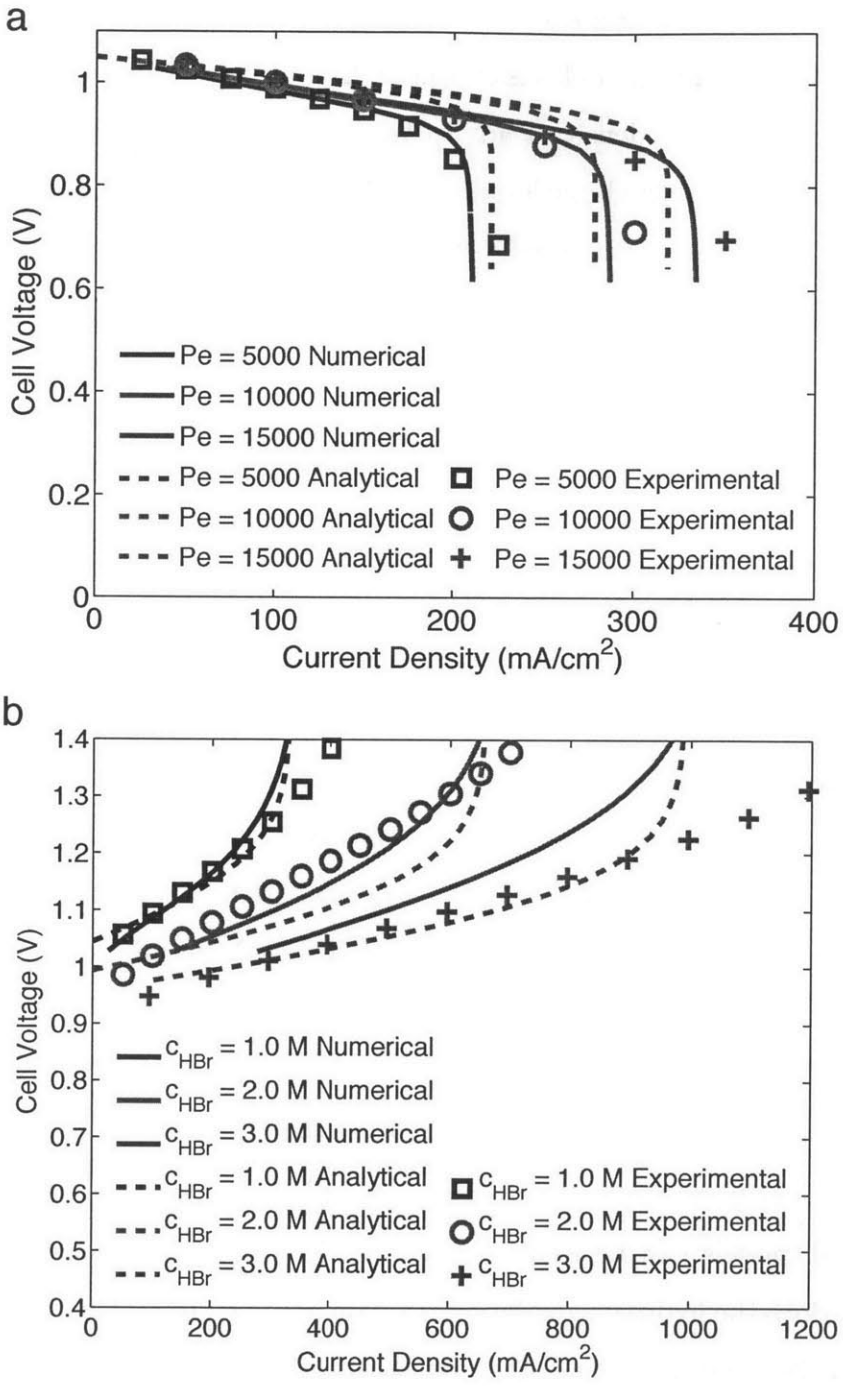

Figure 3-4: Numerical, (solid lines) analytical, (dashed lines) and experimental (symbols) current-voltage relations for the HBLFB at the conditions in Table 3.1 during (a) discharge as the Peclet number is varied from 5,000 to 15,000 and (b) charging as acid concentration is varied from 1 to 3 M. To ensure consistency with realistic operating conditions, no bromine was injected into the cell during charging.

to the numerical simulation. The disparity is likely due to the enrichment of bromine along the anode resulting in an increase in cell voltage in the numerical simulation that is not considered in the analytical theory. Experimental data displays slightly higher limiting current than predicted, which is most likely due to the presence of side reactions at high voltage. The formation of polybromides that occurs at high concentrations could also contribute to this behavior, and is not considered in either model [152].

This analysis can also be applied with no lack in generality to existing membrane-less electrochemical systems. For example, Da Mota et al. have recently demonstrated a membrane-less borohydride/cerium fuel cell that employs chaotic mixing to enhance its limiting current density [98]. When the chaotic element was removed, the authors observed limiting current densities of approximately 60 mA cm^{-2} and 140 mA cm^{-2} for flow rates of 0.5 mL min^{-1} and 3.0 mL min^{-1}, respectively. This result can be accurately predicted by employing literature values for the diffusion coefficient of borohydride in sodium hydroxide [163] and data about the channel geometry provided by the authors [98]. The expression for limiting current density provided in Table 3.2 estimates limiting current densities of 71 mA cm^{-2} and 129 mA cm^{-2}, respectively, validating the authors claim that the system was limited by borohydride diffusion.

3.5 Conclusion

This work develops general theoretical principles for the design and operation of membrane-less laminar flow electrochemical cells, and applies these techniques to the HBLFB as an example. Simple analytical results for different flow types, obtained by boundary layer analysis, provide a computationally inexpensive tool to rapidly examine the performance of laminar flow electrochemical cells in general by reducing the number of model parameters down to the minimum necessary to capture the dominant features of the system. Both the numerical and analytical models can be used to fit discharge and charging behavior and to identify the major sources of loss along the length of the channel. Predicted boundary layer profiles are also

essential to guide the splitting of the anolyte and catholyte fluid streams leaving the electrode gap. Properly designed systems can reduce mixing and maximize reactant utilization or electrolyzed products, which is of particular importance for rechargeable electrochemical cells such as the HBLFB. These models can be used to aid future design of membrane-less laminar flow electrochemical cells.

Similar models, augmented for bulk reactions, could also be applied to viscous flowable electrodes, as in semi-solid Lithium ion flow batteries [27, 164], flow supercapacitors [165], flow capacitive deionization [166], and electrochemical sensing [167]. These unconventional cell architectures rely on membrane separators between the flowable electrodes, but in principle, any combination of the three major components of the cell could be designed for laminar cross flow. Understanding the effects of advection-diffusion boundary layer scaling on electrochemical behavior is critical for the efficient and safe operation of such systems.

On a fundamental level, the results of this work are in sharp contrast to the common practice of treating electrochemical cells as quasi one-dimensional, in which case the sources of loss within the system can easily be classified by fitting to polarization curves. When symmetry is broken by cross flow, the local current density and concentration determine the spatial distribution of losses, which strongly vary along the surface of the electrode. Under conditions examined in this work, no single source of loss is dominant along the entire channel. The precise distribution of losses will vary depending on operating conditions and specific cell design, but the general result that the source of loss is highly variable along the length of the electrode is applicable to a wide range membrane-less laminar flow systems. The fact that electrochemical properties vary along the flow channel separating the electrodes, perpendicular to the current, also suggests that standard area-averaged figures of merit do not properly characterize the performance of flow batteries (regardless of whether or not there is a membrane). These metrics, such as the energy or power density per electrode area, should be replaced by other measures, such as coefficients in boundary layer approximations, which better capture the true, nonlinear scaling behavior of these systems.

Chapter 4

Inertial Effects on the Generation of Co-laminar Flows

4.1 Introduction

Combining multiple species together with laminar flow was an early application of microfludic technology, with applications ranging from flow cytometry [168] to micro reactors [59]. In these systems, moderate Reynolds numbers (Re $<$ 3000) inhibit turbulent flow, ensuring that fluids mix only due to molecular diffusion. Under these conditions, fully-developed flow is often assumed, allowing boundary layer analyses to describe some aspects of mixing [115, 116, 130, 137, 146]. In practice, the Reynolds number in many of these devices is of order unity or greater. As long as the flow is fully-developed and unidirectional, this is irrelevant since the velocity and the velocity gradient are orthogonal, eliminating inertial effects. However, when the flow bends, or if two channels converge into one, these effects no longer disappear, and must be taken into account.

The role of inertia in microfluidics has been previously examined in the context of flow in curved channels [169–173]. Asymptotic expansions have been calculated for very specific cases, including flow in a curved rectangular channel [173], but most efforts have been numerical or experimental [174]. There has also been some investigation of geometrically induced inertial recirculation created by sharp corners that

induce flow separation [175, 176], but questions remain about the role of inertia in common inlet geometries where multiple streams converge [177]. In this work, we examine the role of inertia around the inlet of two channels coming together under a range of conditions, taking existing experimental inlet designs used in membraneless electrochemical cells as a template [6, 79, 94, 146, 178]. These systems rely on reactant separation to successfully generate power. Fully developed flow ensures reactant separation, but the extent to which this assumption breaks down near the inlet is not well understood, and has not been considered in past investigations of membraneless electrochemical systems [178].

In this work, the Navier-Stokes equations are solved numerically for two- and three-dimensional geometries describing the flow of a fluid introduced into a main channel via an angled inlet. The geometry of this system mimics that of a membraneless laminar flow battery presented experimentally elsewhere [146]. Two major sources of mixing are identified: recirculation at the inlet due to flow separation at the inlet junction, and fluid mixing perpendicular to the flow direction due to three-dimensional wall effects as the flow curves. We find that under certain conditions, these two effects drastically increase mixing beyond what would be predicted in a fully developed system. A number of mitigation strategies are presented and discussed, and a scaling analysis is performed to better understand the underlying physics. To our knowledge, the scaling analysis herein is the first attempt to predict the onset of separation and secondary flows in microchannels at moderate Re.

4.2 Numerical Solution

Two and three-dimensional domains were modeled, as shown in Figure 4-1. The fluid flow was modeled using the Navier-Stokes equation, and mass transport was overlaid onto the results of that solution using dilute solution theory in a Newtonian fluid. The complete set of governing equations solve for the velocity field $\vec{v}$, pressure P, and

concentration c in terms of fluid density ρ, viscosity μ, and diffusion coefficient D.

$$\begin{aligned} \rho\left(\frac{\partial \vec{v}}{\partial t} + \vec{v}\cdot\nabla\vec{v}\right) &= \mu\nabla^2\vec{v} - \nabla P \\ \frac{\partial c}{\partial t} + \vec{v}\cdot\nabla c &= D\nabla^2 c \end{aligned} \tag{4.1}$$

Steady state was assumed in all cases, so the time dependent partial derivative drops out of the equations. No slip and no flux were assumed along the walls of the channel. In the three-dimensional model, only half the width of the channel was modeled, with a symmetry boundary condition imposed at the centerline.

The system was numerically implemented in COMSOL Multiphysics (Burlington, MA). The flow remains laminar because the Reynolds numbers investigated were sufficiently low. Numerical parameters were chosen to match previous experimental data, and unless otherwise specified are listed in table 4.1. To be consistent with past experimental work, the flow ratio n between the inlet to the main channel and the inlet to the secondary channel was maintained at 10:1, with a dimensionless concentration of one maintained at the beginning of the secondary channel. The flow rates were set to ensure that once the channels converged, the average flow velocity U_{main} resulted in the specified Reynolds number, specified in terms of the fluid density ρ, fluid viscosity μ, and channel height h.

$$\text{Re} = \frac{\rho U_{\text{main}} h}{\mu} \tag{4.2}$$

4.3 Results and Discussion

4.3.1 Comparison with fully developed flow

A useful way of looking at the results from the numerical model is to compare them with results from fully developed flow. In this case species transport is modeled by assuming unidirectional Poiseuille flow in the channel with perfectly divided reactant starting at $x = 0$ in the channel, as might be ideally assumed for the geometry

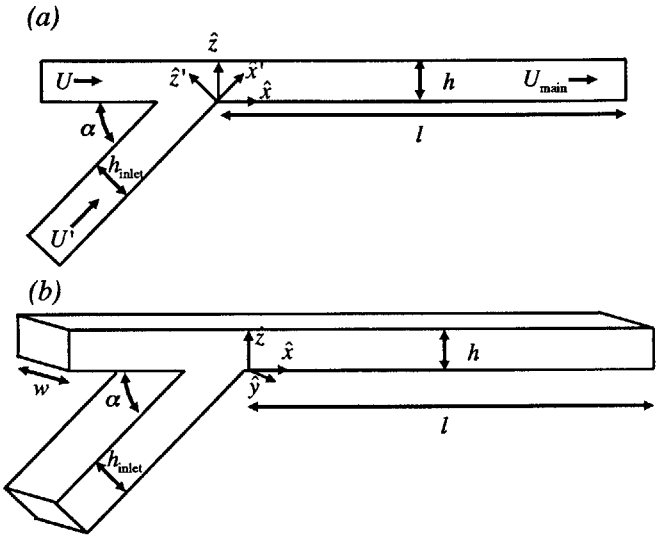

Figure 4-1: Flow cell geometry in the two-dimensional (a) and three-dimensional (b) domain.

Table 4.1: Parameters employed in the numerical calculation unless otherwise specified.

Parameter/units	Symbol	Value
Channel width/mm	w	1.8
Channel length/cm	l	1.3
Channel height/μm	h	1000
Inlet height/μm	h_{inlet}	800
Fluid density/kg m^{-3}	ρ	10^3
Fluid viscosity/Pa s	μ	10^{-3}
Diffusion coefficient/cm^2 s^{-1}	D	10^{-5}
Reactant flow ratio	n	10
Reynolds number	Re	10

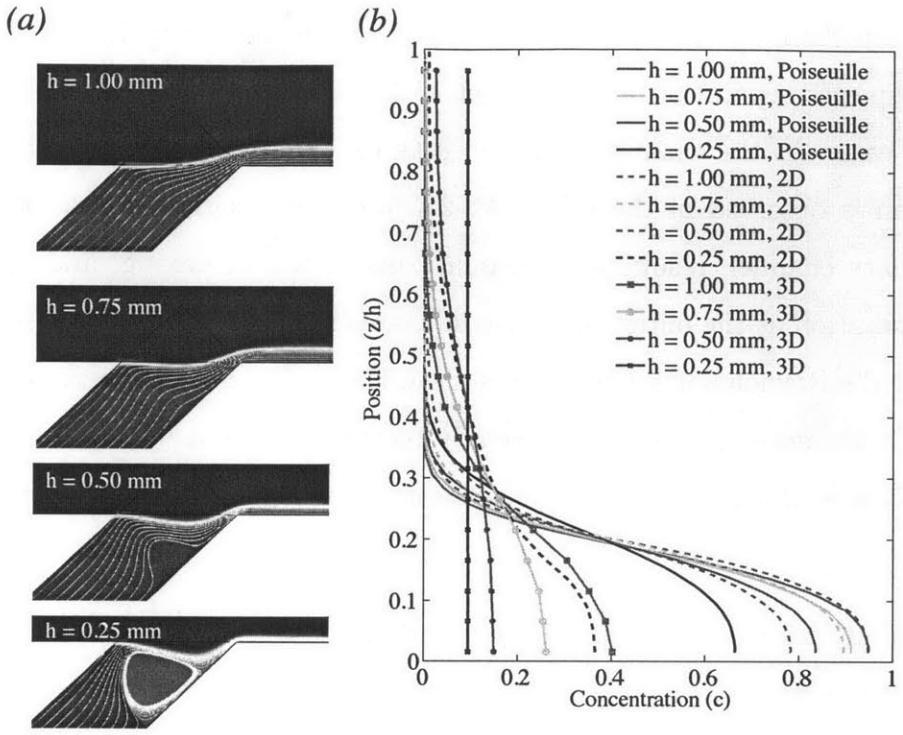

Figure 4-2: (a) Species concentration distribution and fluid stream lines for two-dimensional flow near the inlet as a function of channel height for a Reynolds number of 10. All other parameters are specified in table 4.1. For sufficiently thin channels, flow separation and recirculation can be observed. (b) Species concentration at the main channel outlet centerline as a function of channel height for fully developed Poiseuille flow, a two-dimensional inlet, and a three-dimensional inlet geometry with other parameters as specified in table 4.1. In the absence of flow recirculation, the two-dimensional model produces results similar to those predicted by ideal Poiseuille flow, but recirculation significantly enhances mixing. The three-dimensional channel produces significantly more mixing, with significant mass reaching the far wall for channels as tall as 500 μm.

shown in Figure 4-1. Under these idealized conditions, diffusion of reactant across the channel is sufficiently slow that almost none of it reaches the opposite side of the channel, as shown in Figure 4-2. This condition is necessary for a number of applications, and would indicate that if the fully developed flow assumption is valid, channel heights as small as 250 μm are feasible.

Two-dimensional numerical calculations were performed for a range of channel heights, from 1 mm down to 250 μm, as shown in Figure 4-2. For channel heights greater than 500 μm, the fluid from the secondary channel appears to flow smoothly

into the main channel, with minimal disturbance in the flow near the inlet, resulting in strong species separation at the outlet of the channel consistent with the fully developed case. As the channel height shrinks to 500 μm, however, significant flow deformation is observed in the inlet. At 250 μm, flow recirculation is observed in the secondary channel, resulting in dramatically increased mixing, and diminished species separation at the outlet of the main channel. This recirculation behavior is a function of the Reynolds number in the system indicating that it is inertial in nature, as shown in Figure 4-3. This type of steady recirculation behavior is also commonly observed in flow along curved surfaces when the Reynolds number is between 4 and 40 [179].

Greater understanding of the physics leading to recirculation can be gained by considering the motion of fluid through the secondary channel towards the main channel. As the fluid nears the intersection, it accelerates to match the velocity of the fluid in the main channel. Based on the size of the recirculation region in Figure 4-2a, it is reasonable to assume that the change in fluid velocity occurs over a length roughly equal to h, the height of the main channel as shown in Figure 4-1. We postulate that when the inertial term in the governing equation for the secondary channel flow is greater than the viscous term, the inertial behavior in the secondary channel becomes sufficient to distort the fluid upwards away from the bottom of the channel, which drives recirculation and causes mixing to occur. This parameter amounts to an effective Reynolds number for the inlet region that is distinct from the Reynolds number for fluid flow in the main channel defined in Equation 4.2. The characteristic velocities U' in the secondary channel and U in the main channel can be expressed in terms of the main channel Reynolds number and the parameters listed in table 4.1.

$$\begin{aligned} U &= \frac{n}{1+n}\frac{\mu \mathrm{Re}}{\rho h} \\ U' &= \frac{1}{1+n}\frac{\mu \mathrm{Re}}{\rho h_{\mathrm{inlet}}} \end{aligned} \tag{4.3}$$

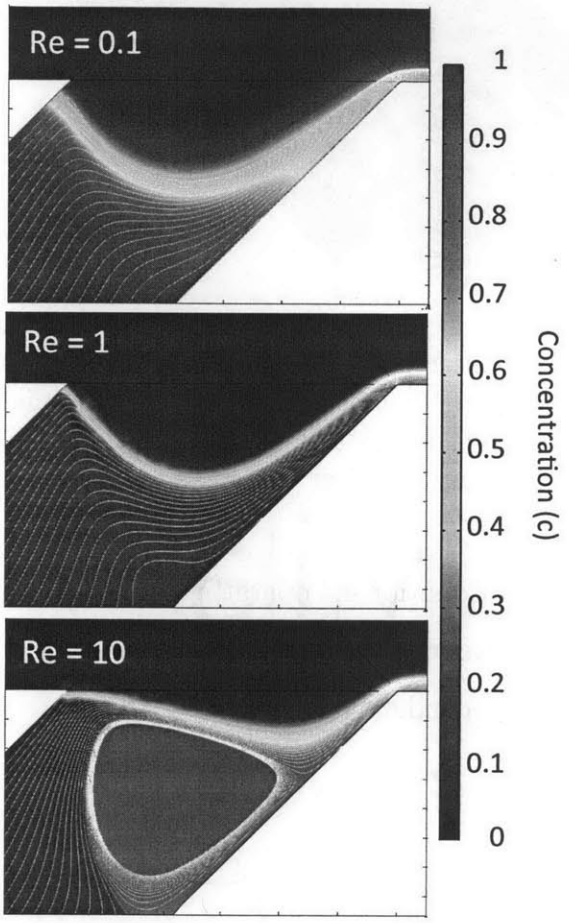

Figure 4-3: Species concentration near the inlet of the two-dimensional channel with a height of 250 μm as a function of Reynolds number. Under the conditions specified in table 4.1, Reynolds numbers of 0.1, 1, and 10 correspond to effective inlet Reynolds numbers of 0.3, 3, and 30, respectively. As the Reynolds number increases, the velocity gradient near where the secondary channel meets the main channel is enhanced, resulting in flow deformation and recirculation.

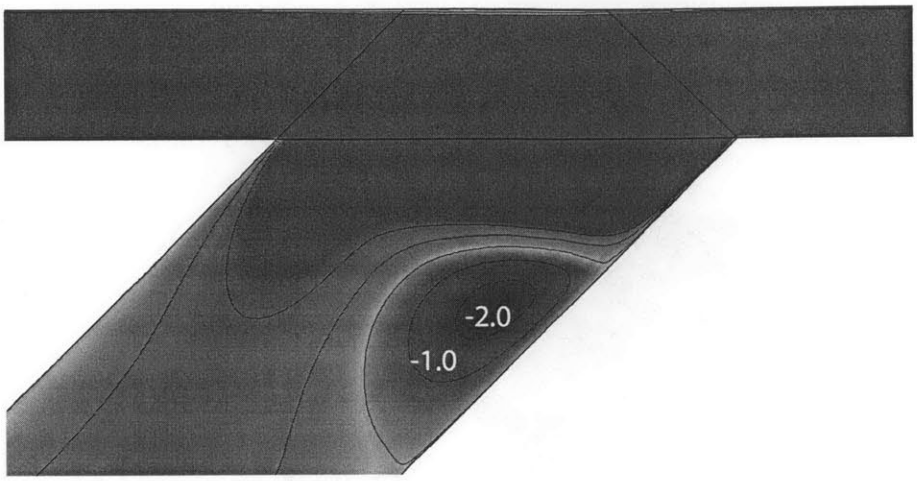

Figure 4-4: Dimensionless recirculation velocity in the x' direction in the inlet channel scaled by the characteristic secondary channel velocity U' for a main channel height of 100 μm, a secondary channel height of 250 μm, and a Reynolds number of 20. All other parameters are as described in table 4.1. Significant recirculation is observed, with a maximum negative dimensionless velocity in excess of -2.

A simple scaling analysis of Equation 4.1 operating in the x direction can be performed to derive the effective inlet Reynolds number $\mathrm{Re}_{\mathrm{inlet}}$ in terms of the parameters listed in table 4.1, including the secondary channel angle α.

$$\begin{aligned} \mathrm{Re}_{\mathrm{inlet}} &= \frac{\rho\left(U - U'\cos\alpha\right)h}{\mu} \\ &= \left(\frac{n}{n+1} - \frac{h}{h_{\mathrm{inlet}}}\frac{\cos\alpha}{n+1}\right)\mathrm{Re} \end{aligned} \tag{4.4}$$

It is also constructive to examine the magnitude of the recirculating velocity by considering the greatest negative velocity in the stagnation region in the $-x'$ direction scaled to the characteristic velocity scale in the secondary channel, U'.

$$\tilde{u}' = \left|\min\left(\frac{u'}{U'}\right)\right| \tag{4.5}$$

This quantity provides a measure of the extent to which recirculation is significant within the channel, and is illustrated in Figure 4-4 for a demonstrative case.

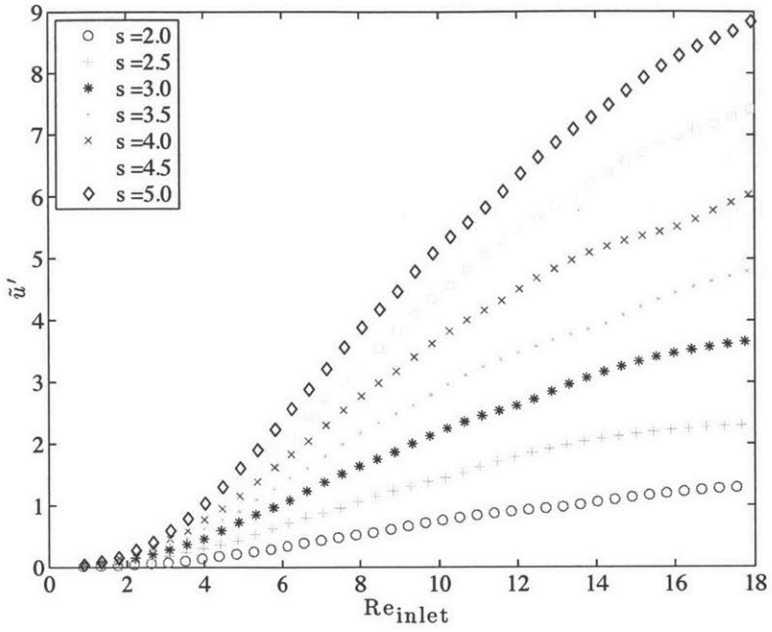

Figure 4-5: Maximum dimensionless recirculation velocity $\tilde{u}'$ as a function of inlet Reynolds number $\mathrm{Re}_{\mathrm{inlet}}$ as defined in equation 4.4 for a range in secondary channel heights. The main channel height is kept fixed at 100 μm, and the flow ratio is maintained at $n = 10$.

The inlet Reynolds number $\mathrm{Re}_{\mathrm{inlet}}$ and the maximum dimensionless recirculation velocity $\tilde{u}'$ can then be tabulated over a wide range of conditions by varying the main channel Reynolds number and the secondary channel height. Figure 4-5 plots recirculation velocity as a function of inlet Reynolds number for a range of range of inlet heights and Reynolds numbers. This plot demonstrates that the value of $\mathrm{Re}_{\mathrm{inlet}}$ at which recirculation becomes important, such that $\tilde{u}' > 1$, is a strong function of the relative heights of the channels, defined as $s = h_{\mathrm{inlet}}/h$.

This result can be collapsed further by considering the relationship between the recirculation velocity $\tilde{u}'$ and the relative heights of the secondary and main channels, $s = h_{\mathrm{inlet}}/h$. As s gets larger, the velocity in the primary channel becomes larger relative to that of the secondary channel. From equation 4.3, the relationship between the flow ratio, the channels' velocity scales, and the channels' heights can easily be expressed.

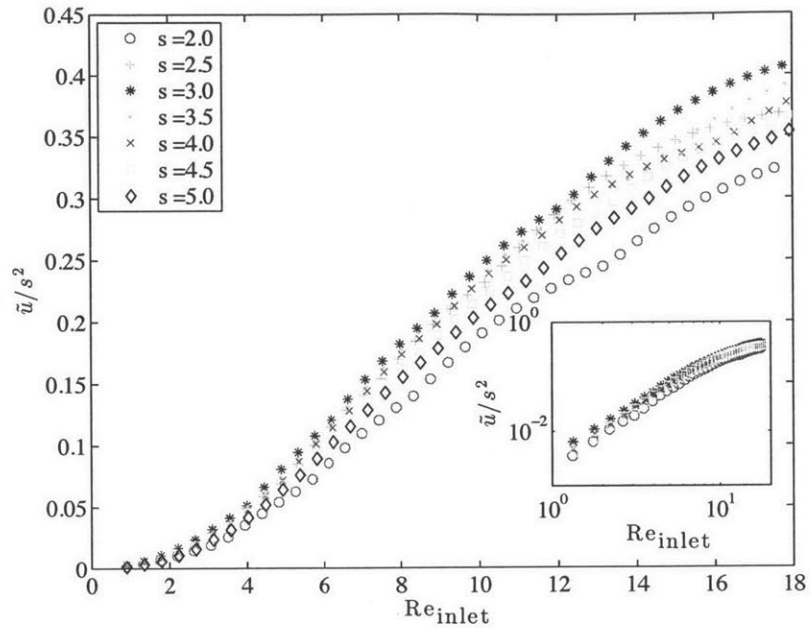

Figure 4-6: Maximum dimensionless recirculation velocity $\tilde{u}'$ scaled by the ratio of secondary to main channel height s^2 as a function of inlet Reynolds number $\mathrm{Re}_{\mathrm{inlet}}$ as defined in equation 4.4 for all the data shown in Figure 4-5. The inset plots the same data on a log-log scale.

$$\frac{U}{U'} = ns \tag{4.6}$$

The fluid velocity in the main channel is the dominant source of fluid motion, which drives the recirculation. Since the recirculation effect is a result of the inertia in the primary channel, we expect that the recirculation velocity scaled to the primary channel velocity will increase as the primary channel velocity increases. From equation 4.6, $U \sim s$, so we consider the maximum recirculation velocity scaled to s^2 as a good measure of recirculation. This expectation is validated by Figure 4-6, which illustrates that the results from all 266 numerical simulations shown in Figure 4-5 collapse onto a single line.

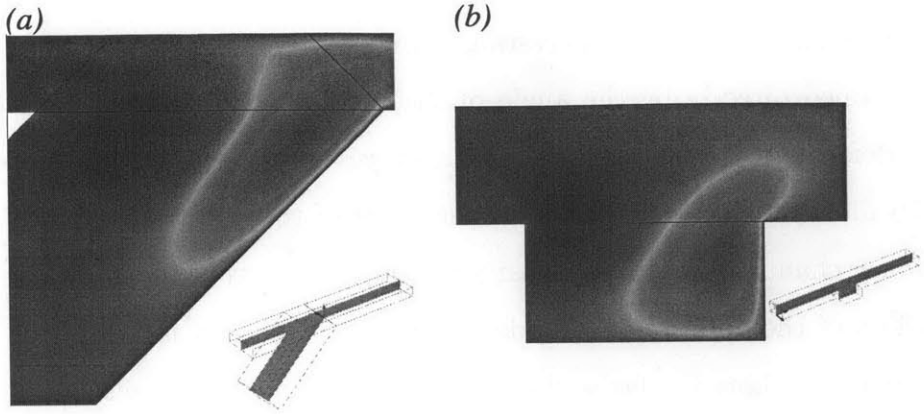

Figure 4-7: (a) Out of plane fluid flow velocity (surface) one quarter of the channel width away from the wall near the inlet of the three-dimensional channel with a height of 500 μm and a Reynolds number of 10. A schematic of the cut plane is shown as an inset. As the fluid in the main channel bends downwards towards the secondary channel, the fluid is deflected towards the center of the channel, represented by the blue region. Likewise, the upwards curvature of the fluid as it bends back into the main channel results fluid being being driven towards the wall represented by the red region. (b) A similar effect can be observed for a simple rectangular channel with a square pocket added. The average fluid velocity and curvature are similar, so the out of plane behavior is also very similar.

4.3.2 Three-dimensional effects

Although flow separation and recirculation play a key role in mixing, they are not the only source of non-idealities in the channel. It is customary to neglect edge effects for wide rectangular channels far from the walls, but those walls can play a very significant role when the flow bends at low or moderate Reynolds number, as observed in the case of Dean flow in a pipe or a rectangular channel [169, 171, 174]. Even at low Reynolds number, the walls can induce significant secondary flows around sharp corners or bends with a non constant radius of curvature [174,180,181]. The recirculating eddies formed in such geometries have been shown to induce the formation of biofilm streamers when certain strains of bacteria are introduced [182]. Similar phenomena can be observed in contracting or expanding flows, which also have been shown to induce out of plane flow [180, 183].

In the case of the inlet geometry considered here, velocity gradients between the centerline of the channel and the wall drives flow out of plane, further enhancing

mixing as shown in Figure 4-7. Interestingly, the effective curvature of the fluid flow is not determined directly by the angle of the inlet, or the height of the channels, but by the deformation of the fluid flow as it curves upwards into the main channel. Figure 4-7b illustrates that the upwards curvature of the fluid, even in the absence of a secondary channel contributes most strongly to the out of plane flow velocities. The net effect of the additional secondary flows is to enhance mixing further, with significant mass reaching the far wall of the channel even for channels as tall has 500 μm, as shown in Figure 4-2. This result is consistent with experimental data from the Hydrogen Bromine Laminar Flow Battery, which indicates significant performance degradation when the channel height drops below 600 μm, as shown in Figure 4-8. This channel height corresponds to an effective inlet Reynolds number of $\mathrm{Re}_{\mathrm{inlet}} = 14$. As the channel height is decreased further, the effective inlet Reynolds number will increase, suggesting that this value represents an upper bound on the effective inlet Reynolds number to suppress recirculation.

4.3.3 Mitigation strategies

The combination of two and three-dimensional secondary flows conspire to establish a minimum channel height of roughly 750 μm for the geometry examined in this study. Making the channel thinner while maintaining species separation is important to a number of applications, so a number of potential strategies were pursued to enhance species separation. These strategies fell into four groups: varying the channel width to minimize wall effects, varying the secondary channel height to reduce the velocity gradient between the secondary and primary fluid flows, varying the secondary channel angle to maximize the unidirectional nature of the flow, and rounding off the edges near the convergence of the two channels to minimize flow separation.

As shown in Figure 4-9, making the channel narrower suppresses the out of plane flow that had previously enhanced mixing, resulting in improved species separation. Since more of the channel is close to the wall, however, wall effects become significant, resulting in out of plan concentration gradients along the top of the channel. This behavior could have a detrimental impact on certain types of systems, but could

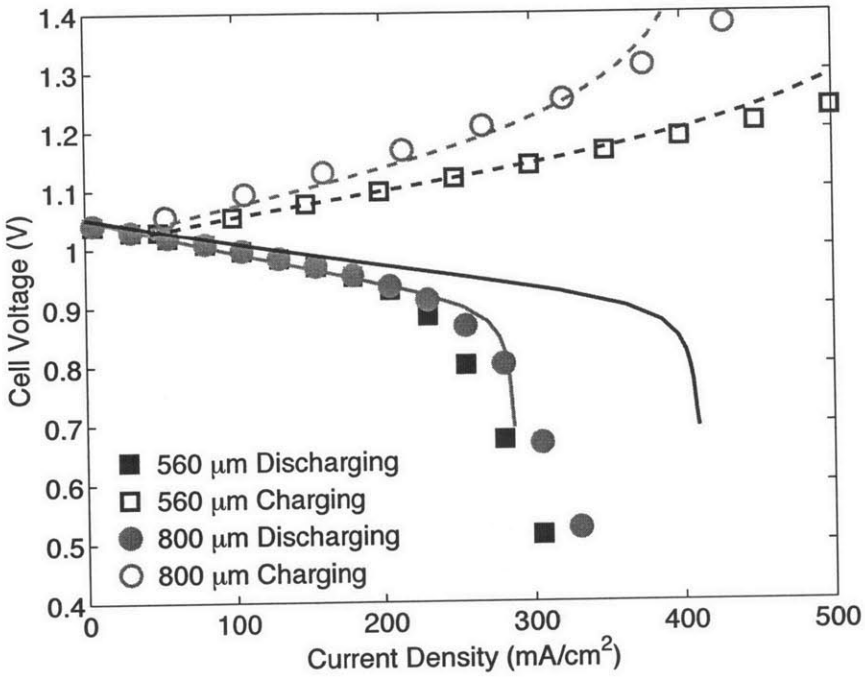

Figure 4-8: Current-voltage performance of the HBLFB with bromine concentration of 1.0 M, hydrobromic acid concentration 1.0 M, and a cell Reynolds number of 10. Further experimental details are available in Chapter 2. When the cell was run using a channel height of 800 μm (green circles), both discharging (solid points) and charging (open points) experimental data was in agreement with numerical modeling results (solid and dashed lines). When the experiment was repeated with a channel height of 560 μm (blue squares), the charging experimental and modeling results showed good agreement, but discharging experimental and modeling results do not.

provide an incremental benefit depending on the application.

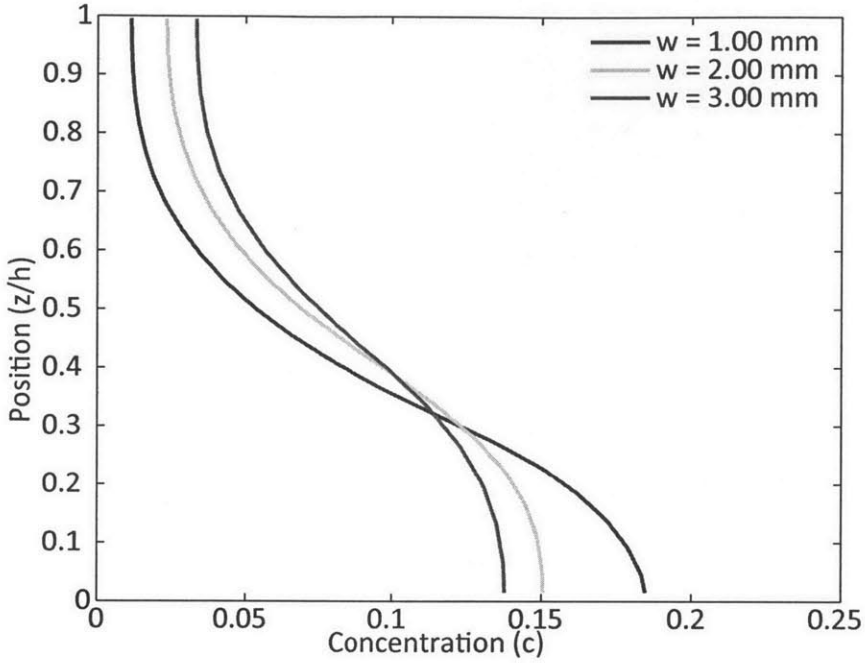

Figure 4-9: Species concentration near the inlet of the two-dimensional channel with a height of 500 μm as a function of channel width with other system parameters as specified in Table 4.1. As the channel width decreases, wall effects inhibit recirculation, resulting in slightly reduced concentration at the outlet vertical centerline.

Reducing the secondary channel height has the effect of increasing the fluid velocity to minimize the velocity gradient near the inlet. This strategy does suppress recirculation, but the increased velocity of the fluid results in sufficient momentum in the z direction that the fluid initially impinges into the channel farther than it would in the fully developed condition, resulting in enhanced mixing. Almost no effect is observed on the outlet concentration, as shown in Figure 4-10.

Varying the inlet angle appears again to trade off one benefit for another: shallower channels appear to minimize the inertial impingement of the fluid into the channel, but also enhance recirculation due to a larger interaction region between the two converging streams. The net result is that shallow angles appear to improve species separation near the channel wall, but degrade separation near the centerline of the channel. This effect is shown in Figure 4-11. The net result is minimal benefit by

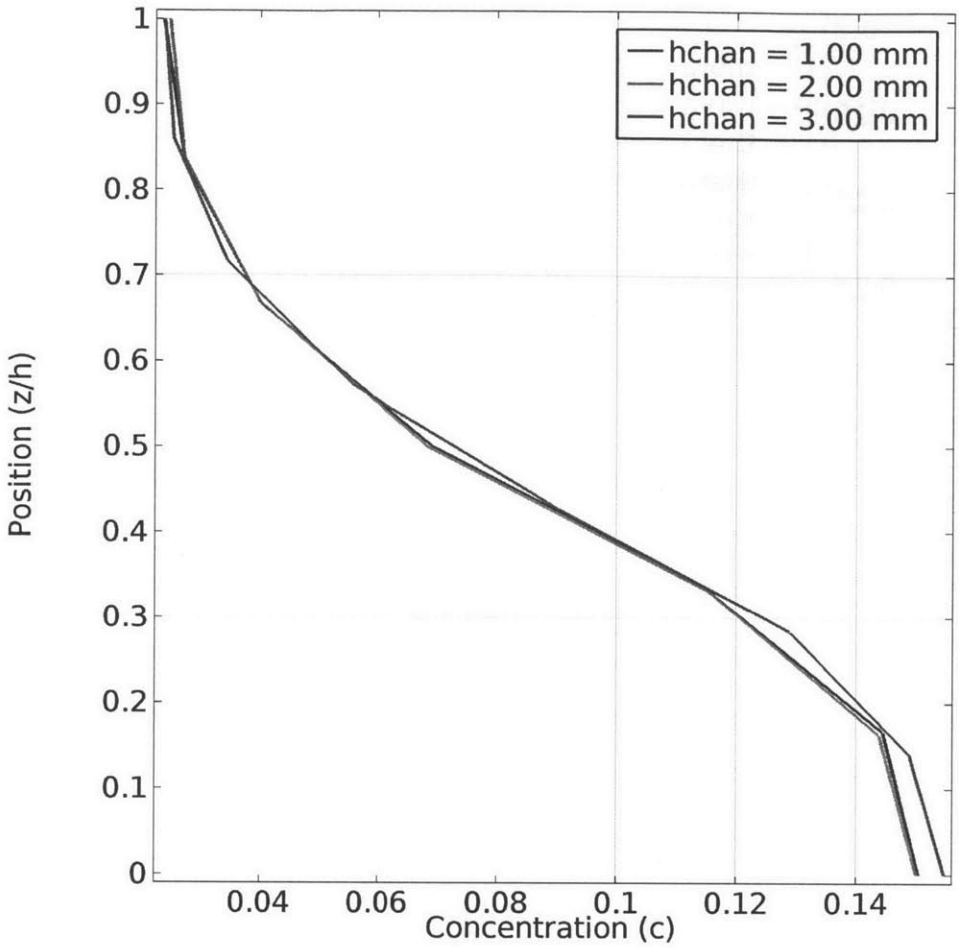

Figure 4-10: Species concentration along the centerline of the outlet of a three-dimensional channel with a height of 500 μm and other parameters as specified in Table 4.1. Inlet height appears to have minimal effect on the outlet concentration.

varying the inlet angle.

A final mitigation strategy investigated was to apply a finite radius of curvature to the converging channels. This was done to minimize singularities in pressure gradient that have been shown to induce recirculation regardless of Reynolds number [184]. A range of radii of curvatures successfully inhibited recirculation at the inlet. However, there was still significant deflection of the fluids, and the outlet concentration of the systems indicate minimal benefit.

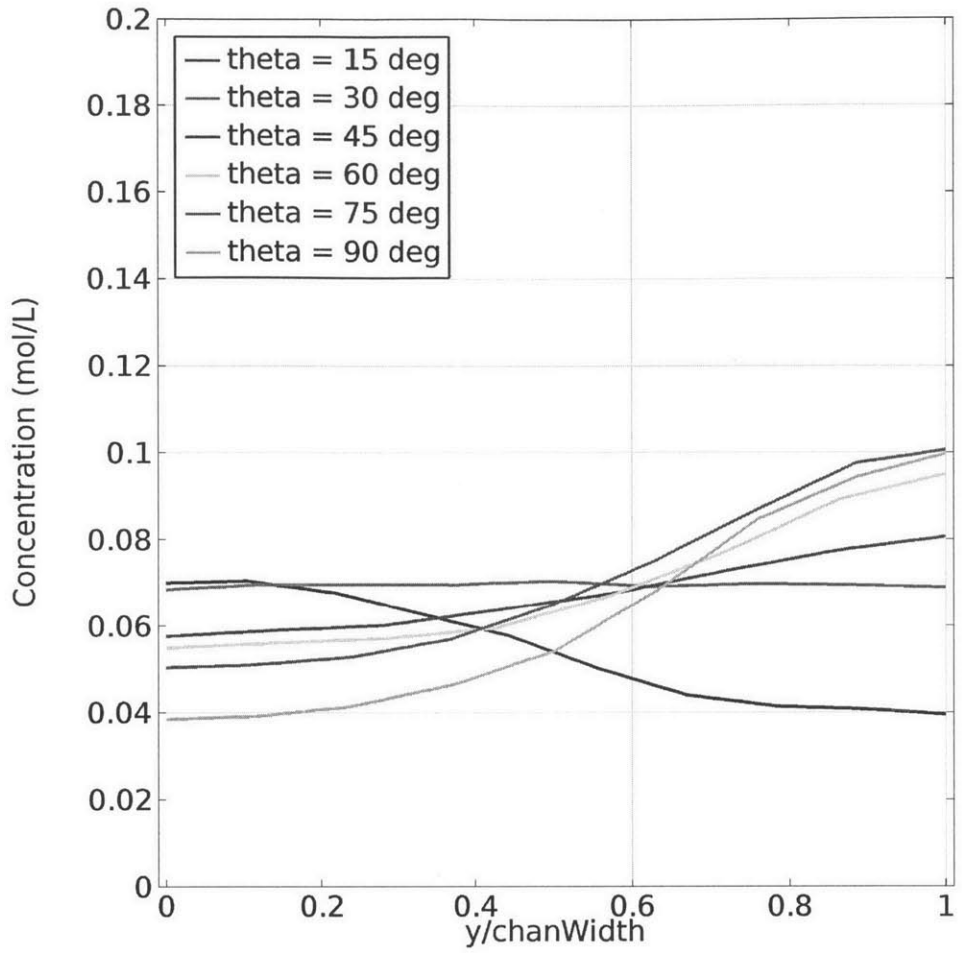

Figure 4-11: Species concentration out of plane along the top edge of the outlet of a three-dimensional channel with a height of 500 μm and other parameters as specified in Table 4.1. Steeper inlet angles appear to improve separation near the centerline of the channel, but degrade separation near the wall.

4.4 Conclusion

This result captures the dominant design criteria describing the convergence of two co-laminar liquid streams at moderate Reynolds number in rectangular channels. We find that for any operating condition, the recirculation velocity can be written as a function of the channel aspect ratio and the inlet Reynolds number, $\tilde{u}'/s^2 = F(\mathrm{Re}_{\mathrm{inlet}})$. This insight can be used as a guide for future channel designs, and informs the intuition that the velocity gradient of the fluid as it passes from the secondary channel into the main channel drives recirculation. A complete understanding of the source of the recirculation behavior is beyond the scope of this work, and remains a promising

avenue of research.

In addition to the recirculation effect, we have also identified and numerically observed wall-induced eddy currents that produce out of plane fluid flow that enhance mixing and disrupt the assumption of two-dimensional flow, even for relatively wide channels. These two effects conspire to establish a maximum effective inlet Reynolds number to maintain the validity of the fully developed flow assumption, and to ensure the species separation necessary for a wide range of applications, including systems incorporating chemical and electrochemical reactions.

Chapter 5

Guidelines for Stationary Energy Storage Technology Development

5.1 Introduction

Increasing the economic viability of renewable energy sources such as photovoltaic panels and wind turbines has been widely recognized as a critical goal for the long term stability and security of the electrical grid [185]. Developments in the production of photovoltaic panels and wind turbines have contributed to dropping costs of generation, but significant work remains to meet economic performance targets [186]. Large-scale energy storage has been proposed to provide grid-scale services such as frequency regulation, transmission and distribution upgrade deferral, and energy arbitrage [187–192], and has also been discussed as a means to provide baseline power in conjunction with renewable sources [190, 193–196], and to increase the economic viability of existing renewable generation resources [185, 197–200]. Such an approach could widen the potential market for renewable generation technologies, increasing production rates and reducing costs.

Compared to energy generation technologies, storage technologies are unique in that their levelized unit energy cost is highly dependent on the configuration of the installed system, with each system rated not only for a peak power, but also for a particular energy storage capacity. However, the cost per energy ($\$\ \mathrm{kWh}^{-1}$) and the cost

per power ($\$\,kW^{-1}$) for various energy storage technologies vary widely, complicating direct comparisons between energy storage technologies. Past work has focused on the strengths and weakness of particular energy storage systems [118, 120, 201]. In this chapter, the economic viability of a hybrid renewable generation/storage plant is investigated as the power and energy rating of its storage subsystem is varied. This analysis establishes performance targets for the economic viability of a hybrid plant as a function of geography and generation technology. A technology-level analysis is also conducted by considering only optimally sized storage systems as a function of power and energy related costs. In this way, performance tradeoffs between technologies can be examined in a system-independent manner. Although the real-time pricing markets in which the systems are situated play a critical role, this analysis shows that the tradeoffs between storage system costs are consistent across a range of markets and generation technologies, suggesting a result that is robust to the specifics of any given installation. This analysis provides a quantitative framework with which one can evaluate existing technologies, as well as guide future development of energy storage technologies to better suit renewable integration applications.

5.2 Experimental

5.2.1 Introduction

The analysis in this chapter is performed in four steps. First, three sites were selected across the United States, and real-time pricing data and renewable generation data were compiled for each one. Second, the economic performance of a range of hypothetical hybrid renewable plants that incorporate a renewable generation resource and a storage subsystem was considered by optimizing the time-resolved charge and discharge behavior of the system. Third, a dimensionless performance parameter comparing revenue to cost was established and calculated to provide a universal figure of merit with which to compare the systems with storage configuration, cost, and efficiency as model inputs. Fourth, a secondary optimization was performed to deter-

mine the optimal storage system size as a function of the energy- and power-related cost of storage, which allowed storage technologies with different cost metrics to be directly compared for each location and generation technology.

5.2.2 Site selection

Since the economic performance of the proposed system is highly dependent on the geographic location where it would be operated, three demonstrative geographic sites were chosen: McCamey, TX; Palm Springs, CA; and Plymouth, MA. The Texas site was chosen as an example of a high performing wind site, with an average capacity factor of 32% over the period examined. The California site was chosen as a high performing solar site, with an average capacity factor of 23%. The Massachusetts site was chosen as a baseline case, where neither wind nor solar was particularly high performing, with capacity factors of 26% and 16%, respectively. Figure 5-1 illustrates the distribution of generation and pricing for these three sites. Data for zonal real-time pricing was obtained from the ISO New England [202], Energy Reliability Council of Texas [203], and California ISO [204] websites. To simulate the performance of a hypothetical wind turbine or solar array, local windspeed and solar insolation data was obtained from the Eastern and Western National Wind Integration Datasets and the National Solar Radiation Database, and then transformed to time dependent output per MW installed using published performance data for a Vestas 3 MW wind turbine [205] and for a standard commercial solar array [206]. Pure arbitrage storage systems that did not incorporate any generation resource were also considered.

5.2.3 Optimization routine

Three key performance parameters were identified as intrinsic to any storage technology: power-related cost per kilowatt, energy-related cost per kilowatt-hour, and roundtrip efficiency. Although incremental improvements on these assumptions could be made for specific technologies, (for example, a flow battery model might consider ramp rate limitations or variation in efficiency as a function of state of charge,)

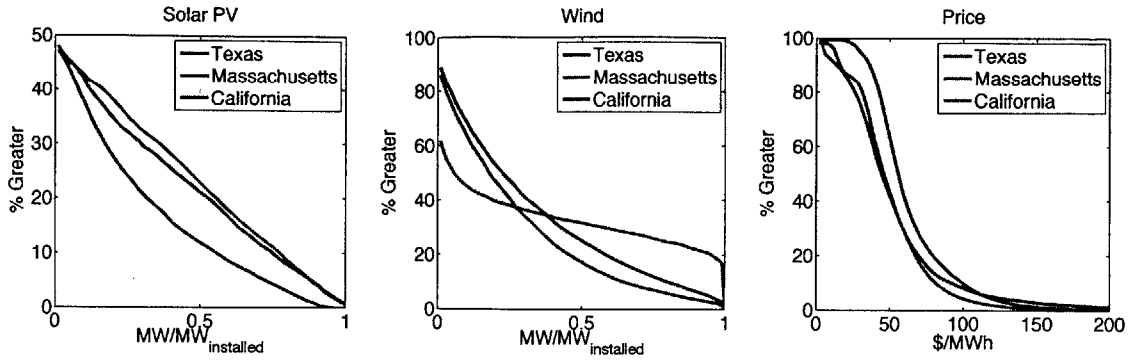

Figure 5-1: Cumulation distribution of specific solar output (left), wind output (center), and price per MWh (right) of generation in McCamey, TX, Plymouth, MA, and Palm Springs, CA.

focusing on only three key parameters adequately simulates the performance of a wide range of storage systems, allowing for direct comparison between all existing technologies, as well as any potential future ones. Lastly, cost parameters are considered independently for the energy and power-related parts of a particular system. Although the total cost intensity per kilowatt or per kilowatt-hour of a particular system is more frequently quoted than the specific energy or power related cost intensity, separating out the costs in this manner makes them system-independent, and more accurately reflects the inherent properties of the technology rather than the choices of the system designer [13].

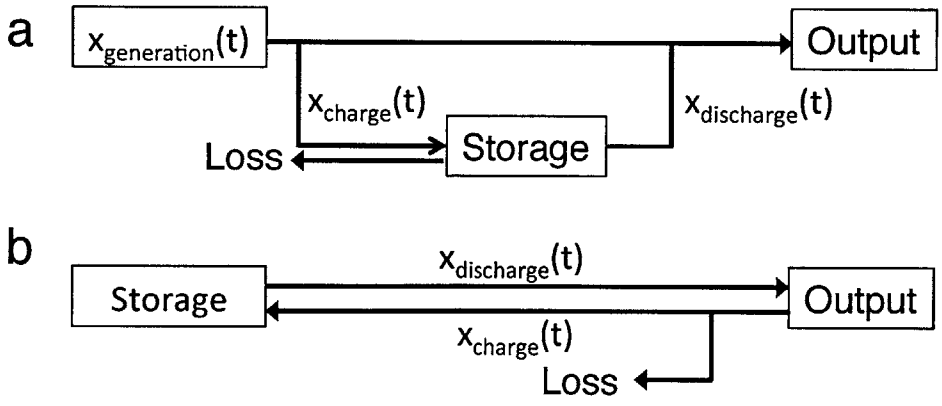

Figure 5-2: Schematic for modeling for hybrid (a) and arbitrage (b) energy storage system.

For each location and plant configuration, an optimization procedure was per-

formed using hourly pricing and generation data from January through December of 2004 to determine the maximum revenue that a hypothetical plant could generate per MW of generation. A trajectory-type approach was employed, in which the decision to charge or discharge the storage system at each time step is taken in order to maximize the revenue of the system subject to system power and energy constraints. The optimization was performed in three week intervals, with one week overlap between each interval to ensure that there were no artificial discontinuities in the results. For the case of the hybrid systems, it was assumed that the charge rate was capped at the real-time output of the generation resource, such that electricity was never purchased back from the grid, whereas the pure arbitrage system could always charge up to its maximum power rating. For the purpose of the simulation, energy stored was defined as energy available to discharge into the grid, so all inefficiencies were incorporated into the charging process. A schematic of the modeled system is shown in Figure 5-2. In order to reduce the computational expense of the optimization, the storage trajectory considered charging and discharging separately so that a linear solution technique could be employed. The optimization routine for each three week segment ($N = 504$ hours) can then be expressed in terms of the real-time price $P(t)$ (\$ MWh^{-1}), the generation profile $x_{\mathrm{generation}}(t)$ (MW $\mathrm{MW}^{-1}_{\mathrm{generation}}$), storage roundtrip efficiency η (%), peak power $\dot{E}_{\mathrm{max}}$ (MW $\mathrm{MW}^{-1}_{\mathrm{generation}}$), and hours of capacity at peak power E_{max} (hrs).

$$\max\left(R_{\mathrm{total}} = \sum_{i=0}^{N} P(i)(x_{\mathrm{generation}}(i) + x_{\mathrm{discharge}}(i) - x_{\mathrm{charge}}(i)/\eta)\right) \quad (5.1)$$

$$0 \leq x_{\mathrm{discharge}} \leq \dot{E}_{\mathrm{max}} \quad (5.2)$$

$$0 \leq x_{\mathrm{charge}} \leq \min(\eta x_{\mathrm{generation}}(t), \eta \dot{E}_{\mathrm{max}}) \quad (5.3)$$

$$0 \leq \sum_{i=0}^{j} \left(x_{\mathrm{charge}}(i) - x_{\mathrm{discharge}}(i)\right) \leq E_{\mathrm{max}} \dot{E}_{\mathrm{max}} \quad (5.4)$$

An offset is included in the energy constraint for each optimization period to account for the amount of energy stored in the system at the beginning of the op-

timization period. An optimized 'trajectory' for the storage system will shift the output of the system to periods of high market pricing, subject to the constraint that a fraction of all stored energy is lost to inefficiency. It must be acknowledged that the majority of existing renewable generation resources sell their energy on purchase price agreements or other fixed-price long term contracts, rather than onto the real-time pricing market, which would limit the value of storage. However, these fixed-price contracts are untenable in the long term, so it will eventually be necessary for renewable generation resources to compete directly on the real-time market with traditional variable generation resources such as gas turbines. This analysis aims to describe such a situation.

To simplify the analysis, it was assumed that the storage systems operate only on the real-time energy markets, and that they are small enough that they do not greatly impact the real-time pricing markets in which they operate. This analysis is consistent with prior work, and employs the previously established assumption that the overestimate in revenue as a result of complete future knowledge is small [11, 200, 207–210]. A more sophisticated model would be necessary to accurately describe how a large storage system impacts its market, but the proposed model is adequate for small storage systems and provides an upper bound on the utility of future systems, since corrections to the model would result in reductions to net revenue.

5.2.4 Establishing performance parameters

A complete understanding of both the revenue generated and the cost incurred by any given hybrid or storage system is necessary to draw any conclusions about its economic viability. A dimensionless performance parameter χ is proposed to represent the effectiveness of an arbitrary energy generation or storage system. It is defined as the ratio between the revenue generated over the course of a year, and the levelized cost of operating the plant over the course of year, such that a plant with a performance parameter greater than 1 is profitable. In general, plant costs could be due to both levelized capital costs and operating costs, but this analysis focuses on plants in which capital costs are dominant, as is the case for many existing energy

storage technologies [120]. It is worth noting that for a given plant configuration, the system cost is fixed, so the optimization of revenue previously described is adequate to maximize χ.

For a given site and choice of generation technology, adding additional storage energy and power increases both the revenue and the cost of the proposed plant. To understand these tradeoffs, plant performance χ can be calculated for an arbitrary storage system with a peak power of $\dot{E}_{\text{max}}$ and E_{max} hours of storage at peak power given the optimized net revenue R_{total} and knowledge of the power and energy-related specific costs of the storage technology employed in the system $C_{\text{storage}}^{\text{power}}$ and $C_{\text{storage}}^{\text{energy}}$, such that for a given location and configuration:

$$\chi = \frac{R_{\text{total}}}{C_{\text{gen}} + \dot{E}_{\text{max}}(C_{\text{storage}}^{\text{power}} + E_{\text{max}} C_{\text{storage}}^{\text{energy}})} \tag{5.5}$$

This performance parameter was calculated over a wide range of system configurations, technology costs, and locations, as summarized in Table 5.1. All calculations assumed a lifetime of 20 years and a discount rate of 5%.

Table 5.1: Experimental parameter space investigated

Parameter	Unit	Values
Location	-	TX, CA, MA
Generation Technology	-	Wind, Solar, Arbitrage
Peak Power	$\text{MW}_{\text{storage}}\ \text{MW}_{\text{generation}}^{-1}$	0 - 5
Energy	hrs storage at peak power	0 - 4
Efficiency	-	90%
Energy Related Storage Cost	\$ kWh^{-1} storage	10 - 700
Power Related Storage Cost	\$ kW^{-1} storage	10 - 400
Generation Related Cost	\$ kW^{-1} generation	1000, 2000, 4000

5.2.5 Optimal system selection

For any given choice of generation technology and storage technology, a system designer must specify the storage subsystem's energy and power ratings. This decision

is a function of many inputs, including the local pricing dynamics, the availability of the renewable resource for recharging, as well as the energy- and power-related costs of the energy storage technology. The performance parameter data determined from the optimization analysis was used to determine the optimal storage size as a function of all these inputs. This reduces the dimensionality of the dataset to the point where it is system size independent. At this level, direct comparisons between two storage technologies with different energy- and power-related costs can be made for a given site and generation technology. At this level of analysis, tradeoffs between energy storage technologies can be quantified.

5.3 Results

5.3.1 Introduction

Four principle results are presented here. First, the increase in revenue generation for optimally operated hybrid generation/storage plants is considered as a function of storage system size. This effect is a result of the hybrid plant's ability shift plant output to periods of high pricing. Second, the increased revenue of a hybrid plant can be weighed against the increased cost of incorporating storage. The costs of storage and generation play a key role here, and result in an optimal system size to maximize the economic performance of the system. Third, the behavior of hybrid systems is compared to that of pure storage systems. Since the key distinction between these two systems is the limited availability of energy to recharge the storage system, a direct comparison allows for an understanding of this difference. Lastly, by comparing optimally sized systems that vary only as a function of location, generation profile, and technology costs, the tradeoffs between storage technologies with very different cost intensities can be quantified.

5.3.2 Storage shifts output into periods of high prices

When operated on the real-time market to maximize revenue, the principle purpose of energy storage is to shift output from periods of low demand and low prices to periods of high demand and high prices. Figure 5-3 illustrates this effect by looking at the representative case of a storage system with a power of one MW MW_{gen}^{-1} and an energy rating of four hours over the course of four days in the spring, summer, fall, and winter. Regardless of the generation profile (wind, solar, or arbitrage) or local pricing dynamics, (Texas, California, or Massachusetts) incorporating storage resulted in a reduction of output during periods of low prices, and an increase in output during periods of high prices. The charge rate for the storage system was capped by the renewable generation resource, which prohibited buying energy back from the grid. The ability to output energy to the grid at peak power during periods of high price is therefore limited by the availability of sufficient renewable generation to charge the storage system in advance. This effect is demonstrated in the fall California wind data, where there is insufficient to adequately charge the storage in advance of price spikes. Although the pricing dynamics in each of the three markets are very different, the effect of storage in each case is to concentrate the output into short bursts during periods of high pricing.

The net result of this time shifting is that for a given plant, increasing the power and energy of its storage system increases the plant's average transaction price and revenue. Figure 5-4 illustrates how the transaction price increases along with the storage subsystem size. Although the average transaction price without storage is lower for wind than solar, as energy storage increases, the pricing distribution and mean transaction price become increasingly similar. One key aspect of this result is that the additional revenue a storage subsystem can generate is limited by local pricing patterns and the amount of power that the storage system can produce during periods of high pricing.

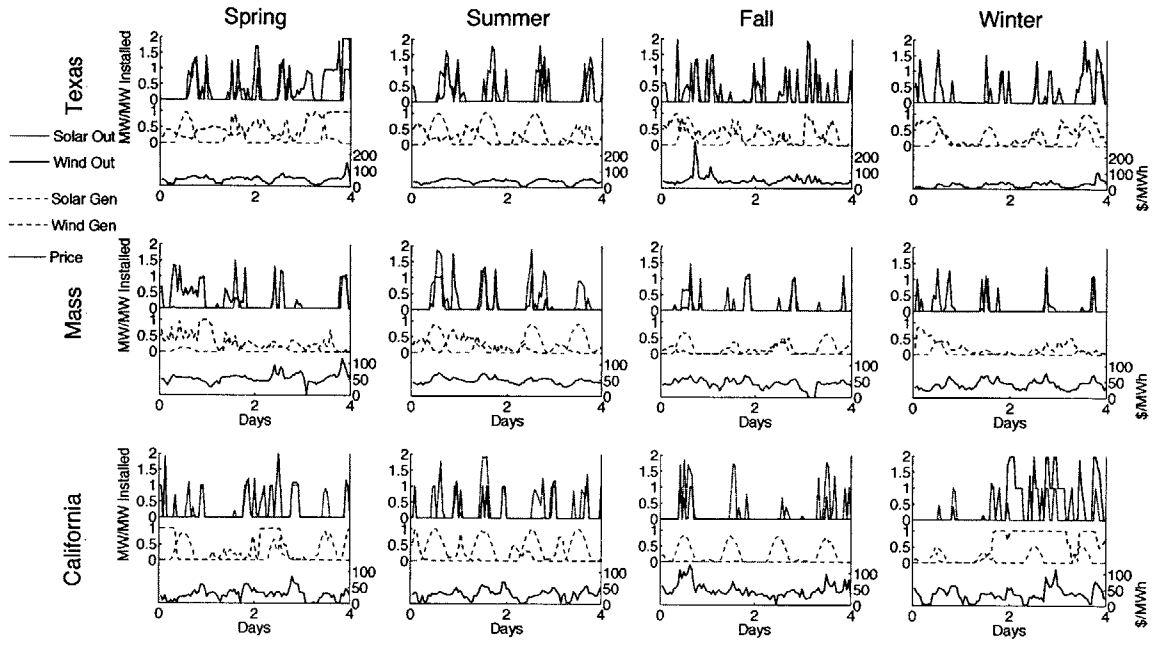

Figure 5-3: Optimized output from hypothetical hybrid plants with a specific storage power of 1 MW MW_{gen}^{-1}, a storage energy of 4 hrs at peak power, and a roundtrip efficiency of 90%. Storage serves to shift the plant output from the real-time generation profile to periods of high prices.

5.3.3 Balancing increased revenue with storage cost

Additional storage increases the revenue that a plant can generate, but also increases the capital costs of the plant. The balance between increased revenue and increased costs can be examined by considering the dimensionless ratio χ between annual cost and annual revenue, as defined by Equations 5.5. Depending on the cost of storage and generation, and assuming a 5% discount rate and a 20 year lifetime, the cost of the system can then be directly compared to the revenue of the system. Figure 5-5 shows how χ varies as a function of storage system power and energy for the case of a hybrid wind plant sited in Texas.

The contour plots illustrate two key findings: firstly, that if a sufficiently inexpensive storage technology is used, the additional revenue generated by the storage system outweighs its cost up to some optimal system size. Secondly, the optimal system size and performance is a strong function of the energy and power-specific storage costs, as well as the cost of generation. As might be expected, storage sys-

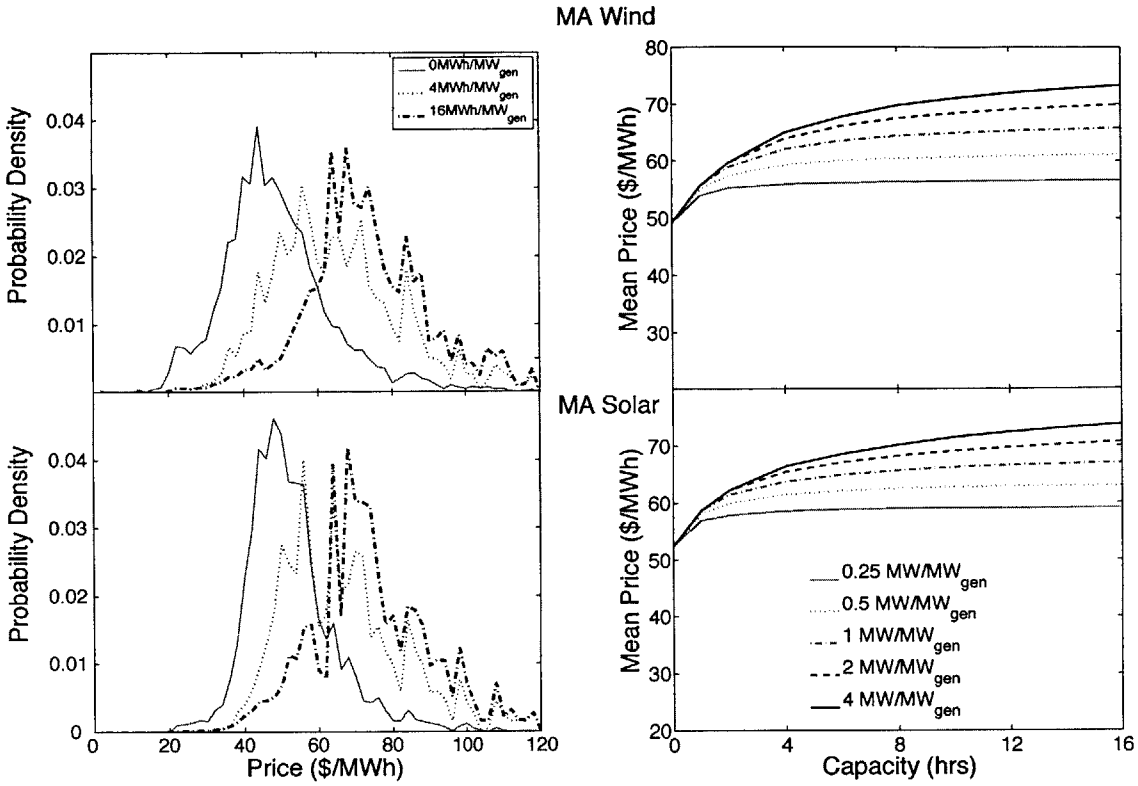

Figure 5-4: Adding additional storage allows a hybrid plant with a specific storage power of 1 MW MW_{gen}^{-1} to shift its output to periods of high pricing for both wind (a) and solar (c). Depending on the power rating of the storage subsystem, additional energy can increase the average transaction price up to some threshold, regardless of generation profile (b + d). A roundtrip efficiency of 90% is assumed.

tems that used technologies with higher energy-related costs, such as supercapacitors or flywheels, produced better economic performance when they were specified with lower energy and higher power relative to their generation resource, as shown in the bottom right of Figure 5-5. The opposite is true of systems with higher power-related costs, such as flow batteries or fuel cells. Regardless of storage technology cost behavior, as the cost of the generation technology drops, the cost of storage must also drop to match. The complete set of contour plots is available in the supplementary information.

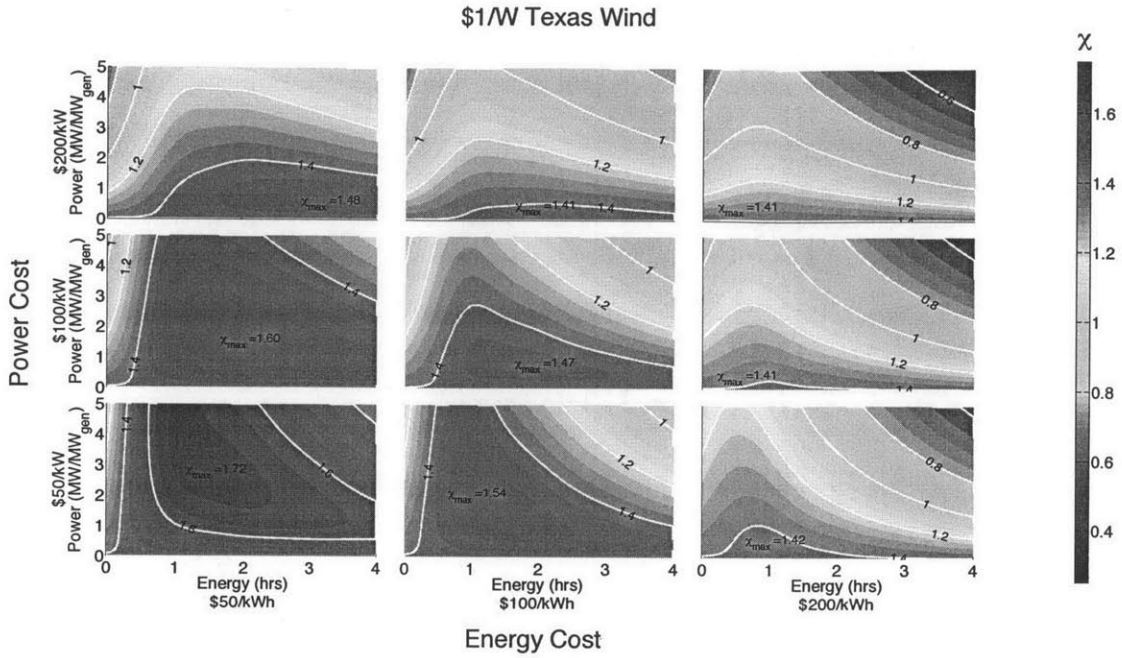

Figure 5-5: Dimensionless performance of hybrid wind turbine/storage plant sited in Texas as a function of storage system size assuming a turbine cost of \$1 W^{-1} and a roundtrip efficiency of 90%. Varying the energy and power-related costs of the storage technology has a significant impact on performance, with low energy cost technologies favoring a high energy storage system, and low power cost technologies favoring a high power storage system. A system lifetime of 20 year and a discount rate of 5% was assumed to determine the annual system cost. In the absence of storage, $\chi = 1.41$ for the wind turbine alone

5.3.4 Comparing storage performance at the technology level

Figure 5-5 shows that adding storage to a renewable generation plant improves economic performance only to a point, beyond which the cost of the storage outweighs its benefits. A secondary optimization process is performed to determine the sizing of large-scale energy storage. By selecting the system configuration from datasets as shown in Figure 5-5 that produce the optimal performance, optimal system size and cost can be determined as a function of the energy- and power-related cost intensity of the storage technology. Given the wide array of available technologies, a quantitative metric to compare their suitability to a particular application is critical. Assuming an optimally sized system, where that size can vary depending on the energy- and power-related cost of the storage technology, the dimensionless performance param-

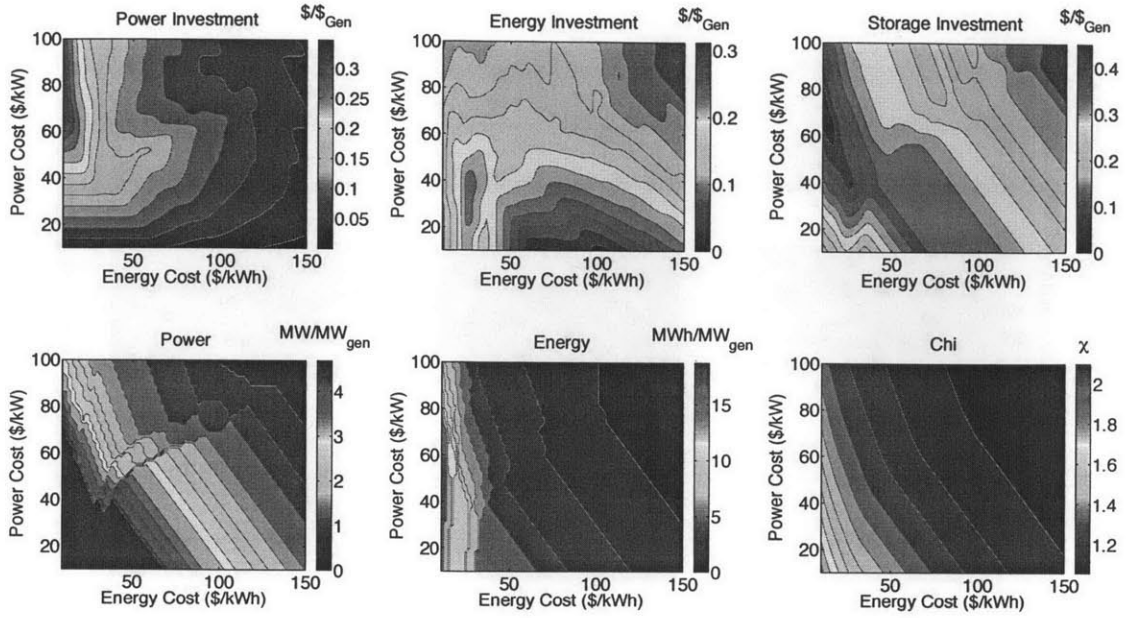

Figure 5-6: The power-related, energy-related, and total cost of the storage subsystem in dollars per dollar spent on the generation subsystem (top), and the optimal storage power, storage energy, and total performance (bottom) for a hybrid wind storage system located in Texas with a generation cost of \$1 W^{-1} and an efficiency of 90%. The roughness in the data is due to granularity in the dataset where the algorithm was forced to choose between more power and less energy and more energy and less power.

eter χ allows for such a comparison. Figure 5-6 shows how the optimal storage size, investment, and performance varies as a function of energy- and power-related cost intensity. As the cost of storage increases, its benefit justifies that additional cost up to some threshold investment, beyond which the investment drops.

Although the dimensionless performance of the hybrid systems vary significantly with the cost of generation and local pricing dynamics, the marginal tradeoff between power-related cost and energy-related cost for the storage system is very consistent across diverse datasets, as shown in Figure 5-7. This result can be compared directly with existing energy storage technologies. In particular, recent work has estimated the power- and energy- related specific costs of a number of energy storage technologies in a similar manner to this study [13]. These results are summarized in Figure 5-8. The most important implication of this result is that if two competing technologies with different cost profiles can be configured to produce similar performance at one

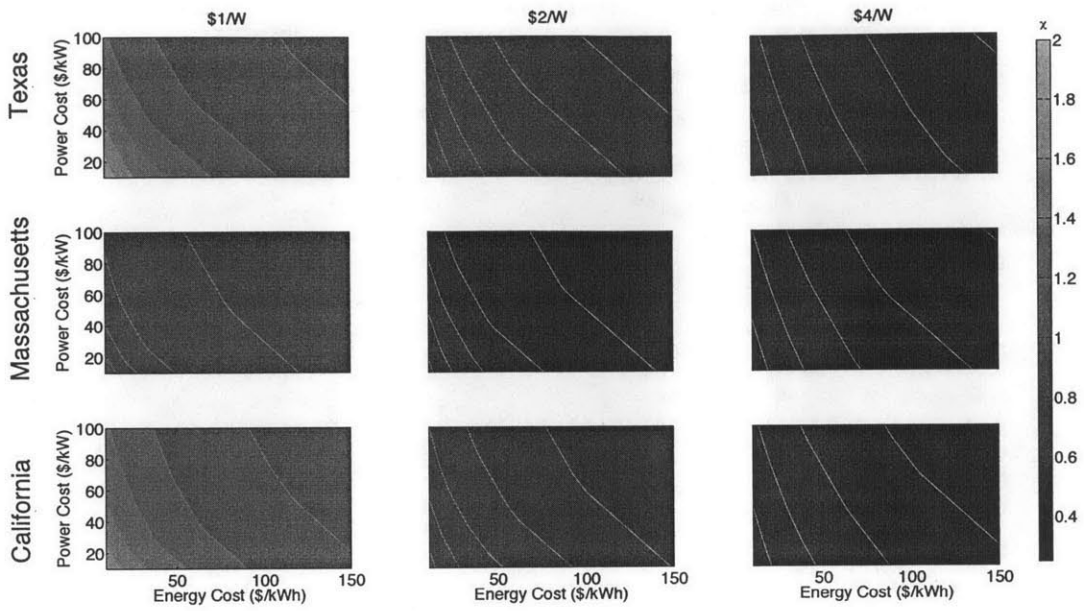

Figure 5-7: Optimal performance of a hybrid storage wind plant as a function of location and cost intensity of the generation and storage technologies.

site, it is likely that they will also perform similarly to each other at a different site, independent of generation resource and pricing behavior. The exact cause of this relationship remains unknown, and is a subject of further study.

5.4 Discussion

The first part of this chapter establishes economic performance targets for existing storage technologies to apply them to large-scale renewables integration by acting on the real-time energy markets. Among the wide variety of grid-scale needs identified for energy storage [211], large-scale renewables integration remains an key application. The analysis presented here provides a decision making process with which system size choices can be made in order to maximize the economic value of a given renewable generation resource. The resulting optimal system size varies strongly depending on the cost profile of a given storage technology, with a weaker dependence on local pricing dynamics and the renewable resource output profile.

The second part of this work deals with the tradeoff between cost of storage per

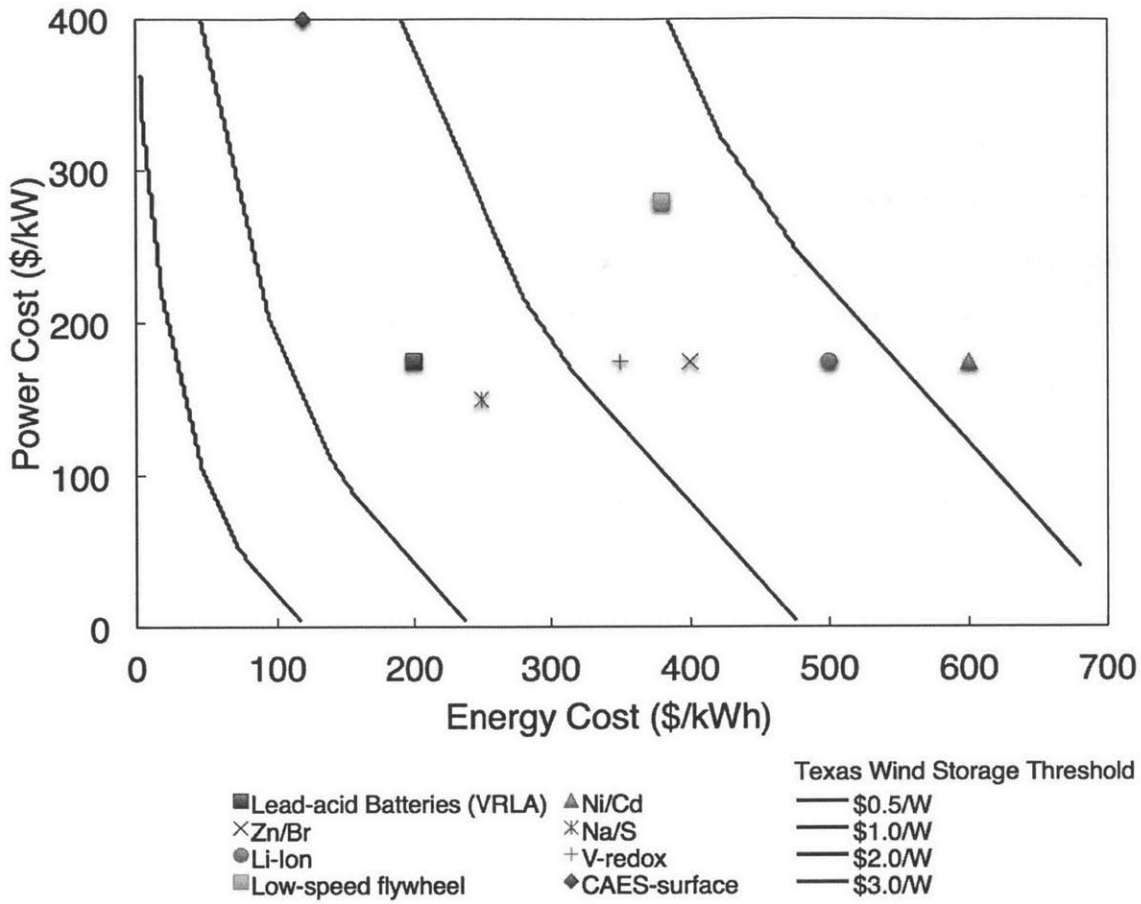

Figure 5-8: Cost intensities of a range of energy storage technologies overlaid with the threshold cost intensities at which it becomes profitable to incorporate storage into a Texas wind farm with a variable generation cost.

power and per energy of storage technologies, and how this tradeoff impacts the ability of energy storage to improve the economic performance of renewable generation. A set of storage performance targets is derived by optimizing storage system size for each site and generation technology. These targets can be thought of as the maximum cost intensity that the storage system can have while still having a positive effect on the economic effectiveness of the generation technology. Since the cost intensity of storage must be considered in terms of both cost per energy and cost per power, these targets are actually contours as shown in Figure 5-8.

Although the specific cost targets vary widely depending the generation resource and local pricing dynamics, the technology-level tradeoff between cost per energy and cost per power appears to be largely independent of the site location, generation pro-

file, and generation technology cost. Despite wide disparities in the pricing dynamics of the three markets considered here, as well as the variation in resource availability, there is a clear and consistent relationship between optimal system performance and the energy- and power-related costs of the storage technology. In all cases, equal performance could be obtained from technologies with differing costs so long as they lay along iso-performance curves with a slope of roughly $1 - 2$ \$ MW^{-1} per \$ MWh^{-1}. This relationship could prove very helpful to evaluating current and future technology development, since at present there is no clear consensus on how to evaluate future energy storage technologies.

The precise source of this universal result from such disparate data is beyond the scope of this thesis, but one possible hypothesis is that the tradeoff comes from the characteristic timescale of periods of high pricing. Future work will include statistical analysis of real-time pricing data to examine how spikes in pricing are distributed. Simulated pricing data with more widely varying pricing behavior may also be considered.

In this chapter, optimal storage system behavior and sizing has been considered for hybrid renewable/storage plants using broad range of storage technology cost metrics. Although the specific performance of particular plants vary across locations and technologies, this work identifies universal tradeoffs between storage cost per power and per energy that appear to be universal across the entire dataset. This result can be applied as a common framework for evaluating and discussing widely disparate energy storage technologies, and can serve as a guide for development of energy storage technologies.

Chapter 6

Perspectives and Conclusions

6.1 Summary of Conclusions

In this thesis, the Hydrogen Bromine Laminar Flow Battery (HBLFB) has been investigated with the ultimate goal of providing low-cost and reliable energy storage for grid-scale applications. The results presented here demonstrate the potential of the HBLFB to accomplish those goals, and suggest that further efforts to realize the potential of this system are justified. The four major results are summarized below.

A proof of concept cell has been designed, implemented, and characterized. This cell demonstrated a power density of 795 mW cm^{-2} at room temperature and atmospheric pressure [146]. This result is the highest power density ever reported for a membrane-less electrochemical cell, and is within 7% of the highest reported power density for a traditional membrane-based flow battery at room temperature [3]. It also demonstrated 90% roundtrip voltage efficiency operating at 200 mW cm^{-2}, the first reported instance of a membrane-less laminar flow electrochemical cell being used for efficient energy storage.

Numerical and analytical models have been developed to accurately describe the performance of the HBLFB operating in charging and discharging modes [178]. These results are consistent with experimental results, and provide a greater understanding of the behavior of the demonstration cell investigated in Chapter 2. The numerical model expands on the present understanding of laminar flow electrochemical cells

by describing the flux of multiple ionic species to accurately describe both charging and discharging operation. The analytical model identifies the dominant physics and builds on boundary layer theory to predict the performance of an arbitrary laminar flow electrochemical cell with minimal computation expense. Polarization curves can be rapidly generated to approximate the current-voltage or arbitrarily-sized systems that agree well with experiment data.

Secondary flows generated by inertial effects near the inlet region of the HBLFB have been identified as the primary limitation on power density. This discovery has significant practical implications on the development of the HBLFB, with the redesign of the inlet region playing a key role in future efforts. Further, the physical phenomena underlying these flows have broad implications for any circumstance where two or more streams are combined.

Large-scale energy storage for the electrical grid is still in its infancy, and the performance metrics and targets that storage technologies must meet continue to evolve in parallel with the storage technologies themselves. A numerical model using fine-grained historical real-time market pricing across the United States has been developed to provide a framework for assessing the economic viability of energy storage technologies in terms of their energy- and power-related costs. At the appropriate price point, this model demonstrates that large-scale energy storage can increase the economic viability of renewable energy resources. The extent of this benefit depends on appropriately sizing the storage system, the availability of the renewable resource, and the local market pricing dynamics. This work presents a quantitative framework with which to evaluate energy storage technologies, with disparate energy- and power-related costs.

6.2 Perspectives

For the HBLFB to truly have an impact on the large-scale energy storage landscape, a major remaining challenge is to successfully scale the existing single cell up to a multi-cell stack capable of handling several MWh of energy. Unlike membrane-

based systems, the areal power density of membrane-less electrochemical systems is a function of the shape and size of the active area, so the optimal design of a multi-cell HBLFB stack requires a thorough understanding of the performance of the battery across a range of conditions. As summarized in Table 3.2, the average current density of a laminar flow battery scales inversely with the square or cube root of the length of the channel, depending on the channel geometry. At least from a pure performance perspective, shorter channels correspond to higher power density.

From an economic perspective, making the channels shorter covers a larger fraction of the potential active area with gaskets, reducing the overall system power output. The total cell area largely determines the overall cost of the stack, so maximizing the active portion of the cell is central to minimizing cost. A potential stack design illustrating this situation is shown in Figure 6-1.

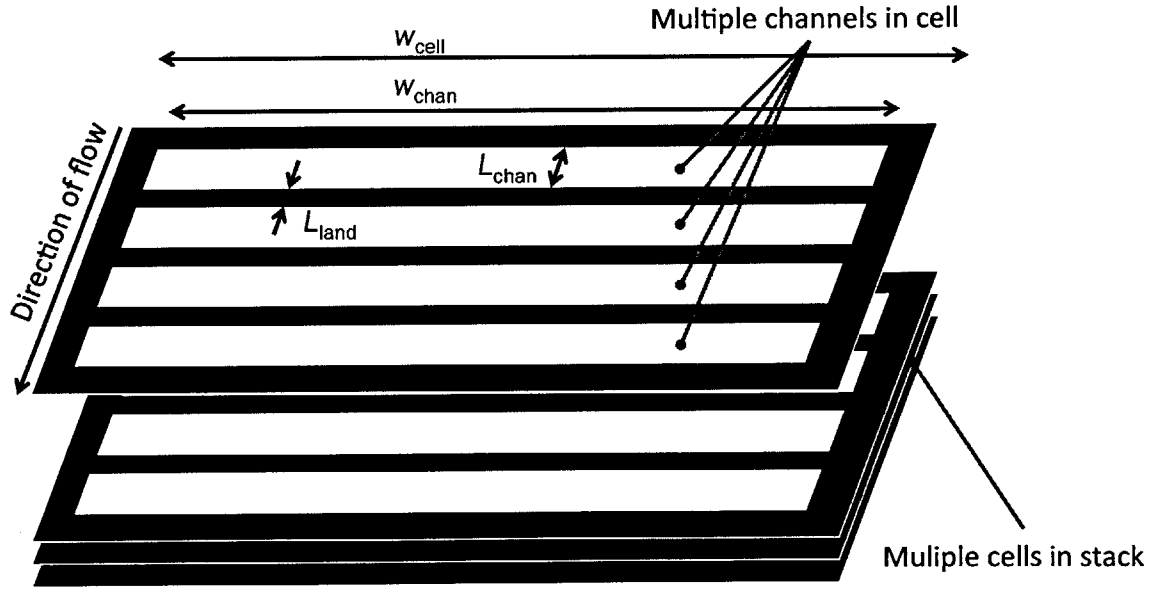

Figure 6-1: Layout of a multi cell HBLFB stack. Choosing the appropriate channel length L_{chan} relative to the inactive land spacing L_{land} is necessary in order to minimize cell cost ($\$ \text{ kW}^{-1}$) by trading off active area for maximum power density.

Using the analytical model derived in Chapter 3, it is possible to rapidly estimate the current-voltage performance of a proposed HBLFB system of arbitrary size. For the purpose of this calculation, it is assumed that the channels are much wider than

they are long to ensure fully two-dimensional flow. This assumption allows the channel width, w_{chan}, to be treated as roughly equal to the cell width, w_{cell}. Depending on the required efficiency, the maximum power density and percent active area can be calculated as a function of channel length for a particular channel height, h_{chan}, and flow rate expressed as the cell Reynolds number, $\text{Re} = \rho \bar{U} h_{\text{chan}} \mu^{-1}$. A sample calculation shown in Figure 6-2 illustrates the tradeoff between power density and percent active area. Because the cell must operate at lower currents relative to limiting current to achieve higher efficiency, reactant depletion and therefore the drop off in power density becomes less severe. Below a certain threshold efficiency, the cell simply operates at maximum power, causing the power output curves to converge.

By further assuming a particular areal specific cost, $c_{\text{materials}}$, and a land spacing L_{land}, the stack cost can be estimated as a function of channel length and operating efficiency, as shown in Figure 6-3. As the efficiency requirement increases, the system cost increases, since the cell must operate at lower and lower currents. More interestingly, increasing the efficiency requirement also increases the optimal channel length, since less bromine is consumed at the required lower current densities. The areal specific cost can be shown to have no effect on the optimal channel length, even as it has a very strong influence on the overall stack cost, as shown in Figure 6-4.

It is feasible to estimate the overall system cost of a grid-scale HBLFB system in terms of energy- and power-related costs as described in Chapter 5 by coupling these results to previous cost estimate studies for fuel cell systems [20]. Since stack components typical comprise roughly 25% of the overall cost, it is reasonable to target a power-related system cost of \$200 kW^{-1}. These components including balance of plant, power electronics, as well as bipolar plates, endplates, and the rest of the electrochemical stack, The energy-related cost of the HBLFB is dominated by the cost of the reactant tanks since reactant costs are roughly \$4 kWh^{-1}. Commercially available compressed hydrogen vessels have a cost of roughly \$25 kWh^{-1} [32]. Assuming that bromine can be stored for similar costs and assuming an additional 50% cost for packaging, assembly, and auxiliary systems, the HBLFB is estimated to have an energy-related cost of \$80 kWh^{-1}. These costs compare very favorably to previous es-

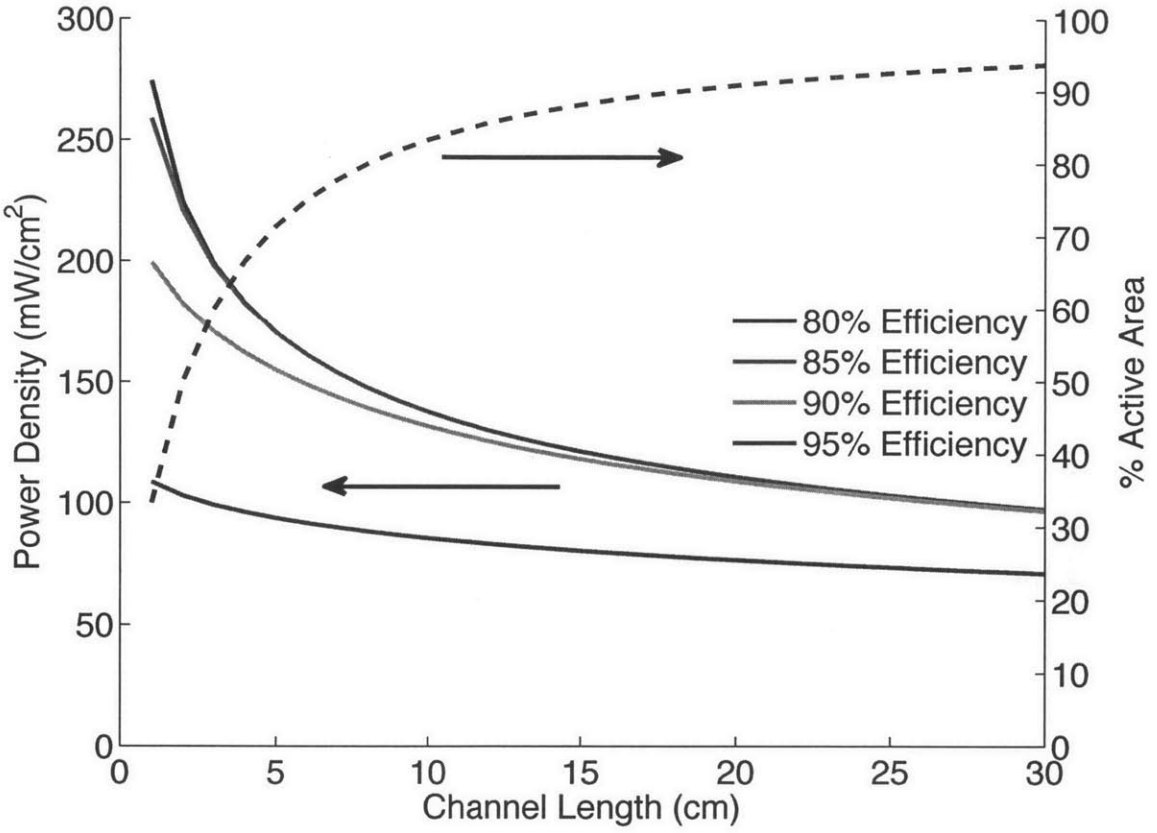

Figure 6-2: Analytically predicted HBLFB power output as a function of channel length and required roundtrip efficiency. Increasing the channel length resulted in decreased power density and increased percent active area. A channel height of 800 μm and a Reynolds number of 10 are assumed. For a specific areal material cost of \$10 m^{-2} and a land spacing of 2 cm, these results can be used to estimate the stack cost in \$ kW^{-1} as a function of channel length and minimum cell efficiency (b). An optimal channel length is observed that minimizes system cost, but depends strongly on required cell efficiency.

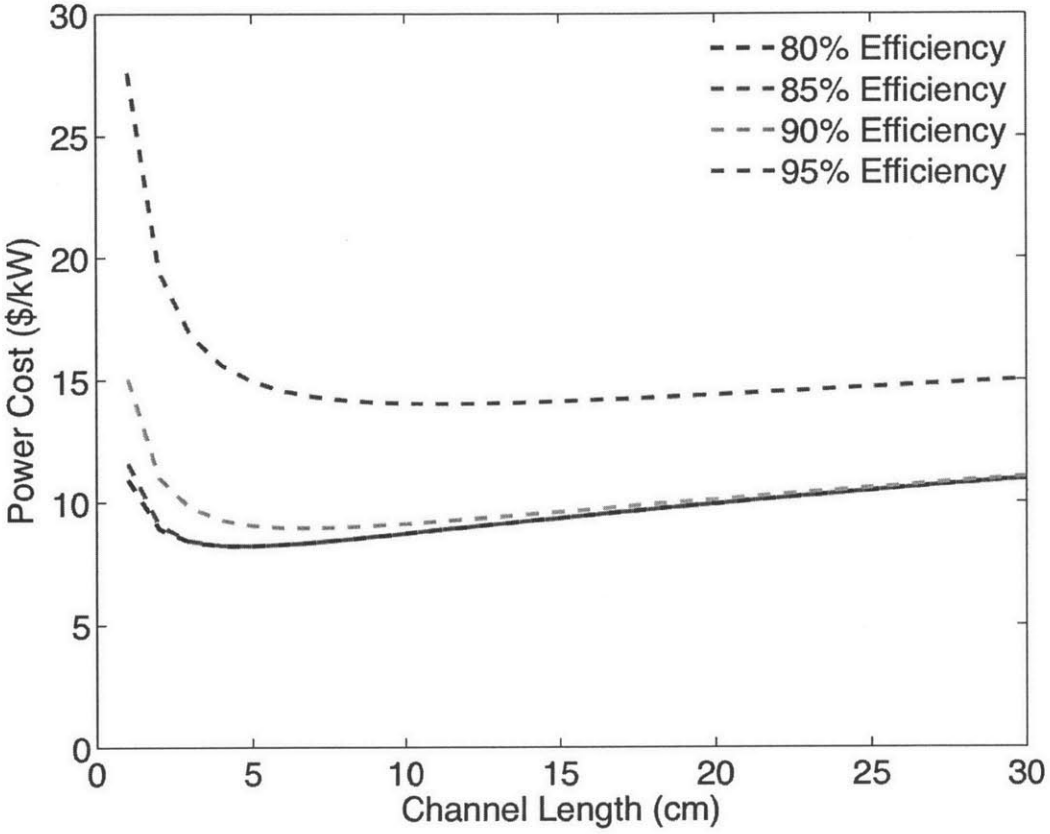

Figure 6-3: Stack cost in \$ kW^{-1} as a function of channel length and cell efficiency for a specific areal material cost of \$10 m^{-2}, a land spacing of 2 cm, and other conditions as specified in Figure 6-2. An optimal channel length is observed that minimizes system cost, but depends strongly on required cell efficiency.

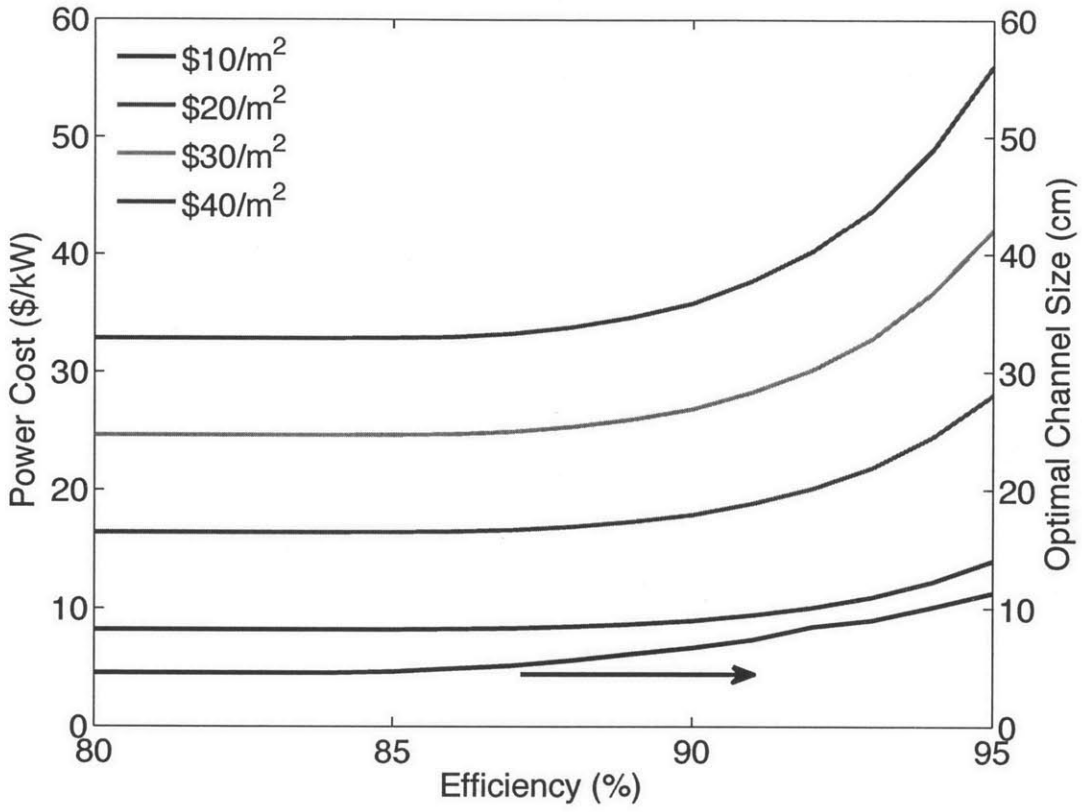

Figure 6-4: Optimal stack cost and channel length as a function of areal specific cost $c_{\text{materials}}$ and minimum operating efficiency. Other parameters are the same as in Figure 6-2. Areal specific cost strongly influences the overall stack cost, but has no effect on the optimal channel length.

timates for existing energy storage technologies, and suggest that a properly designed grid-scale HBLFB system has the potential to eventually outperform existing energy storage technologies. More tangibly, these cost estimates can be directly applied to the analysis from Chapter 5. For a solar photovoltaic plant sited in McCamey, TX with an installed cost of \$4 W^{-1}, for example, Figure A-14 demonstrates that incorporating an HBLFB energy storage system with the cost intensities predicted here would increase the economic performance of the plant by 35%. This result would necessarily vary depending on location, cost of generation, and local pricing dynamics, but such significant gains could certainly have a major impact on the electrical grid.

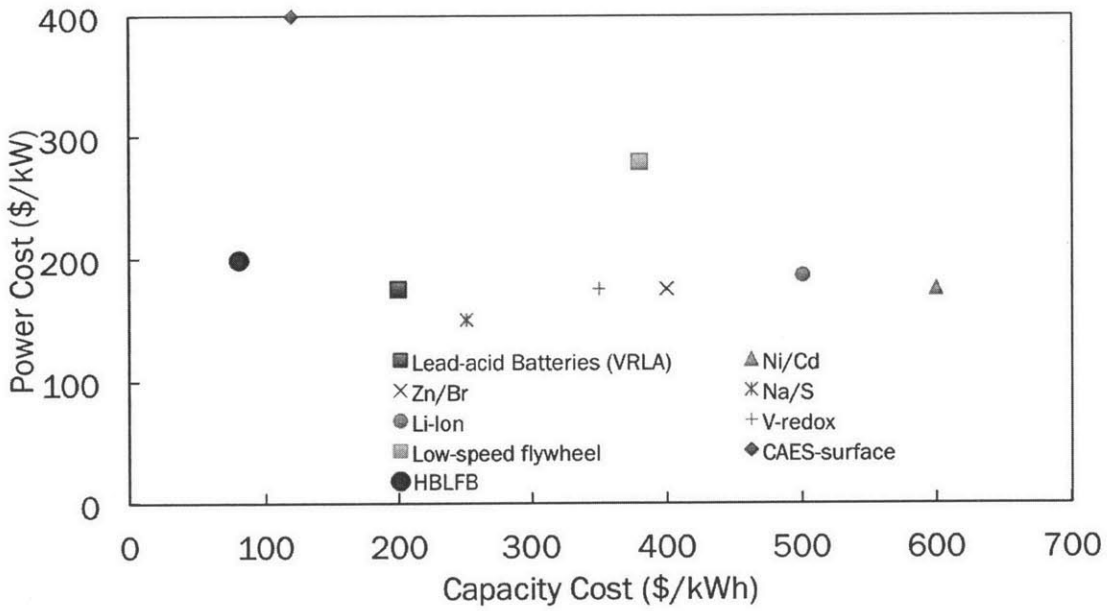

Figure 6-5: Power- and energy-related cost estimates for a range of energy storage technologies, including targets for the HBLFB. Data reproduced from Schoenung et al. [8].

Appendix A

Guidelines for Energy Storage: Supplemental Information

A.1 Balancing increased revenue with storage cost

The performance parameter χ was calculated for a range of storage system sizes, geographic locations, and generation resources, as outline in Table 5.1.

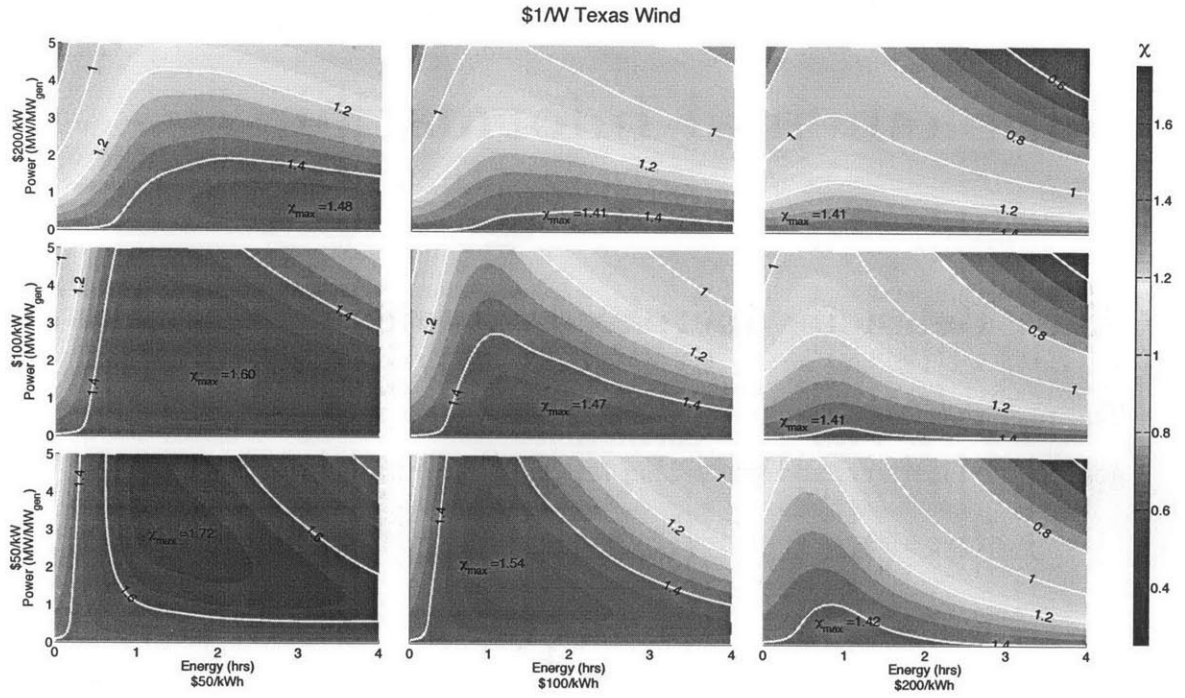

Figure A-1: Dimensionless performance of hybrid wind turbine/storage plant sited in Texas as a function of storage system size assuming a turbine cost of \$1 W^{-1} and a roundtrip efficiency of 90%. Without storage, $\chi = 1.41$.

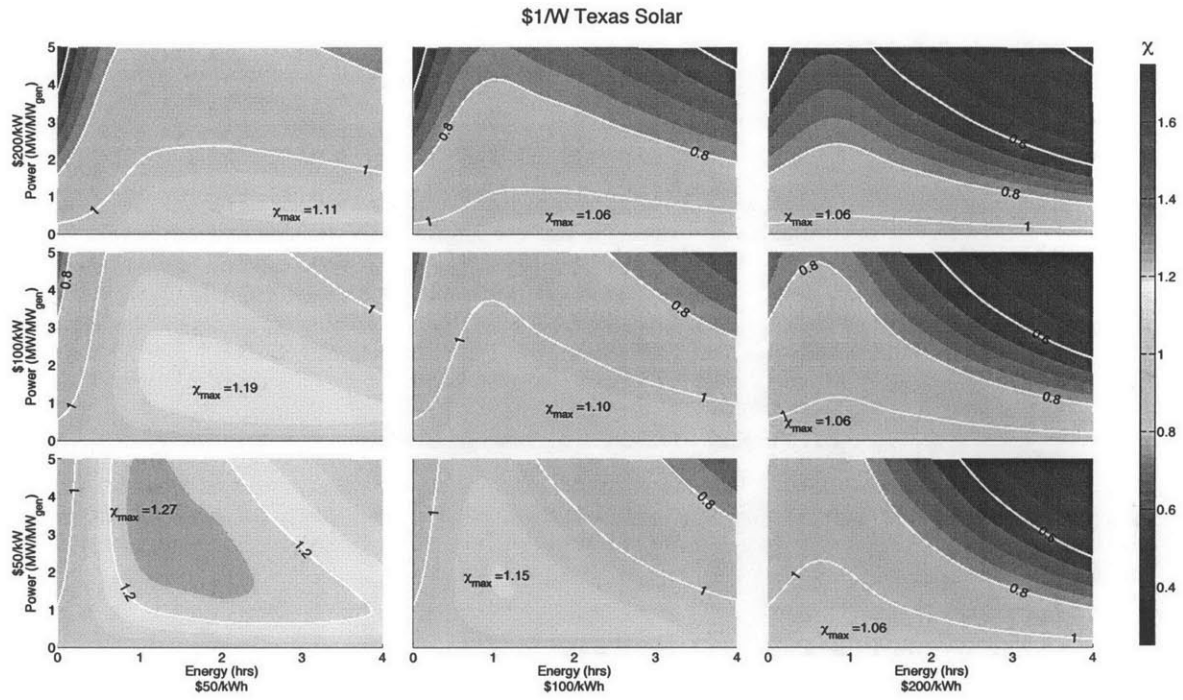

Figure A-2: Dimensionless performance of hybrid solar/storage plant sited in Texas as a function of storage system size assuming a turbine cost of \$1 W^{-1} and a roundtrip efficiency of 90%. Without storage, $\chi = 1.06$.

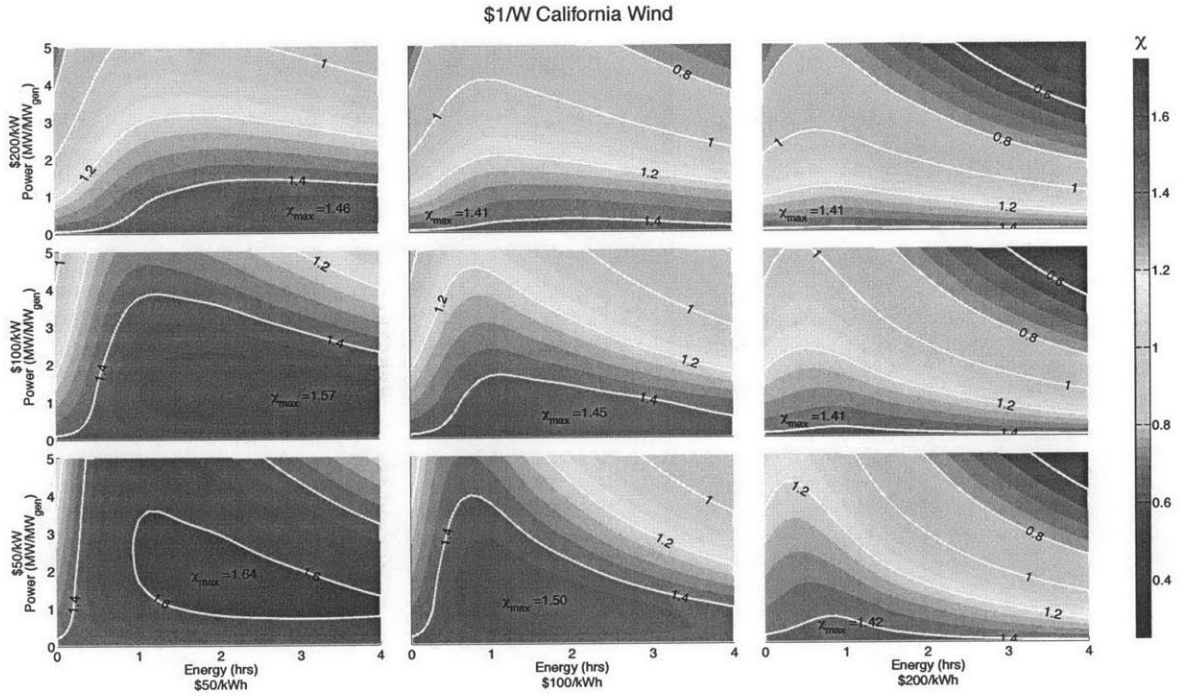

Figure A-3: Dimensionless performance of hybrid wind turbine/storage plant sited in Calfornia as a function of storage system size assuming a turbine cost of \$1 W^{-1} and a roundtrip efficiency of 90%. Without storage, $\chi = 1.41$.

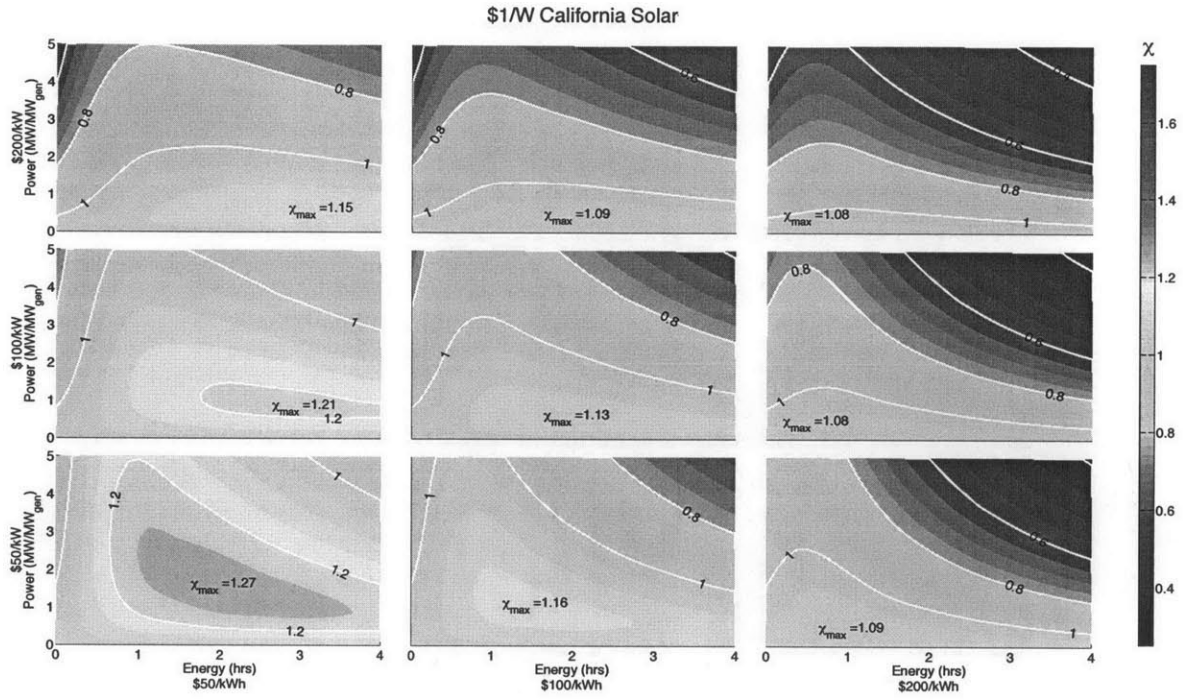

Figure A-4: Dimensionless performance of hybrid solar/storage plant sited in California as a function of storage system size assuming a turbine cost of \$1 W^{-1} and a roundtrip efficiency of 90%. Without storage, $\chi = 1.08$.

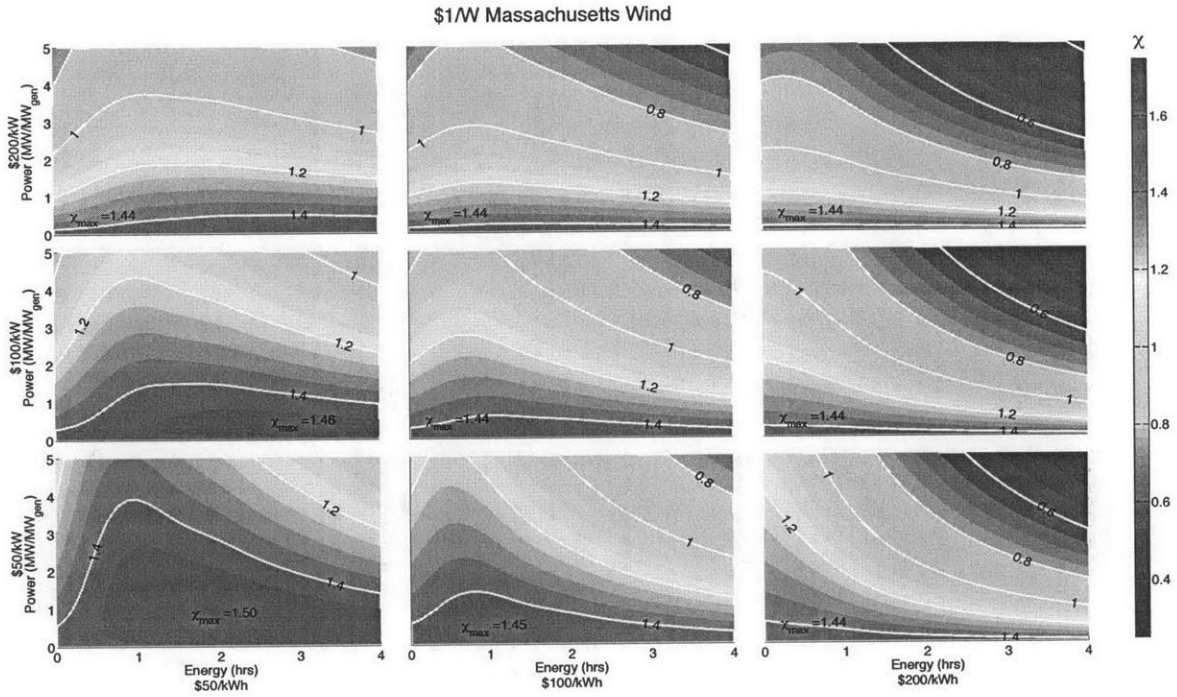

Figure A-5: Dimensionless performance of hybrid wind turbine/storage plant sited in Massachusetts as a function of storage system size assuming a turbine cost of \$1 W^{-1} and a roundtrip efficiency of 90%. Without storage, $\chi = 1.44$.

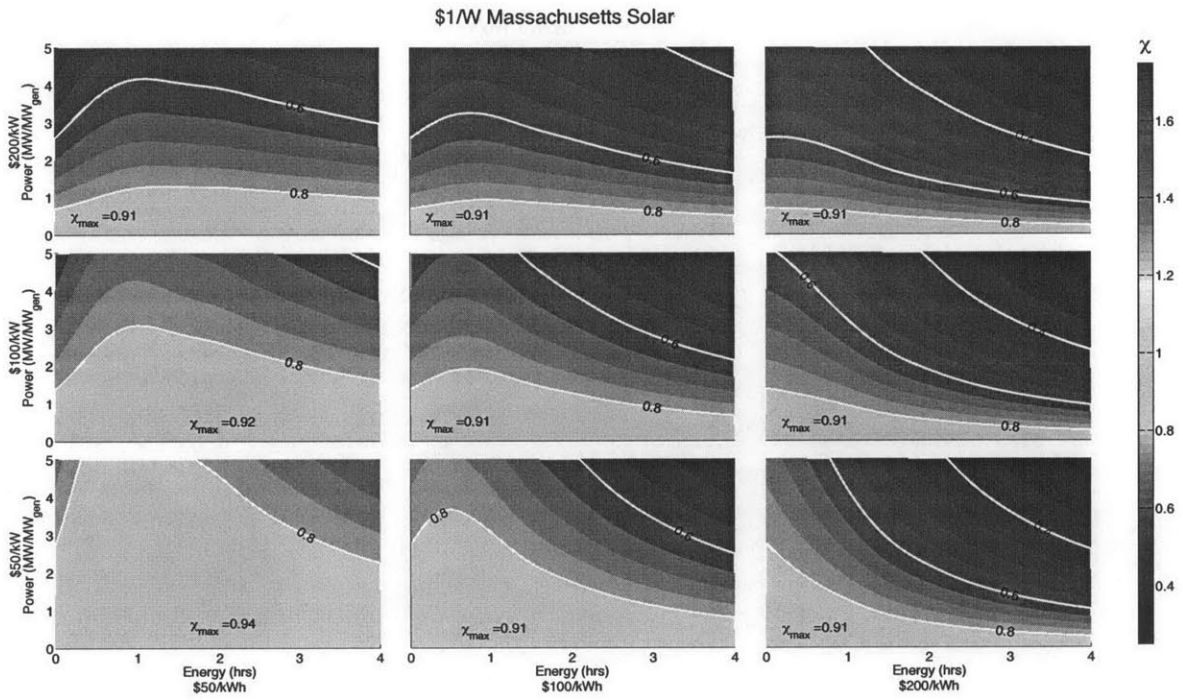

Figure A-6: Dimensionless performance of hybrid solar/storage plant sited in Massachusetts as a function of storage system size assuming a turbine cost of \$1 W^{-1} and a roundtrip efficiency of 90%. Without storage, $\chi = 0.91$.

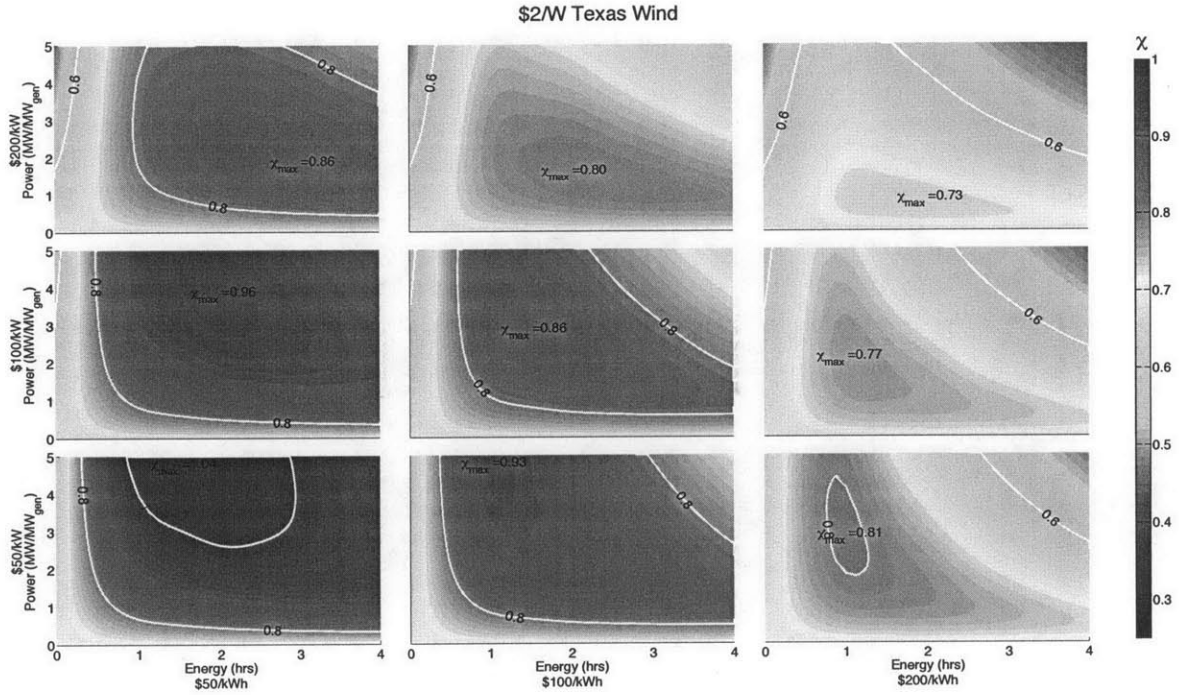

Figure A-7: Dimensionless performance of hybrid wind turbine/storage plant sited in Texas as a function of storage system size assuming a turbine cost of \$2 W^{-1} and a roundtrip efficiency of 90%. Without storage, $\chi = 0.70$.

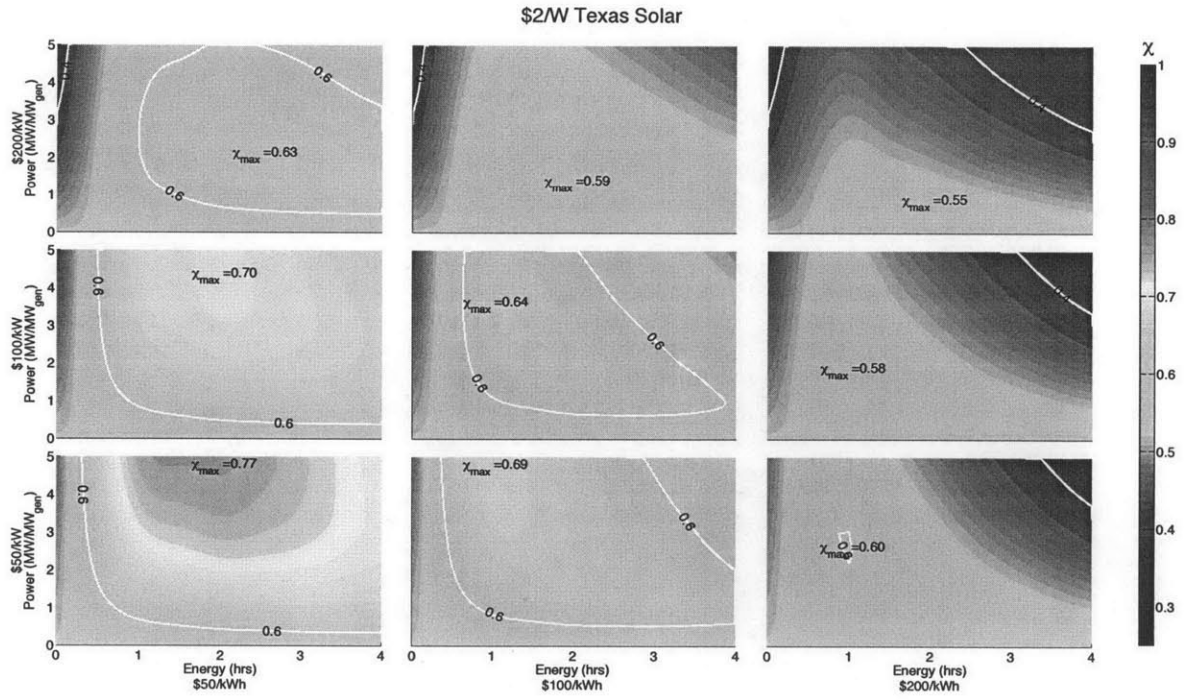

Figure A-8: Dimensionless performance of hybrid solar/storage plant sited in Texas as a function of storage system size assuming a turbine cost of \$2 W^{-1} and a roundtrip efficiency of 90%. Without storage, $\chi = 0.53$.

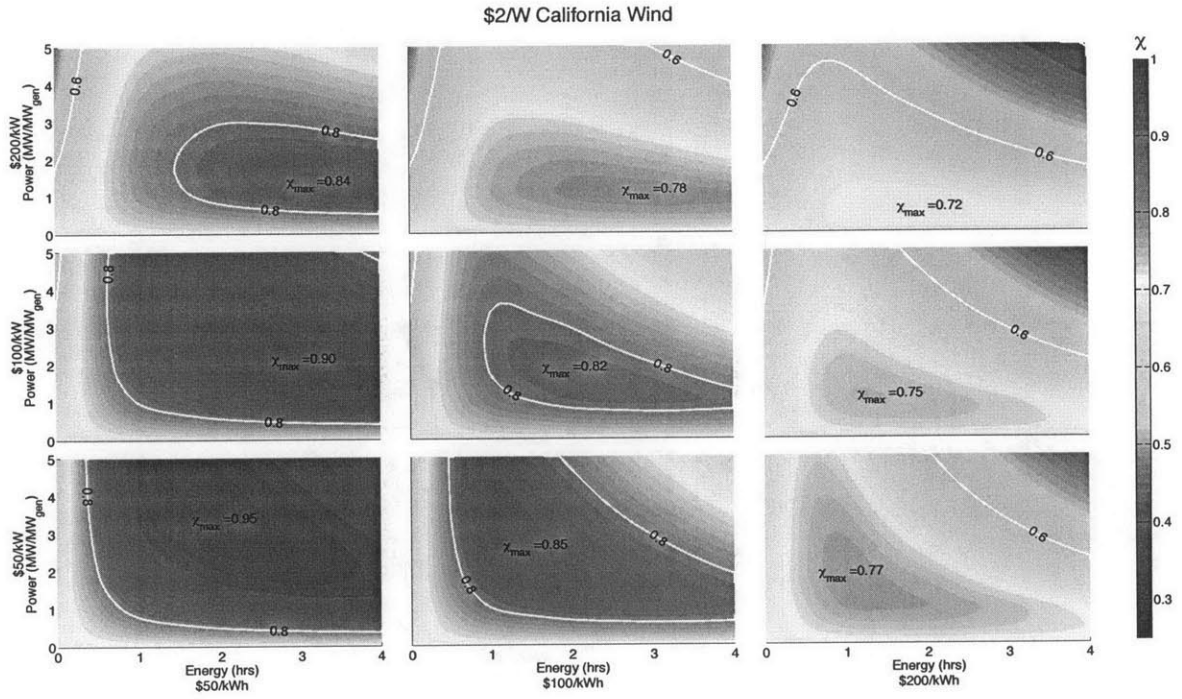

Figure A-9: Dimensionless performance of hybrid wind turbine/storage plant sited in Calfornia as a function of storage system size assuming a turbine cost of \$2 W^{-1} and a roundtrip efficiency of 90%. Without storage, $\chi = 0.71$.

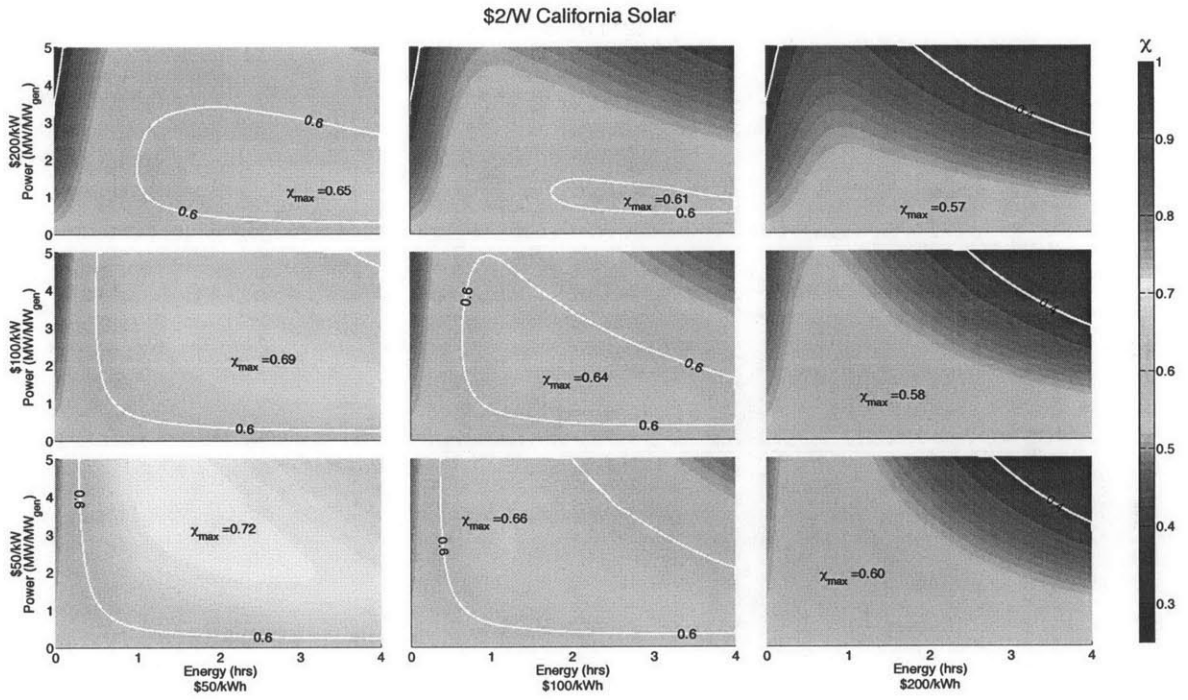

Figure A-10: Dimensionless performance of hybrid solar/storage plant sited in California as a function of storage system size assuming a turbine cost of \$2 W^{-1} and a roundtrip efficiency of 90%. Without storage, $\chi = 0.54$.

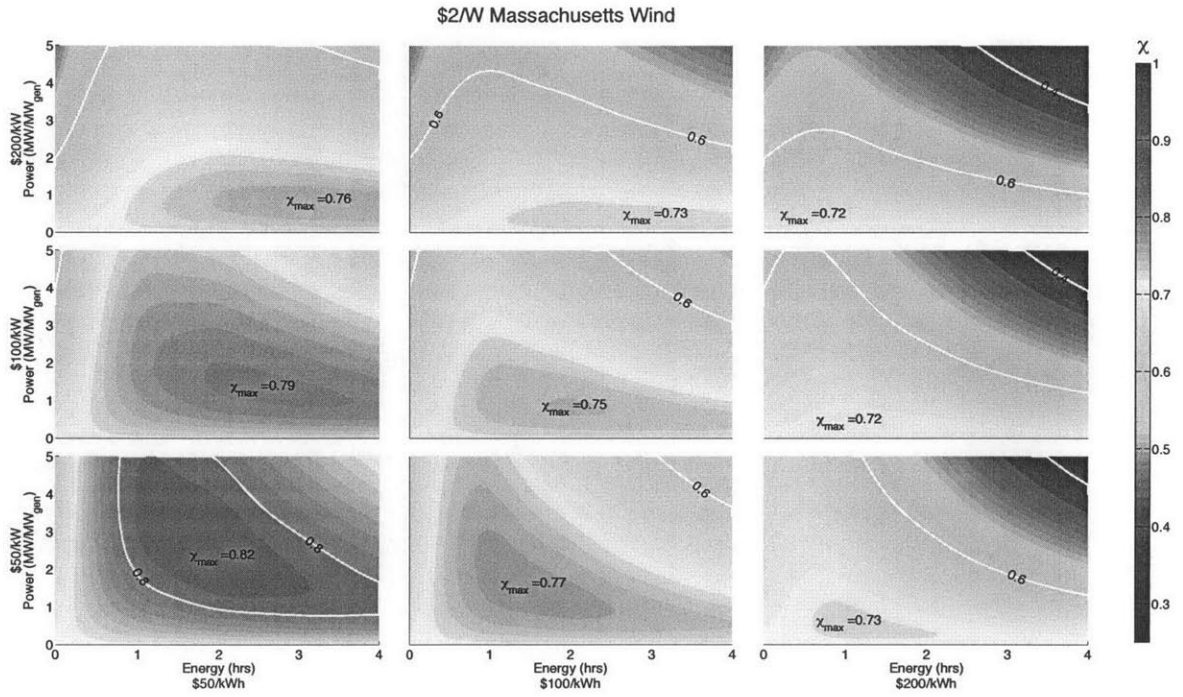

Figure A-11: Dimensionless performance of hybrid wind turbine/storage plant sited in Massachusetts as a function of storage system size assuming a turbine cost of \$2 W^{-1} and a roundtrip efficiency of 90%. Without storage, $\chi = 0.72$.

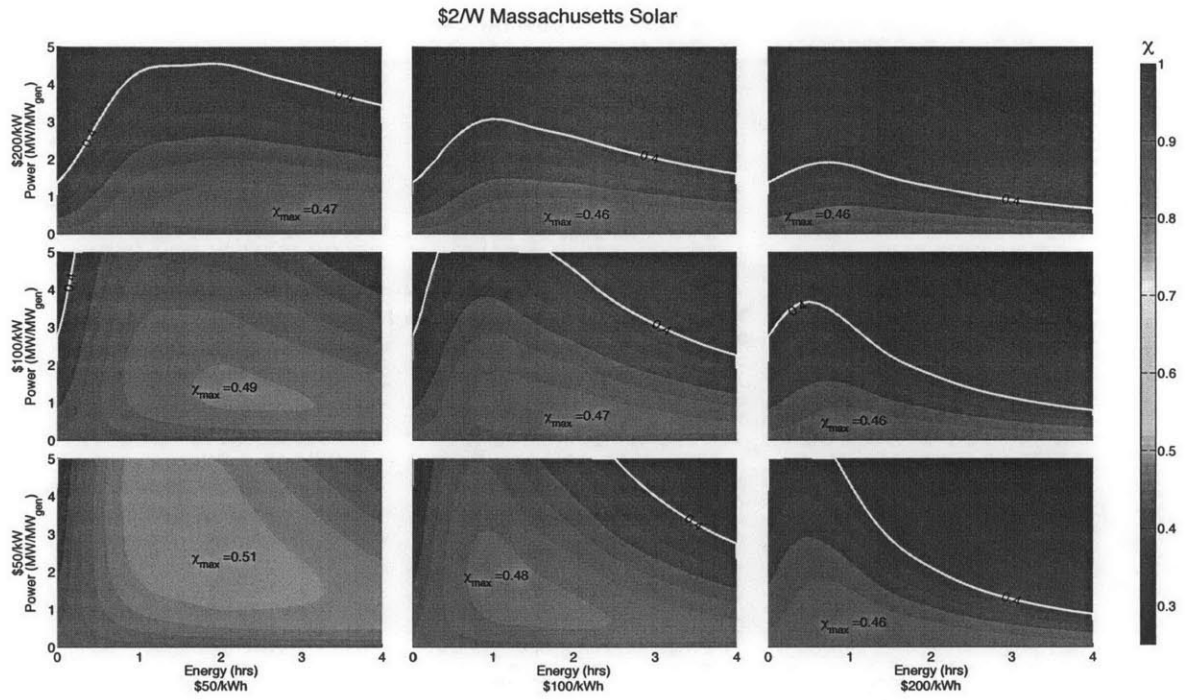

Figure A-12: Dimensionless performance of hybrid solar/storage plant sited in Massachusetts as a function of storage system size assuming a turbine cost of \$2 W^{-1} and a roundtrip efficiency of 90%. Without storage, $\chi = 0.46$.

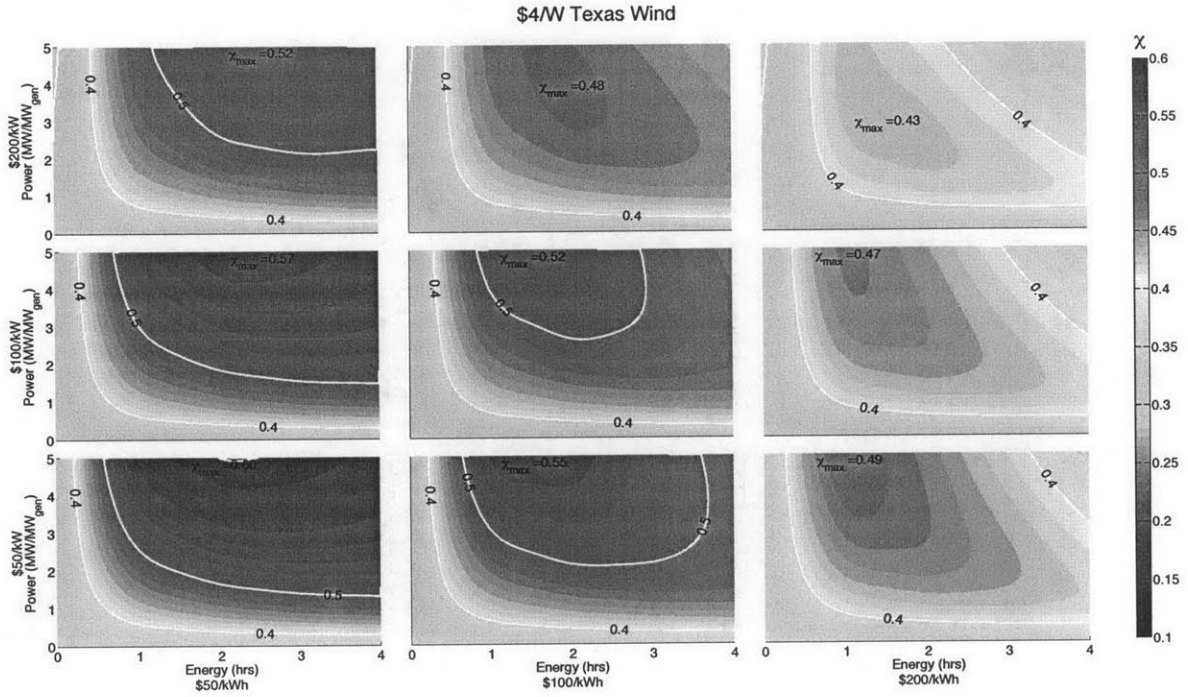

Figure A-13: Dimensionless performance of hybrid wind turbine/storage plant sited in Texas as a function of storage system size assuming a turbine cost of \$4 W^{-1} and a roundtrip efficiency of 90%. Without storage, $\chi = 0.35$.

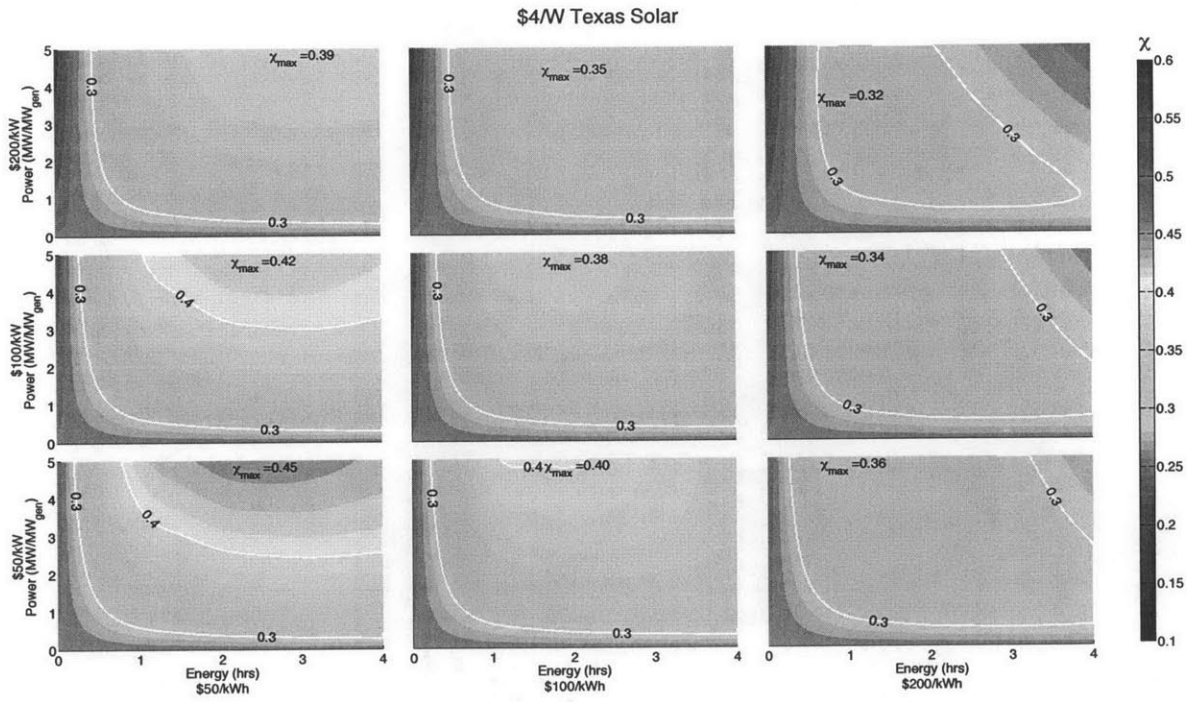

Figure A-14: Dimensionless performance of hybrid solar/storage plant sited in Texas as a function of storage system size assuming a turbine cost of \$4 W^{-1} and a roundtrip efficiency of 90%. Without storage, $\chi = 0.26$.

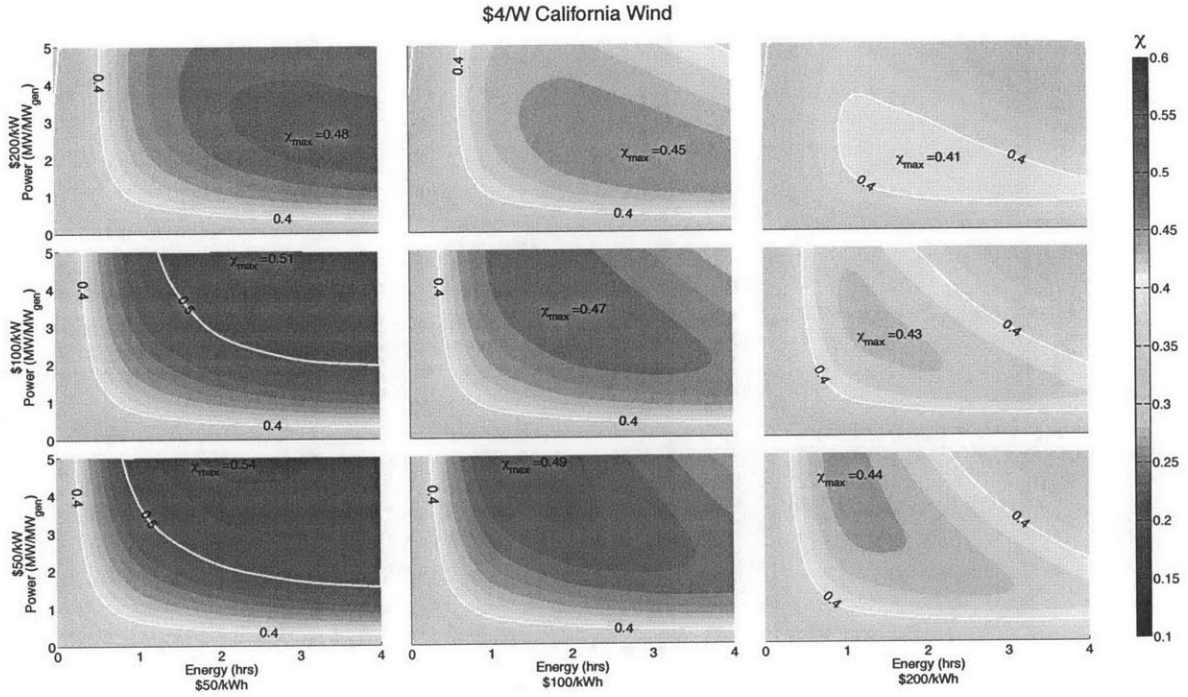

Figure A-15: Dimensionless performance of hybrid wind turbine/storage plant sited in Calfornia as a function of storage system size assuming a turbine cost of \$4 W^{-1} and a roundtrip efficiency of 90%. Without storage, $\chi = 0.35$.

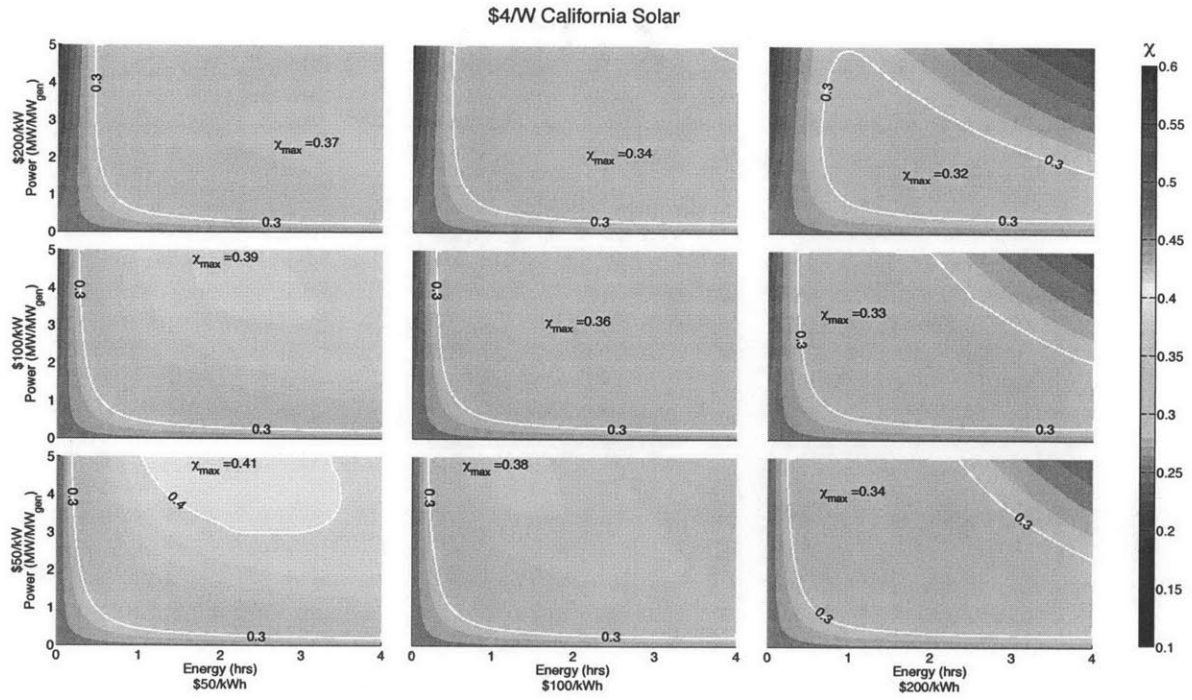

Figure A-16: Dimensionless performance of hybrid solar/storage plant sited in California as a function of storage system size assuming a turbine cost of \$4 W^{-1} and a roundtrip efficiency of 90%. Without storage, $\chi = 0.27$.

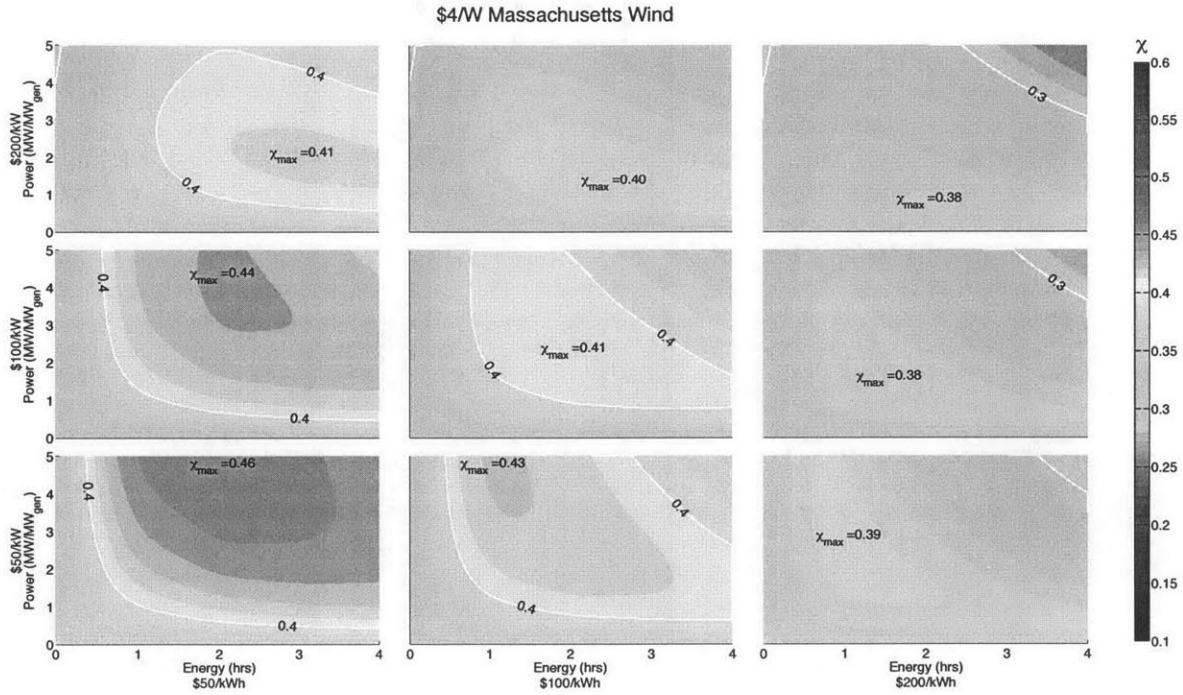

Figure A-17: Dimensionless performance of hybrid wind turbine/storage plant sited in Massachusetts as a function of storage system size assuming a turbine cost of \$4 W^{-1} and a roundtrip efficiency of 90%. Without storage, $\chi = 0.36$.

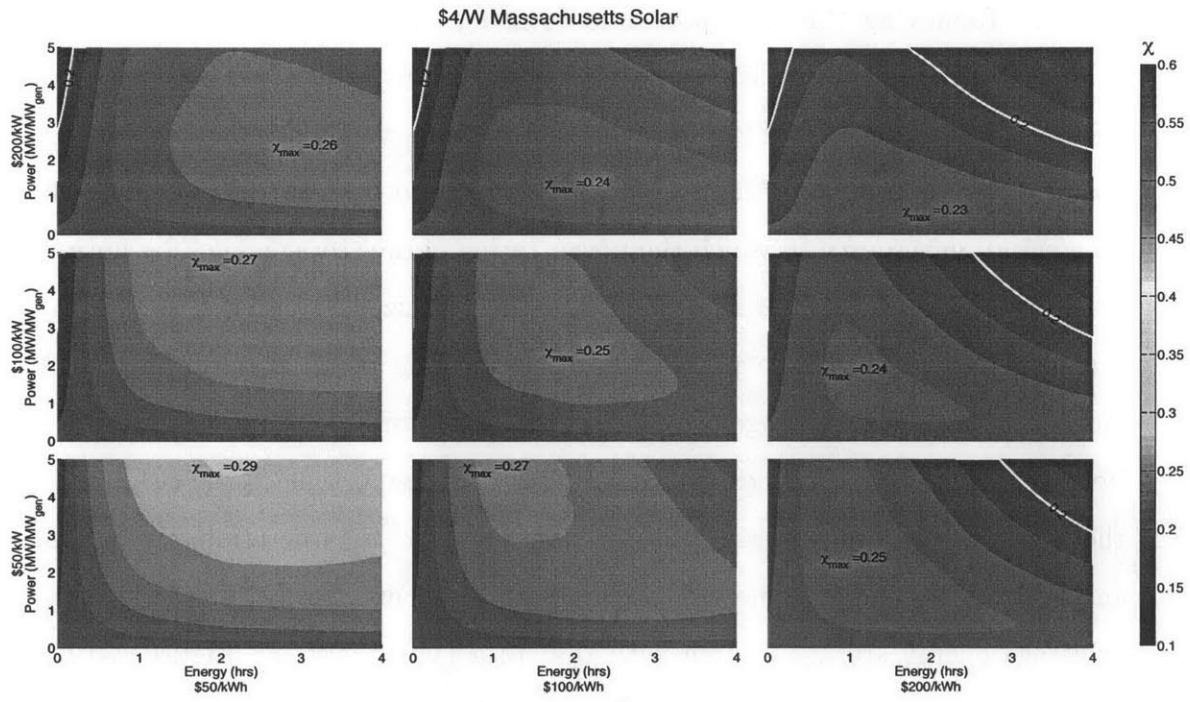

Figure A-18: Dimensionless performance of hybrid solar/storage plant sited in Massachusetts as a function of storage system size assuming a turbine cost of \$4 W^{-1} and a roundtrip efficiency of 90%. Without storage, $\chi = 0.23$.

A.2 Comparison of hybrid storage with pure arbitrage

One key assumed limitation of the hybrid systems considered in this analysis is that they cannot buy electricity back from the grid. This assumption limits the charging rate of the storage system, and means that the net performance of any given system is a function of both the cost of the generation resource and that of the storage system. Removing this limitation and focusing only on the storage system as an energy arbitraging system is instructive in that it illustrates a more clear connection between the cost metrics of the storage and any given system's economic performance. In addition, the number of design variables is reduced from two to one, since there is no generation resource to which the power rating of the storage much be normalized, leaving only the energy of the storage to be optimized. Figure A-19(a – c) plots dimensionless performance parameters as a function of rated energy for arbitrage storage systems with a range of cost metrics for the three sites considered. Although both cost per power and cost per energy are very important to the performance of the system, the cost per energy is the dominant factor in determining the optimal energy of the system. One can also directly compare the performance of a pure arbitrage energy storage system with that of a hybrid system. Figure A-19(d – f) plots performance as a function of discharge time for arbitrage and hybrid systems assuming an storage technology with a cost of \$100/kW and \$100/kWh, and a storage power rating of 1 $MW/MW_{generation}$ for the hybrid system.

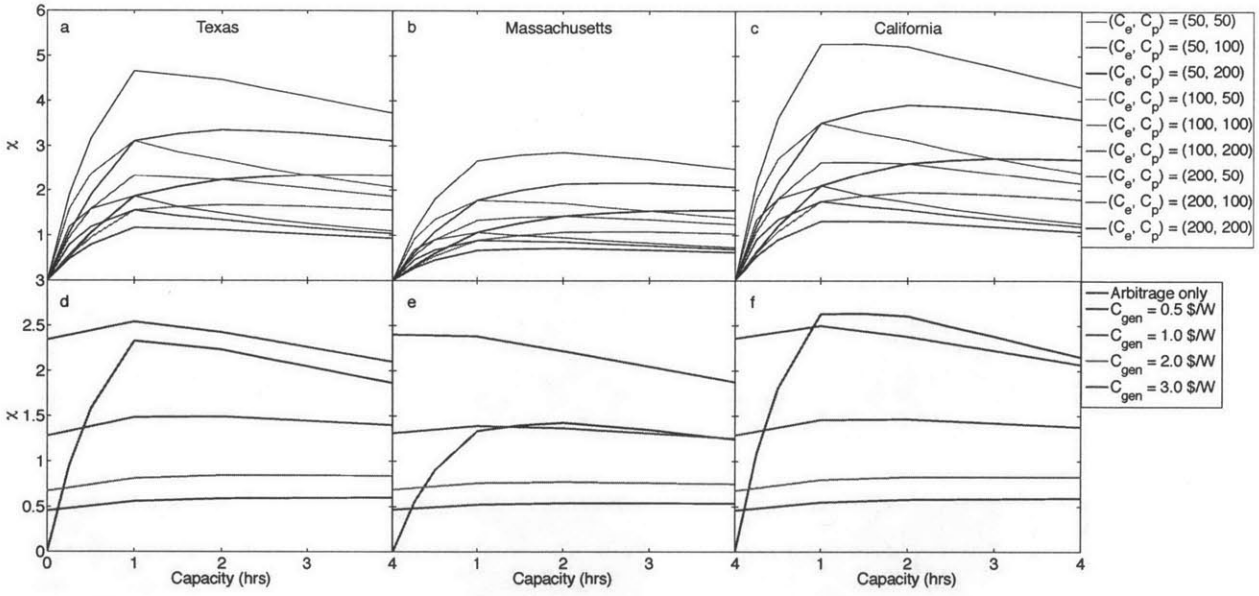

Figure A-19: Dimensionless performance parameter of pure arbitrage (a – c) systems as a function of cost per power and cost per energy for Texas, Massachusetts, and California sites. Performance of hybrid systems rated to 1 MW $MW^{-1}_{generation}$ (d – f) for the same locations depends strongly on the cost of generation, with pure arbitrage out performing the hybrid systems for generation costs above some threshold that is dependent on geography.

A.3 Performance and Design of Optimally Sized Systems

After optimizing the time-resolved behavior hybrid storage generation systems with variable energy and power ratings, it is desirable to select the optimally sized system to maximize χ. The figures in this section show optimal chi, optimal energy, and optimal power as a function of power- and energy-related cost intensity. Because only a discrete set of storage configurations were sampled, the algorithm is sometimes forced to jump between different configurations with similar performance parameters. As a result, the maximal chi results are very smooth, but there is some granularity in the optimal system size results.

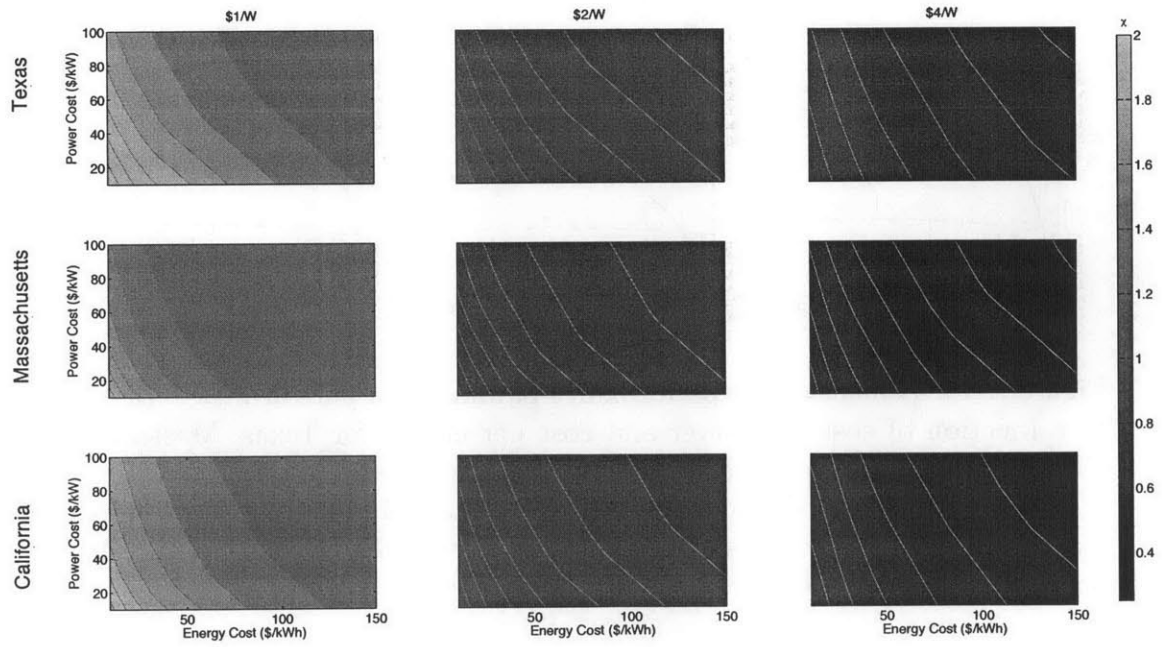

Figure A-20: Optimal performance χ as a function of Energy and Power Cost for hybrid storage wind systems located in Texas, Massachusetts, and California with variable installed cost of generation.

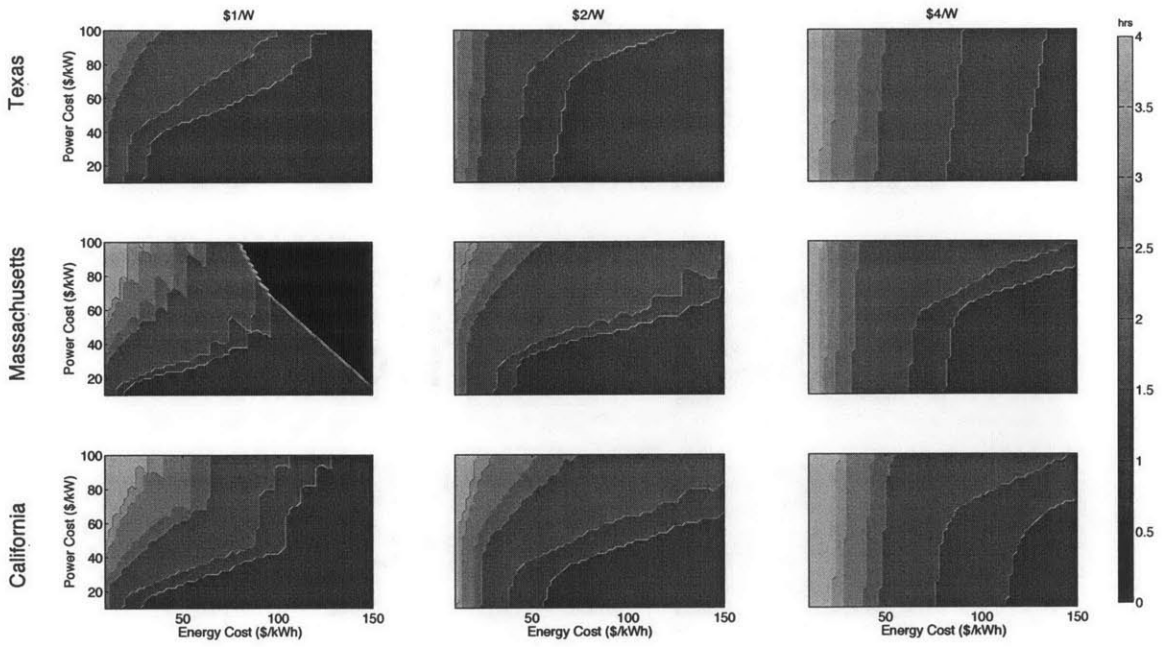

Figure A-21: Optimal storage energy capacity in hours at peak power as a function of Energy and Power Cost for hybrid storage wind systems located in Texas, Massachusetts, and California with variable installed cost of generation.

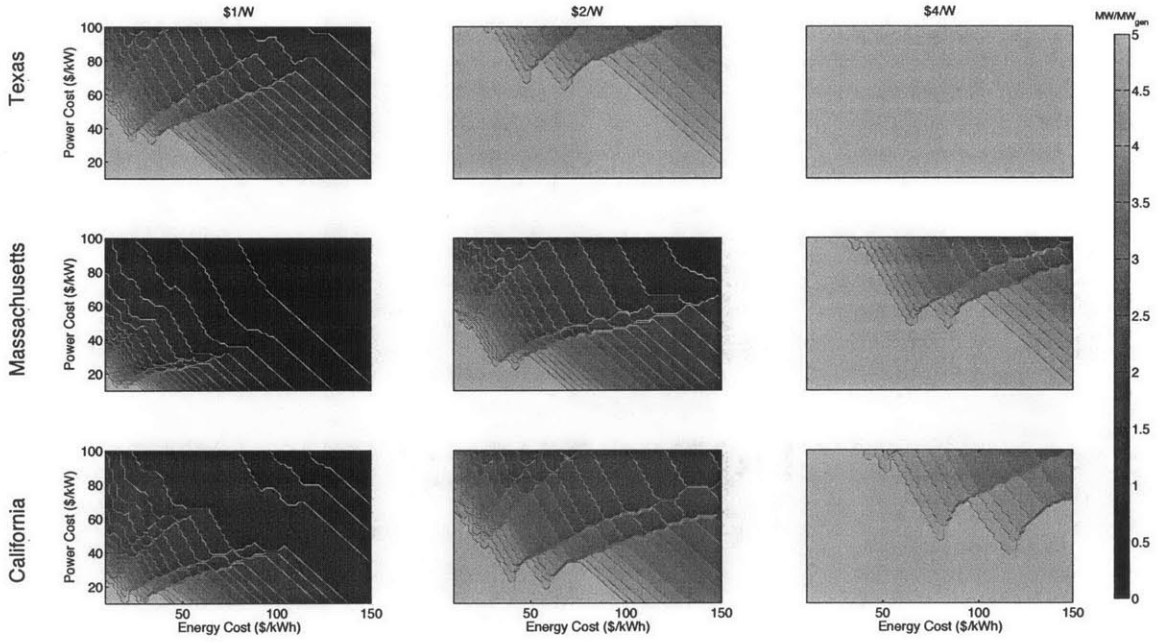

Figure A-22: Optimal storage system power in MW per MW of generation as a function of Energy and Power Cost for hybrid storage wind systems located in Texas, Massachusetts, and California with variable installed cost of generation.

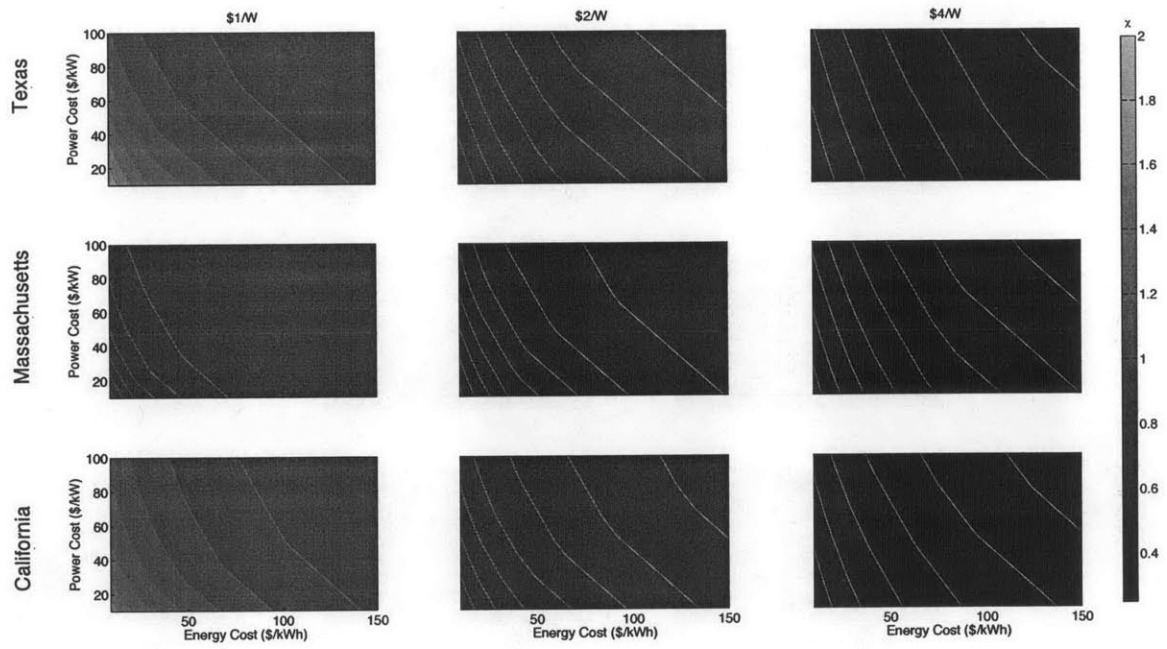

Figure A-23: Optimal performance χ as a function of Energy and Power Cost for hybrid storage solar systems located in Texas, Massachusetts, and California with variable installed cost of generation.

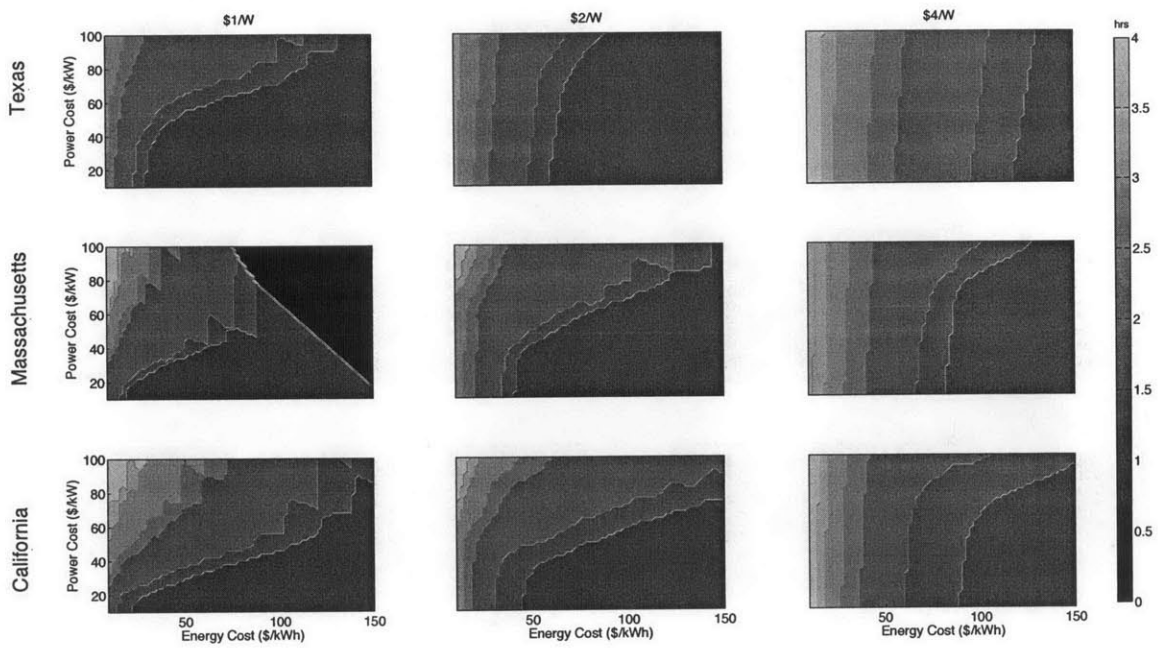

Figure A-24: Optimal storage energy capacity in hours at peak power as a function of Energy and Power Cost for hybrid storage solar systems located in Texas, Massachusetts, and California with variable installed cost of generation.

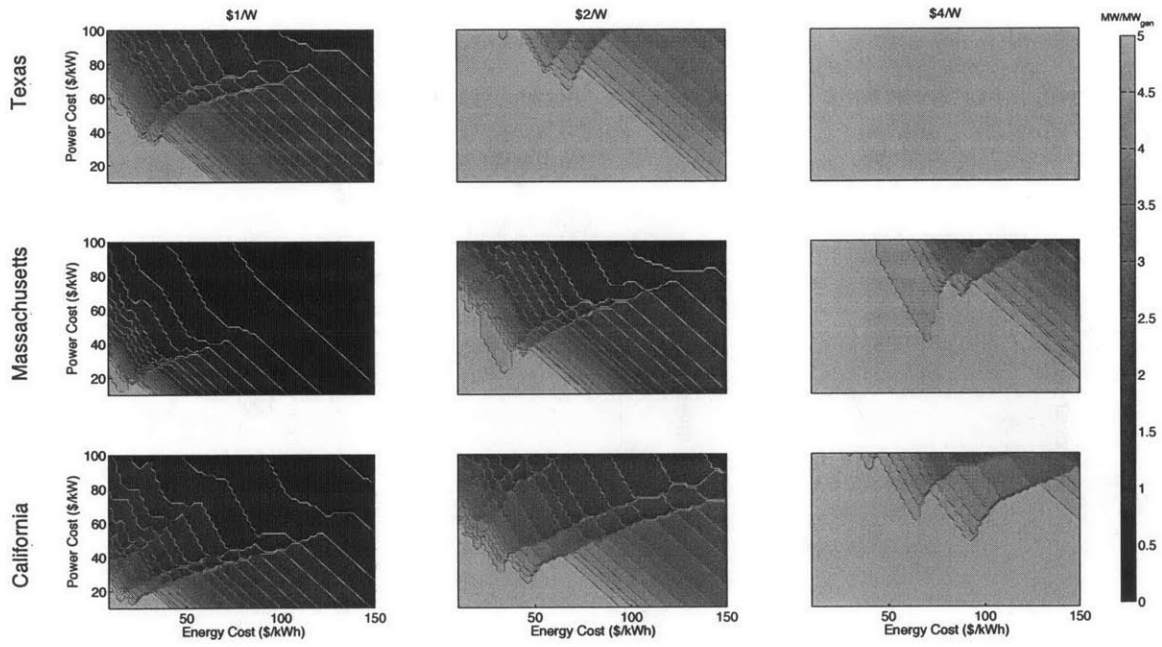

Figure A-25: Optimal storage system power in MW per MW of generation as a function of Energy and Power Cost for hybrid storage solar systems located in Texas, Massachusetts, and California with variable installed cost of generation.

A.4 Tradeoffs in system behavior along an isoperformance line

The previous plots demonstrate how comparable performance can be achieved using storage technologies of very different cost intensities, as long as an appropriately sized system is chosen, but provides no information on exactly what that system size is. Figure A-26 Illustrates how system size and investment in the power- and energy-related components of the system vary along a particular constant performance contour. As energy cost increases and power cost decreases (red to blue), storage power increases and storage energy decreases. However, storage power investment actually decreases, while storage energy investment increases.

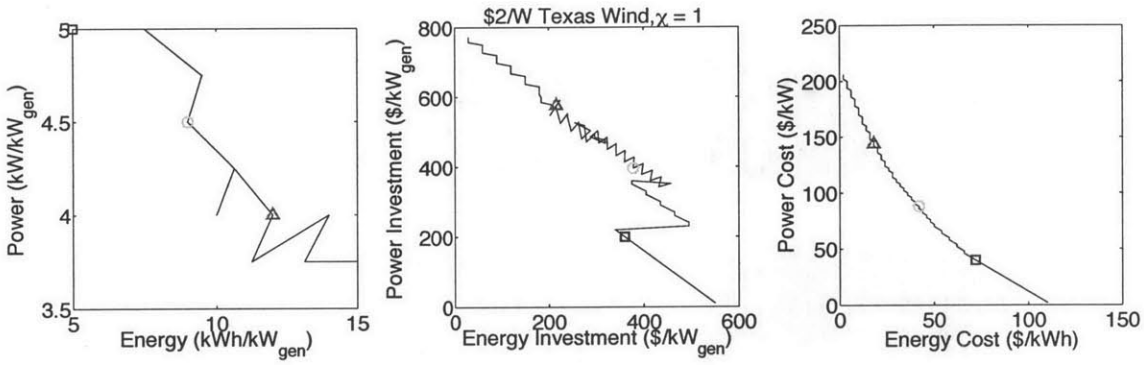

Figure A-26: Optimal storage subsystem size, investment, and cost intensity along an isoperformance curve such that $\chi = 1$ for a hybrid storage wind system located in Texas with a generation cost of \$2/W. The roughness in the plots is due to granularity in the data. The same three points are marked on each plot to indicated directionality. Roughness in the plots is due to granularity in the dataset

Bibliography

[1] Sciences, U S Department of Energy Office of Basic Energy, "Basic research needs for electrical energy storage," tech. rep., 2007.

[2] M. Skyllas-Kazacos, M. H. Chakrabarti, S. A. Hajimolana, F. S. Mjalli, and M. Saleem, "Progress in Flow Battery Research and Development," *Journal of The Electrochemical Society*, vol. 158, no. 8, p. R55, 2011.

[3] K. T. Cho, P. Ridgway, A. Z. Weber, S. Haussener, V. Battaglia, and V. Srinivasan, "High Performance Hydrogen/Bromine Redox Flow Battery for Grid-Scale Energy Storage," *Journal of The Electrochemical Society*, vol. 159, no. 11, pp. A1806–A1815, 2012.

[4] R. Ferrigno, A. D. Stroock, T. D. Clark, M. Mayer, and G. M. Whitesides, "Membraneless Vanadium Redox Fuel Cell Using Laminar Flow," *Journal of the American Chemical Society*, vol. 124, no. 44, pp. 12930–12931, 2002.

[5] E. R. Choban, L. J. Markoski, A. Wieckowski, and P. J. A. Kenis, "Microfluidic fuel cell based on laminar flow," *Journal of Power Sources*, vol. 128, no. 1, pp. 54–60, 2004.

[6] R. S. Jayashree, L. Gancs, E. R. Choban, A. Primak, D. Natarajan, L. J. Markoski, and P. J. A. Kenis, "Air-Breathing Laminar Flow-Based Microfluidic Fuel Cell," *Journal of the American Chemical Society*, vol. 127, no. 48, pp. 16758–16759, 2005.

[7] W. A. Braff and C. R. Buie, "Hydrogen Bromine Laminar Flow Electrochemical Cell for High Power and Efficiency Energy Storage Applications," *ECS Transactions*, vol. 33, no. 39, pp. 179–190, 2011.

[8] S. M. Schoenung and W. V. Hassenzahl, "Long- vs. Short-Term Energy Storage Technologies Analysis A Life-Cycle Cost Study A Study for the DOE Energy Storage Systems Program," tech. rep., 2003.

[9] J. G. Kassakian and R. Schmalensee, "The Future of the Electric Grid," tech. rep., 2011.

[10] D. Rastler, "EPRI - Electricity Energy Storage Technology Options," tech. rep., 2011.

[11] J. Eyer, J. Iannucci, and G. Corey, "Energy Storage Benefits and Market Analysis Handbook, A Study for the DOE Energy Storage Systems Program," *Sandia National Labratories*, 2004.

[12] B. Warshay, S. Minnihan, and M. Feinstein, "Grid Storage Under the Microscope: Using Local Knowledge to Forecase Global Demand," Tech. Rep. LRSGI-R-11-1, 2012.

[13] S. M. Schoenung and J. Eyer, "Benefit/Cost Framework for Evaluating Modular Energy Storage," *Sandia National Laboratories*, pp. 1–40, 2008.

[14] D. R. Rolison and L. F. Nazar, "Electrochemical energy storage to power the 21st century," *MRS Bulletin*, vol. 36, no. 07, pp. 486–493, 2011.

[15] B. Dunn, H. Kamath, and J. M. Tarascon, "Electrical Energy Storage for the Grid: A Battery of Choices," *Science*, vol. 334, no. 6058, pp. 928–935, 2011.

[16] J. Hassoun, S. Panero, P. Reale, and B. Scrosati, "A New, Safe, High-Rate and High-Energy Polymer Lithium-Ion Battery," *Advanced Materials*, vol. 21, pp. 4807–4810, Aug. 2009.

[17] L. Xiaojin, X. Yu, S. Zhigang, and Y. Baolian, "Mass minimization of a discrete regenerative fuel cell (RFC) system for on-board energy storage," *Journal of Power Sources*, vol. 195, no. 15, pp. 4811–4815, 2010.

[18] M. L. Perry, R. M. Darling, and R. Zaffou, "High Power Density Redox Flow Battery Cells," *ECS Transactions*, vol. 53, no. 7, pp. 7–16, 2013.

[19] V. Livshits, A. Ulus, and E. Peled, "High-power H2/Br2 fuel cell," *Electrochemistry Communications*, vol. 8, no. 8, pp. 1358–1362, 2006.

[20] H. J. Stone, "Economic Analysis of Stationary PEM Fuel Cell Systems," tech. rep., 2005.

[21] M. S. Whittingham, "Electrical energy storage and intercalation chemistry," *Science*, vol. 192, no. 4244, pp. 1126–1127, 1976.

[22] Y. Gogotsi and P. Simon, "True Performance Metrics in Electrochemical Energy Storage," *Science*, vol. 334, no. 6058, pp. 917–918, 2011.

[23] J. O. Besenhard and H. P. Fritz, "Cathodic reduction of graphite in organice solutions of alkali and NR4+ salts," *Electroanalytical Chemistry and Interfacial Electrochemistry*, vol. 53, pp. 329–333, 1974.

[24] G. Pistoia, M. Paquali, L. A. De Picciotto, and M. M. Thackeray, "Behaviorof the spinel LiV2O4 as a positive electrode for secondary Li cells," *Solid State Ionics*, vol. 28, pp. 879–885, 1988.

[25] K. Zaghib, A. Guerfi, P. Hovington, A. Vijh, M. Trudeau, A. Mauger, J. B. Goodenough, and C. M. Julien, "Journal of Power Sources," *Journal of Power Sources*, vol. 232, pp. 357–369, June 2013.

[26] B. Kang and G. Ceder, "Battery materials for ultrafast charging and discharging," *Nature*, vol. 457, pp. 190–193, Mar. 2009.

[27] M. Duduta, B. Ho, V. C. Wood, P. Limthongkul, V. E. Brunini, W. C. Carter, and Y.-M. Chiang, "Semi-Solid Lithium Rechargeable Flow Battery," *Advanced Energy Materials*, vol. 1, no. 4, pp. 511–516, 2011.

[28] Y. M. Chiang, "Building a Better Battery," *Science*, vol. 330, no. 6010, pp. 1485–1486, 2010.

[29] Y. Yang, G. Zheng, and Y. Cui, "A membrane-free lithium/polysulfide semi-liquid battery for large-scale energy storage," *Energy & Environmental Science*, vol. 6, no. 5, p. 1552, 2013.

[30] B. M. Wilner, H. A. Frank, E. Findl, and M. G. Klein, "Electrolytically Regenerative Hydrogen/Oxygen Fuel Cell Battery." U.S. Patent Office, 1970.

[31] F. Mitlitsky, B. Myers, and A. Weisberg, "Regenerative fuel cell systems," *Energy & Fuels*, vol. 12, no. 1, pp. 56–71, 1998.

[32] W. A. Amos, "Costs of Storing and Transporting Hydrogen," Tech. Rep. NREL/TP-570-25106, National Renewable Energy Laboratory, 1998.

[33] L. L. Swette, A. B. LaConti, and S. A. McCatty, "Proton-exchange membrane regenerative fuel cells," *Journal of Power Sources*, vol. 47, pp. 343–351, 1994.

[34] G. Chen, D. A. Delafuente, S. Sarangapani, and T. E. Mallouk, "Combinatorial discovery of bifunctional oxygen reduction — water oxidation electrocatalysts for regenerative fuel cells," *Catalysis Today*, vol. 67, pp. 341–355, 2001.

[35] J. Pettersson, B. Ramsey, and D. J. Harrison, "Fabrication of bifunctional membrane electrode assemblies for unitised regenerative polymer electrolyte fuel cells," *Electronics Letters*, vol. 42, no. 25, p. 1444, 2006.

[36] J. Xuan, D. Y. C. Leung, M. K. H. Leung, M. Ni, and H. Wang, "A computational study of bifunctional oxygen electrode in air-breathing reversible microfluidic fuel cells," *International Journal of Hydrogen Energy*, vol. 36, no. 15, pp. 9231–9241, 2011.

[37] M. Skyllas-Kazacos, D. Kasherman, D. R. Hong, and M. Kazacos, "Characteristics and Performance of 1-Kw Unsw Vanadium Redox Battery," *Journal of Power Sources*, vol. 35, no. 4, pp. 399–404, 1991.

[38] H. Kamath, S. Rajagopalan, and M. Zwillenberg, "Vanadium Redox Flow Batteries," Tech. Rep. 1414836, Palo Alto, CA, 2007.

[39] W. Wang, Z. Nie, B. Chen, F. Chen, Q. Luo, X. Wei, G.-G. Xia, M. Skyllas-Kazacos, L. Li, and Z. Yang, "A New Fe/V Redox Flow Battery Using a Sulfuric/Chloric Mixed-Acid Supporting Electrolyte," *Advanced Energy Materials*, vol. 2, no. 4, pp. 487–493, 2012.

[40] S. Kim, E. Thomsen, G. Xia, Z. Nie, J. Bao, K. Recknagle, W. Wang, V. Viswanathan, Q. Luo, X. Wei, A. Crawford, G. Coffey, G. Maupin, and V. Sprenkle, "1 kW/1 kWh advanced vanadium redox flow battery utilizing mixed acid electrolytes," *Journal of Power Sources*, vol. 237, no. c, pp. 300–309, 2013.

[41] Z. Yang, J. Zhang, M. C. W. Kintner-Meyer, X. Lu, D. Choi, J. P. Lemmon, and J. Liu, "Electrochemical Energy Storage for Green Grid," *Chemical Reviews*, vol. 111, no. 5, pp. 3577–3613, 2011.

[42] H. Vafiadis and M. Skyllas-Kazacos, "Evaluation of membranes for the novel vanadium bromine redox flow cell," *Journal of Membrane Science*, vol. 279, no. 1-2, pp. 394–402, 2006.

[43] R. Zaffou, W. N. Li, and M. L. Perry, "Vanadium Redox Flow Batteries for Electrical Energy Storage: Challenges and Opportunities," in *Polymers for energy storage and delivery: polyelectrolytes for batteries and fuel cells*, pp. 107–127, Washington, DC: American Chemical Society, 2012.

[44] C. J. Barnhart and S. M. Benson, "On the importance of reducing the energetic and material demands of electrical energy storage," *Energy & Environmental Science*, 2013.

[45] R. S. Yeo and D.-T. Chin, "Hydrogen-Bromine Cell for Energy-Storage Applications," *Journal of The Electrochemical Society*, vol. 127, no. 3, pp. 549–555, 1980.

[46] G. H. Schuetz and P. J. Fiebelmann, "Electrolysis of hydrobromic acid," *International Journal of Hydrogen Energy*, vol. 5, no. 3, pp. 305–316, 1980.

[47] W. Cooper and R. Parsons, "Kinetics of Bromine/Bromide Electrode on Platinum in Aqueous Sulphuric Acid," *Transactions of the Faraday Society*, vol. 66, no. 571, pp. 1698–1712, 1970.

[48] S. Ferro and A. De Battisti, "The bromine electrode. Part I: Adsorption phenomena at polycrystalline platinum electrodes," *Journal of Applied Electrochemistry*, vol. 34, no. 10, pp. 981–987, 2004.

[49] S. Ferro, C. Orsan, and A. De Battisti, "The bromine electrode Part II: reaction kinetics at polycrystalline Pt," *Journal of Applied Electrochemistry*, vol. 35, no. 3, pp. 273–278, 2005.

[50] U S Geological Survey, "Mineral Commodity Summaries 2011," Tech. Rep. 198, U.S. Geological Survey, 2011.

[51] G. G. Barna, S. N. Frank, T. H. Teherani, and L. D. Weedon, "Lifetime Studies in H2/Br2 Fuel-Cells," *Journal of The Electrochemical Society*, vol. 131, no. 9, pp. 1973–1980, 1984.

[52] R. F. Savinell and S. D. Fritts, "Theoretical Performance of a Hydrogen Bromine Rechargeable SPE Fuel-Cell," *Journal of Power Sources*, vol. 22, pp. 423–440, 1988.

[53] R. S. Yeo and J. McBreen, "Transport Properties of Nafion Membranes in Electrochemically Regenerative Hydrogen-Halogen Cells," *Journal of The Electrochemical Society*, vol. 126, no. 10, pp. 1682–1687, 1979.

[54] A. Kusoglu, K. T. Cho, R. A. Prato, and A. Z. Weber, "Solid State Ionics," *Solid State Ionics*, vol. 254, p. in press, 2014.

[55] S. D. Fritts and R. F. Savinell, "Simulation Studies on the Performance of the Hydrogen Electrode Bonded to Proton-Exchange Membranes in the Hydrogen-Bromine Fuel-Cell," *Journal of Power Sources*, vol. 28, no. 3, pp. 301–315, 1989.

[56] H. Kreutzer, V. Yarlagadda, and T. V. Nguyen, "Performance Evaluation of a Regenerative Hydrogen-Bromine Fuel Cell," *Journal of The Electrochemical Society*, vol. 159, no. 7, pp. F331–F337, 2012.

[57] Tiax, LLC, "Cost Analysis of Fuel Cell Systems for Transportation," Tech. Rep. DE-SCO2-98EE50526, 2004.

[58] L. Li, S. Kim, G. Xai, W. Wang, and Z. Yang, "Advanced Redox Flow Batteries for Stationary Electrical Energy Storage," Tech. Rep. PNNL-21174, Pacific Northwest National Lab, Mar. 2012.

[59] P. J. A. Kenis, R. Ismagilov, and G. M. Whitesides, "Microfabrication inside capillaries using multiphase laminar flow patterning," *Science*, vol. 285, no. 5424, pp. 83–85, 1999.

[60] C. N. Baroud, F. Okkels, L. Ménétrier, and P. Tabeling, "Reaction-diffusion dynamics: confrontation between theory and experiment in a microfluidic reactor.," *Physical Review E*, vol. 67, no. 6, p. 060104, 2003.

[61] E. R. Choban, P. Waszczuk, and P. J. A. Kenis, "Characterization of Limiting Factors in Laminar Flow-Based Membraneless Microfuel Cells," *Electrochemical and Solid-State Letters*, vol. 8, no. 7, p. A348, 2005.

[62] A. Bazylak, D. Sinton, and N. Djilali, "Improved fuel utilization in microfluidic fuel cells: A computational study," *Journal of Power Sources*, vol. 143, no. 1-2, pp. 57–66, 2005.

[63] M.-H. Chang, F. Chen, and N.-S. Fang, "Analysis of membraneless fuel cell using laminar flow in a Y-shaped microchannel," *Journal of Power Sources*, vol. 159, no. 2, pp. 810–816, 2006.

[64] W. Chen and F. Chen, "Theoretical approaches to studying the single and simultaneous reactions in laminar flow-based membraneless fuel cells," *Journal of Power Sources*, vol. 162, no. 2, pp. 1137–1146, 2006.

[65] M. H. Sun, G. Velve Casquillas, S. S. Guo, J. Shi, H. Ji, Q. Ouyang, and Y. Chen, "Characterization of microfluidic fuel cell based on multiple laminar flow," *Microelectronic Engineering*, vol. 84, no. 5-8, pp. 1182–1185, 2007.

[66] J. Xuan, M. K. H. Leung, D. Y. C. Leung, M. Ni, and H. Wang, "Hydrodynamic focusing in microfluidic membraneless fuel cells: Breaking the trade-off between fuel utilization and current density," *International Journal of Hydrogen Energy*, vol. 36, pp. 11075–11084, Aug. 2011.

[67] C. O. Colpan, A. Fung, and F. Hamdullahpur, "2D modeling of a flowing-electrolyte direct methanol fuel cell," *Journal of Power Sources*, vol. 209, pp. 301–311, 2012.

[68] J. Xuan, D. Y. C. Leung, H. Wang, M. K. H. Leung, B. Wang, and M. Ni, "Air-breathing membraneless laminar flow-based fuel cells: Do they breathe enough oxygen?," *Applied Energy*, vol. 104, pp. 400–407, 2013.

[69] J. L. Cohen, D. A. Westly, A. Pechenik, and H. D. Abruña, "Fabrication and preliminary testing of a planar membraneless microchannel fuel cell," *Journal of Power Sources*, vol. 139, no. 1-2, pp. 96–105, 2005.

[70] J. L. Cohen, D. J. Volpe, D. A. Westly, A. Pechenik, and H. D. Abruña, "A Dual Electrolyte H 2/O 2Planar Membraneless Microchannel Fuel Cell System with Open Circuit Potentials in Excess of 1.4 V," *Langmuir*, vol. 21, no. 8, pp. 3544–3550, 2005.

[71] E. R. Choban, J. S. Spendelow, L. Gancs, A. Wieckowski, and P. J. A. Kenis, "Membraneless laminar flow-based micro fuel cells operating in alkaline, acidic, and acidic/alkaline media," *Electrochimica Acta*, vol. 50, no. 27, pp. 5390–5398, 2005.

[72] L. J. Markoski, P. Waszczuk, P. J. A. Kenis, and E. R. Choban, "Emulsions for fuel cells." United States Patent Application, 2003.

[73] S. Ha, Z. Dunbar, and R. I. Masel, "Characterization of a high performing passive direct formic acid fuel cell," *Journal of Power Sources*, vol. 158, no. 1, pp. 129–136, 2006.

[74] S. M. Mitrovski and R. G. Nuzzo, "A passive microfluidic hydrogen–air fuel cell with exceptional stability and high performance," *Lab on a Chip*, vol. 6, no. 3, p. 353, 2006.

[75] R. S. Jayashree, D. Egas, J. S. Spendelow, D. Natarajan, L. J. Markoski, and P. J. A. Kenis, "Air-Breathing Laminar Flow-Based Direct Methanol Fuel Cell with Alkaline Electrolyte," *Electrochemical and Solid-State Letters*, vol. 9, no. 5, p. A252, 2006.

[76] R. S. Jayashree, M. Mitchell, D. Natarajan, L. J. Markoski, and P. J. A. Kenis, "Microfluidic Hydrogen Fuel Cell with a Liquid Electrolyte," *Langmuir*, vol. 23, no. 13, pp. 6871–6874, 2007.

[77] F. R. Brushett, W.-P. Zhou, R. S. Jayashree, and P. J. A. Kenis, "Alkaline Microfluidic Hydrogen-Oxygen Fuel Cell as a Cathode Characterization Platform," *Journal of The Electrochemical Society*, vol. 156, no. 5, p. B565, 2009.

[78] F. R. Brushett, R. S. Jayashree, W.-P. Zhou, and P. J. A. Kenis, "Investigation of fuel and media flexible laminar flow-based fuel cells," *Electrochimica Acta*, vol. 54, no. 27, pp. 7099–7105, 2009.

[79] R. S. Jayashree, S. K. Yoon, F. R. Brushett, P. O. Lopez-Montesinos, D. Natarajan, L. J. Markoski, and P. J. A. Kenis, "On the performance of membraneless laminar flow-based fuel cells," *Journal of Power Sources*, vol. 195, no. 11, pp. 3569–3578, 2010.

[80] M. Gowdhamamoorthi, A. arun, S. kiruthika, and B. muthukumaran, "Enhanced Performance of Membraneless Sodium Percarbonate Fuel Cells," *Journal of Materials*, vol. 2013, no. 4, pp. 1–7, 2013.

[81] D. T. Whipple, R. S. Jayashree, D. Egas, N. Alonso-Vante, and P. J. A. Kenis, "Ruthenium cluster-like chalcogenide as a methanol tolerant cathode catalyst in air-breathing laminar flow fuel cells," *Electrochimica Acta*, vol. 54, no. 18, pp. 4384–4388, 2009.

[82] F. R. Brushett, M. S. Thorum, N. S. Lioutas, M. S. Naughton, C. Tornow, H.-R. M. Jhong, A. A. Gewirth, and P. J. A. Kenis, "A Carbon-Supported Copper Complex of 3,5-Diamino-1,2,4-triazole as a Cathode Catalyst for Alkaline Fuel Cell Applications," *Journal of the American Chemical Society*, vol. 132, no. 35, pp. 12185–12187, 2010.

[83] F. R. Brushett, M. S. Naughton, J. W. D. Ng, L. Yin, and P. J. A. Kenis, "Analysis of Pt/C electrode performance in a flowing-electrolyte alkaline fuel cell," *International Journal of Hydrogen Energy*, vol. 37, no. 3, pp. 2559–2570, 2012.

[84] F. R. Brushett, H. T. Duong, J. W. D. Ng, R. L. Behrens, A. Wieckowski, and P. J. A. Kenis, "Investigation of Pt, Pt[sub 3]Co, and Pt[sub 3]Co/Mo Cathodes for the ORR in a Microfluidic H[sub 2]/O[sub 2] Fuel Cell," *Journal of The Electrochemical Society*, vol. 157, no. 6, p. B837, 2010.

[85] M. S. Naughton, F. R. Brushett, and P. J. A. Kenis, "Carbonate resilience of flowing electrolyte-based alkaline fuel cells," *Journal of Power Sources*, vol. 196, no. 4, pp. 1762–1768, 2011.

[86] E. Kjeang, J. McKechnie, D. Sinton, and N. Djilali, "Planar and three-dimensional microfluidic fuel cell architectures based on graphite rod electrodes," *Journal of Power Sources*, vol. 168, no. 2, pp. 379–390, 2007.

[87] E. Kjeang, R. Michel, D. A. Harrington, N. Djilali, and D. Sinton, "A Microfluidic Fuel Cell with Flow-Through Porous Electrodes," *Journal of the American Chemical Society*, vol. 130, no. 12, pp. 4000–4006, 2008.

[88] E. Kjeang, R. Michel, D. A. Harrington, D. Sinton, and N. Djilali, "An alkaline microfluidic fuel cell based on formate and hypochlorite bleach," *Electrochimica Acta*, vol. 54, no. 2, pp. 698–705, 2008.

[89] S. A. Mousavi Shaegh, N.-T. Nguyen, and S. H. Chan, "An air-breathing microfluidic formic acid fuel cell with a porous planar anode: experimental and numerical investigations," *Journal of Micromechanics and Microengineering*, vol. 20, no. 10, p. 105008, 2010.

[90] S. A. Mousavi Shaegh, N.-T. Nguyen, S. H. Chan, and W. Zhou, "Air-breathing membraneless laminar flow-based fuel cell with flow-through anode," *International Journal of Hydrogen Energy*, vol. 37, no. 4, pp. 3466–3476, 2012.

[91] J. W. Lee, M.-A. Goulet, and E. Kjeang, "Microfluidic redox battery.," *Lab on a Chip*, vol. 13, no. 13, pp. 2504–2507, 2013.

[92] K. S. Salloum, J. R. Hayes, C. A. Friesen, and J. D. Posner, "Sequential flow membraneless microfluidic fuel cell with porous electrodes," *Journal of Power Sources*, vol. 180, no. 1, pp. 243–252, 2008.

[93] J. R. Hayes, A. M. Engstrom, and C. Friesen, "Orthogonal flow membraneless fuel cell," *Journal of Power Sources*, vol. 183, no. 1, pp. 257–259, 2008.

[94] K. S. Salloum and J. D. Posner, "Counter flow membraneless microfluidic fuel cell," *Journal of Power Sources*, vol. 195, no. 19, pp. 6941–6944, 2010.

[95] S. Moghaddam, E. Pengwang, R. I. Masel, and M. Shannon, "An enhanced microfluidic control system for improving power density of a hydride-based micro fuel cell," *Journal of Power Sources*, vol. 195, no. 7, pp. 1866–1871, 2010.

[96] K. S. Salloum and J. D. Posner, "A membraneless microfluidic fuel cell stack," *Journal of Power Sources*, vol. 196, no. 3, pp. 1229–1234, 2011.

[97] A. D. Stroock, S. K. W. Dertinger, A. Ajdari, I. Mezic, H. A. Stone, and G. M. Whitesides, "Chaotic mixer for microchannels.," *Science*, vol. 295, no. 5555, pp. 647–651, 2002.

[98] N. Da Mota, D. A. Finkelstein, J. D. Kirtland, C. A. Rodriguez, A. D. Stroock, and H. D. Abruña, "Membraneless, room-temperature, direct borohydride/cerium fuel cell with power density of over 0.25 W/cm2.," *Journal of the American Chemical Society*, vol. 134, no. 14, pp. 6076–6079, 2012.

[99] A. S. Hollinger, R. J. Maloney, R. S. Jayashree, D. Natarajan, L. J. Markoski, and P. J. A. Kenis, "Nanoporous separator and low fuel concentration to minimize crossover in direct methanol laminar flow fuel cells," *Journal of Power Sources*, vol. 195, no. 11, pp. 3523–3528, 2010.

[100] S. Moore, D. Sinton, and D. Erickson, "A plate-frame flow-through microfluidic fuel cell stack," *Journal of Power Sources*, vol. 196, no. 22, pp. 9481–9487, 2011.

[101] A. Li, S. H. Chan, and N.-T. Nguyen, "A laser-micromachined polymeric membraneless fuel cell," *Journal of Micromechanics and Microengineering*, vol. 17, no. 6, pp. 1107–1113, 2007.

[102] J. W. Lee and E. Kjeang, "Chip-embedded thin film current collector for microfluidic fuel cells," *International Journal of Hydrogen Energy*, vol. 37, pp. 9359–9367, 2012.

[103] B. Ho, "Planar Multiplexing of Microfluidic Fuel Cells," *Journal of Fluids Engineering*, vol. 135, p. 021304, Feb. 2013.

[104] S. A. Mousavi Shaegh, N.-T. Nguyen, and S. H. Chan, "Air-breathing microfluidic fuel cell with fuel reservoir," *Journal of Power Sources*, vol. 209, pp. 312–317, 2012.

[105] A. S. Hollinger and P. J. A. Kenis, "Manufacturing all-polymer laminar flow-based fuel cells," *Journal of Power Sources*, vol. 240, no. C, pp. 486–493, 2013.

[106] J. W. Lee and E. Kjeang, "Journal of Power Sources," *Journal of Power Sources*, vol. 242, no. C, pp. 472–477, 2013.

[107] J. Lee, K. G. Lim, G. T. R. Palmore, and A. Tripathi, "Optimization of Microfluidic Fuel Cells Using Transport Principles," *Analytical Chemistry*, vol. 79, no. 19, pp. 7301–7307, 2007.

[108] A. E. Khabbazi, A. J. Richards, and M. Hoorfar, "Numerical study of the effect of the channel and electrode geometry on the performance of microfluidic fuel cells," *Journal of Power Sources*, vol. 195, no. 24, pp. 8141–8151, 2010.

[109] D. Krishnamurthy, E. O. Johansson, J. W. Lee, and E. Kjeang, "Computational modeling of microfluidic fuel cells with flow-through porous electrodes," *Journal of Power Sources*, vol. 196, no. 23, pp. 10019–10031, 2011.

[110] I. B. Sprague and P. Dutta, "Role of the diffuse layer in acidic and alkaline fuel cells," *Electrochimica Acta*, vol. 56, no. 12, pp. 4518–4525, 2011.

[111] I. B. Sprague and P. Dutta, "Performance improvement of micro-fuel cell by manipulating the charged diffuse layer," *Applied Physics Letters*, vol. 101, p. 113903, 2012.

[112] I. B. Sprague, D. Byun, and P. Dutta, "Effects of reactant crossover and electrode dimensions on the performance of a microfluidic based laminar flow fuel cell," *Electrochimica Acta*, vol. 55, no. 28, pp. 8579–8589, 2010.

[113] I. B. Sprague and P. Dutta, "Modeling of Diffuse Charge Effects in a Microfluidic Based Laminar Flow Fuel Cell," *Numerical Heat Transfer, Part A: Applications*, vol. 59, pp. 1–27, Jan. 2011.

[114] I. B. Sprague and P. Dutta, "Improved kinetics from ion advection through overlapping electric double layers in nano-porous electrodes," *Electrochimica Acta*, vol. 91, pp. 20–29, 2013.

[115] I. B. Sprague and P. Dutta, "Depth Averaged Analytic Solution for a Laminar Flow Fuel Cell with Electric Double Layer Effects," *SIAM Journal on Applied Mathematics*, vol. 72, no. 4, pp. 1149–1168, 2012.

[116] M. R. Thorson, F. R. Brushett, C. J. Timberg, and P. J. A. Kenis, "Design rules for electrode arrangement in an air-breathing alkaline direct methanol laminar flow fuel cell," *Journal of Power Sources*, vol. 218, no. C, pp. 28–33, 2012.

[117] T. A. Zawodzinski, C. Derouin, S. Radzinski, R. J. Sherman, V. T. Smith, T. E. Springer, and S. Gottesfeld, "Water-Uptake by and Transport Through Nafion(R) 117 Membranes," *Journal of The Electrochemical Society*, vol. 140, no. 4, pp. 1041–1047, 1993.

[118] J. Rugolo and M. J. Aziz, "Electricity storage for intermittent renewable sources," *Energy & Environmental Science*, vol. 5, no. 5, pp. 7151–7160, 2012.

[119] G. L. Soloveichik, "Battery Technologies for Large-Scale Stationary Energy Storage," *Annual Review of Chemical and Biomolecular Engineering*, vol. 2, no. 1, pp. 503–527, 2011.

[120] E. Hittinger, J. F. Whitacre, and J. Apt, "What properties of grid energy storage are most valuable?," *Journal of Power Sources*, vol. 206, pp. 436–449, 2012.

[121] A. Z. Weber, M. M. Mench, J. P. Meyers, P. N. Ross, J. T. Gostick, and Q. Liu, "Redox flow batteries: a review," *Journal of Applied Electrochemistry*, vol. 41, no. 10, pp. 1137–1164, 2011.

[122] C. Ponce de León, A. Frías-Ferrer, J. González-García, D. A. Szánto, and F. C. Walsh, "Redox flow cells for energy conversion," *Journal of Power Sources*, vol. 160, no. 1, pp. 716–732, 2006.

[123] K. W. Knehr, E. Agar, C. R. Dennison, A. R. Kalidindi, and E. C. Kumbur, "A Transient Vanadium Flow Battery Model Incorporating Vanadium Crossover and Water Transport through the Membrane," *Journal of The Electrochemical Society*, vol. 159, no. 9, pp. A1446–A1459, 2012.

[124] Q. Liu, A. A. Shinkle, Y. Li, C. W. Monroe, L. T. Thompson, and A. E. S. Sleightholme, "Non-aqueous chromium acetylacetonate electrolyte for redox flow batteries," *Electrochemistry Communications*, vol. 12, no. 11, pp. 1634–1637, 2010.

[125] J. A. Kosek and A. B. LaConti, "Advanced Hydrogen Electrode for a Hydrogen Bromine Battery," *Journal of Power Sources*, vol. 22, pp. 293–300, 1988.

[126] M. Goor-Dar, N. Travitsky, and E. Peled, "Study of hydrogen redox reactions on platinum nanoparticles in concentrated HBr solutions," *Journal of Power Sources*, vol. 197, pp. 111–115, 2012.

[127] J. K. Clark, S. J. Paddison, M. Eikerling, M. Dupuis, and T. A. Zawodzinski, "A comparative ab initio study of the primary hydration and proton dissociation of various imide and sulfonic acid ionomers.," *The Journal of Physical Chemistry A*, vol. 116, no. 7, pp. 1801–1813, 2012.

[128] K.-D. Kreuer, S. J. Paddison, E. Spohr, and M. Schuster, "Transport in Proton Conductors for Fuel-Cell Applications: Simulations, Elementary Reactions, and Phenomenology," *Chemical Reviews*, vol. 104, no. 10, pp. 4637–4678, 2004.

[129] E. Kjeang, B. Proctor, A. G. Brolo, D. A. Harrington, N. Djilali, and D. Sinton, "High-performance microfluidic vanadium redox fuel cell," *Electrochimica Acta*, vol. 52, no. 15, pp. 4942–4946, 2007.

[130] W. A. Braff, C. R. Buie, and M. Z. Bazant, "Numerical and Analytic Modeling of a Membraneless Hydrogen Bromine Laminar Flow Battery," *ECS Transactions*, vol. 53, no. 7, pp. 51–62, 2013.

[131] D. R. Lide, *Handbook of Chemistry and Physics*. CRC Press, 93rd ed., 2012.

[132] A. Lévêque, *Les Lois de la Transmission de Chaleur par Convection*. Annales des Mines ou Recueil de Mémoires sur l'Exploitation des Mines et sur les Sciences et les Arts qui s'y Rattachent, 1928.

[133] R. F. Probstein, *Physicochemical Hydrodynamics*. Wiley-Interscience, 1989.

[134] V. Haddadi-Asl, M. Kazacos, and M. Skyllas-Kazacos, "Conductive carbon-polypropylene composite electrodesfor vanadium redox battery," *Journal of Applied Electrochemistry*, vol. 25, pp. 29–33, 1995.

[135] M. Wesselmark, B. Wickman, C. Lagergren, and G. Lindbergh, "Hydrogen oxidation reaction on thin platinum electrodes in the polymer electrolyte fuel cell," *Electrochemistry Communications*, vol. 12, no. 11, pp. 1585–1588, 2010.

[136] R.-F. Liu, N. Singh, A. Ivanovskaya, A. Calgaro, H. Metiu, and E. McFarland, "Theory Guided Design of Electrocatalysts for the H2-Br2 Flow Battery System," *221st ECS Meeting*, pp. 1–1, 2012.

[137] R. F. Ismagilov, A. D. Stroock, P. J. A. Kenis, G. Whitesides, and H. A. Stone, "Experimental and theoretical scaling laws for transverse diffusive broadening in two-phase laminar flows in microchannels," *Applied Physics Letters*, vol. 76, no. 17, p. 2376, 2000.

[138] S. A. Mousavi Shaegh, N.-T. Nguyen, and S. H. Chan, "A review on membraneless laminar flow-based fuel cells," *International Journal of Hydrogen Energy*, vol. 36, no. 9, pp. 5675–5694, 2011.

[139] E. Kjeang, N. Djilali, and D. Sinton, "Advances in Microfluidic Fuel Cells," in *Advances in microfluidic fuel cells*, pp. 99–139, Elsevier, 2009.

[140] D. A. Finkelstein, J. D. Kirtland, N. D. Mota, A. D. Stroock, and H. D. Abruña, "Alternative Oxidants for High-Power Fuel Cells Studied by Rotating Disk Electrode (RDE) Voltammetry at Pt, Au, and Glassy Carbon Electrodes," *The Journal of Physical Chemistry C*, vol. 115, no. 13, pp. 6073–6084, 2011.

[141] P. Tabeling, M. Chabert, A. Dodge, C. Jullien, and F. Okkels, "Chaotic mixing in cross-channel micromixers.," *Philosophical transactions. Series A, Mathematical, physical, and engineering sciences*, vol. 362, no. 1818, pp. 987–1000, 2004.

[142] V. Edwards and J. Newman, "Design of thin-gap channel flow cells," *Journal of The Electrochemical Society*, vol. 134, no. 5, pp. 1181–1186, 1987.

[143] J. Newman and K. E. Thomas-Alyea, *Electrochemical Systems*. John Wiley, 3 ed., 2004.

[144] J. Jiménez, "The growth of a mixing layer in a laminar channel," *Journal of Fluid Mechanics*, vol. 535, pp. 245–254, 2005.

[145] A. N. Colli and J. M. Bisang, "Validation of Theory with Experiments for Local Mass Transfer at Parallel Plate Electrodes under Laminar Flow Conditions," *Journal of The Electrochemical Society*, vol. 160, no. 1, pp. E5–E11, 2012.

[146] W. A. Braff, M. Z. Bazant, and C. R. Buie, "Membrane-less hydrogen bromine flow battery," *Nature Communications*, vol. 4, p. 2346, 2013.

[147] T. S. Zhao, K.-D. Kreuer, and T. V. Nguyen, *Advances in Fuel Cells*. Oxford, UK: Elsevier, Ltd, 2007.

[148] A. A. Kulikovsky, *Analytical Modeling of Fuel Cells*. Amsterdam, The Netherlands: Elsevier, 1st ed., 2010.

[149] M. Z. Bazant, "10.626 Electrochemical Energy Systems," 2011.

[150] P. M. Biesheuvel, M. van Soestbergen, and M. Z. Bazant, "Imposed currents in galvanic cells," *Electrochimica Acta*, vol. 54, no. 21, pp. 4857–4871, 2009.

[151] M. Z. Bazant, "Theory of Chemical Kinetics and Charge Transfer based on Nonequilibrium Thermodynamics," *Accounts of Chemical Research*, vol. 46, no. 5, pp. 1144–1160, 2013.

[152] R. W. Ramette and D. A. Palmer, "Thermodynamics of Tri- and Pentabromide Anions in Aqueous Solution," *Journal of Solution Chemistry*, vol. 15, no. 5, pp. 387–395, 1986.

[153] P. K. Adanuvor, R. E. White, and S. E. Lorimer, "The Effect of the Tribromide Complex Reaction on the Oxidation/Reduction Current of the Br2/Br Electrode," *Journal of The Electrochemical Society*, vol. 134, no. 6, pp. 1450–1454, 1987.

[154] A. J. Bard, R. Parsons, and J. Jordan, *Standard Potentials in Aqueous Solution.* New York, NY: Marcel Dekker, Inc., 1985.

[155] M. Z. Bazant, "Conformal mapping of some non-harmonic functions in transport theory," *Proceedings of the Royal Society A: Mathematical, Physical and Engineering Sciences*, vol. 460, no. 2045, pp. 1433–1452, 2004.

[156] J. Choi, D. Margetis, T. M. Squires, and M. Z. Bazant, "Steady advection–diffusion around finite absorbers in two-dimensional potential flows," *Journal of Fluid Mechanics*, vol. 536, pp. 155–184, 2005.

[157] L. M. Cummings, Y. E. Hohlov, S. D. Howison, and K. Kornev, "Two-dimensional solidification and melting in potential flows," *Journal of Fluid Mechanics*, vol. 378, pp. 1–18, 1999.

[158] M. Z. Bazant, J. Choi, and B. Davidovitch, "Dynamics of conformal maps for a class of non-Laplacian growth phenomena," *Physical Review Letters*, vol. 91, no. 4, p. 045503, 2003.

[159] W. M. Deen, "Analysis of Transport Phenomena," Oxford University Press, 2012.

[160] A. Lévêque, "The laws of convective heat transfer," *Annales des Mines*, vol. 13, p. 284, 1928.

[161] A. A. Sonin and R. F. Probstein, "A Hydrodynamic Theory of Desalination by Electrodialysis," *Desalination*, vol. 5, no. 3, pp. 293–329, 1968.

[162] D. S. Deng, E. V. Dydek, J. H. Han, S. Schlumpberger, A. Mani, and M. Z. Bazant, "Overlimiting current and shock electrodialysis in porous media," *submitted*, 2013.

[163] M. Chatenet, M. B. Molina-Concha, N. El-Kissi, G. Parrour, and J. P. Diard, "Direct rotating ring-disk measurement of the sodium borohydride diffusion coefficient in sodium hydroxide solutions," *Electrochimica Acta*, vol. 54, pp. 4426–4435, July 2009.

[164] V. E. Brunini, Y.-M. Chiang, and W. C. Carter, "Modeling the hydrodynamic and electrochemical efficiency of semi-solid flow batteries," *Electrochimica Acta*, vol. 69, pp. 301–307, 2012.

[165] V. Presser, C. R. Dennison, J. Campos, K. W. Knehr, E. C. Kumbur, and Y. Gogotsi, "The Electrochemical Flow Capacitor: A New Concept for Rapid Energy Storage and Recovery," *Advanced Energy Materials*, vol. 2, no. 7, pp. 895–902, 2012.

[166] S.-i. Jeon, H.-r. Park, J.-g. Yeo, S. Yang, C. H. Cho, M. H. Han, and D. K. Kim, "Desalination via a new membrane capacitive deionization process utilizing flow-electrodes," *Energy & Environmental Science*, vol. 6, no. 5, pp. 1471–1475, 2013.

[167] Z. Nie, C. A. Nijhuis, J. Gong, X. Chen, A. Kumachev, A. W. Martinez, M. Narovlyansky, and G. M. Whitesides, "Electrochemical sensing in paper-based microfluidic devices," *Lab on a Chip*, vol. 10, no. 4, p. 477, 2010.

[168] S. Eyal and S. R. Quake, "Velocity-independent microfluidic flow cytometry," *Electrophoresis*, vol. 23, pp. 2653–2657, 2002.

[169] W. R. Dean, "Note on the motion of fluid in a curved pipe," *Philosophical Magazine*, vol. 4, no. 20, pp. 208–223, 1927.

[170] S. A. Berger, L. Talbot, and L. S. Yao, "Flow in curved pipes," *Annual Review of Fluid Mechanics*, vol. 15, pp. 461–512, 1983.

[171] D. Di Carlo, "Inertial microfluidics.," *Lab on a Chip*, vol. 9, no. 21, pp. 3038–3046, 2009.

[172] X. Mao, A. A. Nawaz, S.-C. S. Lin, M. I. Lapsley, Y. Zhao, J. P. McCoy, W. S. El-Deiry, and T. J. Huang, "An integrated, multiparametric flow cytometry chip using "microfluidic drifting" based three-dimensional hydrodynamic focusing.," *Biomicrofluidics*, vol. 6, no. 2, pp. 24113–241139, 2012.

[173] M. Norouzi and N. Biglari, "An analytical solution for Dean flow in curved ducts with rectangular cross section," *Physics of Fluids*, vol. 25, no. 5, p. 053602, 2013.

[174] L. Guglielmini, R. Rusconi, S. Lecuyer, and H. A. Stone, "Three-dimensional features in low-Reynolds-number confined corner flows," *Journal of Fluid Mechanics*, vol. 668, pp. 33–57, 2010.

[175] D. T. Chiu, "Cellular manipulations in microvortices," *Analytical and Bioanalytical Chemistry*, vol. 387, no. 1, pp. 17–20, 2006.

[176] A. P. Sudarsan and V. M. Ugaz, "Multivortex micromixing.," *Proceedings of the National Academy of Sciences*, vol. 103, no. 19, pp. 7228–7233, 2006.

[177] M. Nasir, D. R. Mott, M. J. Kennedy, J. P. Golden, and F. S. Ligler, "Parameters affecting the shape of a hydrodynamically focused stream," *Microfluidics and Nanofluidics*, vol. 11, no. 2, pp. 119–128, 2011.

[178] W. A. Braff, C. R. Buie, and M. Z. Bazant, "Boundary layer analysis of membraneless electrochemical cells," *Journal of The Electrochemical Society*, vol. 160, no. 11, pp. A2056–A2063, 2013.

[179] P. K. Kundu, I. M. Cohen, and D. R. Dowling, *Fluid mechanics*. Waltham, MA: Academic Press, 5th ed., 2012.

[180] P. N. Shankar, "On stokes flow in a semi-infinite wedge," *Journal of Fluid Mechanics*, vol. 422, pp. 69–90, 2000.

[181] E. Lauga, A. D. Stroock, and H. A. Stone, "Three-dimensional flows in slowly varying planar geometries," *Physics of Fluids*, vol. 16, no. 8, p. 3051, 2004.

[182] R. Rusconi, S. Lecuyer, L. Guglielmini, and H. A. Stone, "Laminar flow around corners triggers the formation of biofilm streamers," *Journal of The Royal Society Interface*, vol. 7, no. 50, pp. 1293–1299, 2010.

[183] J. Zhang, M. Li, W. H. Li, and G. Alici, "Inertial focusing in a straight channel with asymmetrical expansion–contraction cavity arrays using two secondary flows," *Journal of Micromechanics and Microengineering*, vol. 23, p. 085023, July 2013.

[184] T. F. Balsa, "Secondary flow in a Hele-Shaw cell," *Journal of Fluid Mechanics*, vol. 372, pp. 25–44, 1998.

[185] R. Sioshansi, "Increasing the Value of Wind with Energy Storage," *Energy Journal*, vol. 32, no. 2, pp. 1–29, 2011.

[186] US Department of Energy, "Report on the First Quadrennial Technology Review: Technology Assessments," pp. 1–292, 2012.

[187] M. Bolinger and R. Wiser, "Annual Report on U.S. Wind Power Installation, Cost, and Performance Trends: 2007," tech. rep., 2008.

[188] R. Sioshansi, "Emissions Impacts of Wind and Energy Storage in a Market Environment," *Environmental Science & Technology*, vol. 45, no. 24, pp. 10728–10735, 2011.

[189] E. S. Hrayshat, "Techno-economic Analysis of Electricity Generation by Means of a Proposed 50 MW Grid-connected Wind Power Plant for Jordan," *Energy Sources Part B-Economics Planning and Policy*, vol. 4, no. 3, pp. 247–260, 2009.

[190] J. Mason, V. Fthenakis, K. Zweibel, T. Hansen, and T. Nikolakakis, "Coupling PV and CAES power plants to transform intermittent PV electricity into a dispatchable electricity source," *Progress in Photovoltaics: Research and Applications*, vol. 16, no. 8, pp. 649–668, 2008.

[191] A. Oudalov, D. Chartouni, and C. Ohler, "Optimizing a battery energy storage system for primary frequency control," *IEEE Transactions on Power Systems*, vol. 22, no. 3, pp. 1259–1266, 2007.

[192] J. T. Alt, M. D. Anderson, and R. G. Jungst, "Assessment of utility side cost savings from battery energy storage," *IEEE Transactions on Power Systems*, vol. 12, no. 3, pp. 1112–1118, 1997.

[193] B. Sørenson, "Dependability of Wind Energy Generators with Short-Term Energy-Storage," *Science*, vol. 194, no. 4268, pp. 935–937, 1976.

[194] J. B. Greenblatt, S. Succar, D. C. Denkenberger, R. H. Williams, and R. H. Socolow, "Baseload wind energy: modeling the competition between gas turbines and compressed air energy storage for supplemental generation," *Energy Policy*, vol. 35, no. 3, pp. 1474–1492, 2007.

[195] L. Göransson and F. Johnsson, "Large scale integration of wind power: moderating thermal power plant cycling," *Wind Energy*, vol. 14, no. 1, pp. 91–105, 2011.

[196] O. A. Jaramillo, M. A. Borja, and J. M. Huacuz, "Using hydropower to complement wind energy: a hybrid system to provide firm power," *Renewable Energy*, vol. 29, no. 11, pp. 1887–1909, 2004.

[197] P. Denholm, G. L. Kulcinski, and T. Holloway, "Emissions and Energy Efficiency Assessment of Baseload Wind Energy Systems," *Environmental Science & Technology*, vol. 39, no. 6, pp. 1903–1911, 2005.

[198] P. Saran, J. Goentzel, and C. W. Siegert, "Economic analysis of wind plant and battery storage operation using supply chain management techniques," *Power and Energy Society General Meeting, 2010 IEEE*, pp. 1–8, 2010.

[199] E. D. Castronuovo and J. A. P. Lopes, "Optimal operation and hydro storage sizing of a wind–hydro power plant," *International Journal of Electrical Power & Energy Systems*, vol. 26, no. 10, pp. 771–778, 2004.

[200] R. Sioshansi, P. Denholm, T. Jenkin, and J. Weiss, "Estimating the value of electricity storage in PJM: Arbitrage and some welfare effects," *Energy Economics*, vol. 31, no. 2, pp. 269–277, 2009.

[201] R. Walawalkar and J. Apt, "Market Analysis of Emerging Electric Energy Storage Systems," Tech. Rep. DOE/NETL-2008/1330, Carnegie Mellon University, 2008.

[202] ISO New England Website, 2013.

[203] Energy Reliability Council of Texas Website, "http://www.ercot.com," 2013.

[204] California ISO Website, "http://www.caiso.com," 2013.

[205] National Solar Radiation Database, "http://rredc.nrel.gov/solar/old_data/nsrdb/1991-2010/," 2013.

[206] D. Ginley, M. A. Green, and R. Collins, "Solar energy conversion toward 1 terawatt," *MRS Bulletin*, vol. 33, pp. 355–364, Apr. 2013.

[207] F. Graves, T. Jenkin, and D. Murphy, "Opportunities for Electricity Storage in Deregulating Markets," *The Electricity Journal*, vol. 12, no. 8, pp. 46–56, 1999.

[208] R. Walawalkar, J. Apt, and R. Mancini, "Economics of electric energy storage for energy arbitrage and regulation in New York," *Energy Policy*, vol. 35, no. 4, pp. 2558–2568, 2007.

[209] F. Figueiredo, Flynn, P.C., and E. Cabral, "The economics of energy storage in 14 deregulated power markets," *Energy Studies Review*, vol. 14, no. 2, p. 2, 2006.

[210] EPRI, "EPRI-DOE Handbook of Energy Storage for Transmission and Distribution Applications," Tech. Rep. 1001834, Palo Alto, CA, 2003.

[211] J. Eyer and G. Corey, "Energy Storage for the Electricity Grid: Benefits and Market Potential Assessment Guide," *Sandia National Laboratories*, pp. 1–232, Feb. 2010.